

12

AFGL-TR-85-0321

Analysis of Near-field Seismic Waveforms From
Underground Nuclear Explosions

by Jeffrey S. Barker, L. J. Burdick and Terry C. Wallace

Woodward-Clyde Consultants
566 El Dorado St.
Pasadena, CA 91101

15 September 1985

Scientific Report No. 1

Approved for Public Release; Distribution Unlimited

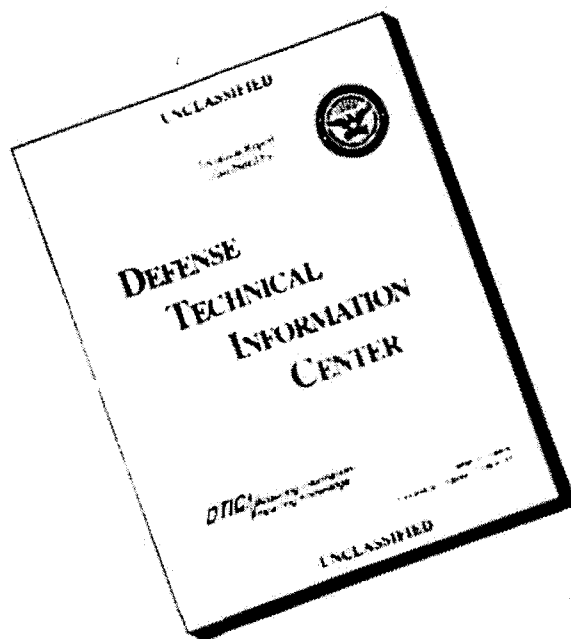
Air Force Geophysics Laboratory
Air Force Systems Command
United States Air Force
Hanscom Air Force Base, Massachusetts 01731

SECRET

AD-A165 227

NTIC FILE COPY

DISCLAIMER NOTICE




THIS REPORT IS INCOMPLETE BUT IS THE BEST AVAILABLE COPY FURNISHED TO THE CENTER. THERE ARE MULTIPLE MISSING PAGES. ALL ATTEMPTS TO DATE TO OBTAIN THE MISSING PAGES HAVE BEEN UNSUCCESSFUL.

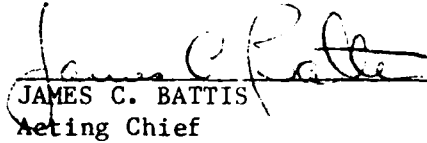
ARPA Order No. 5308
Contract No. F19628-85-C-0036
Effective Date of Contract: 5 March 1985
Contract Expiration Date: 4 March 1987
Amount of Contract: \$293,022
Contractor: Woodward-Clyde Consultants
566 El Dorado St, Suite 100
Pasadena, CA 91101

Principal Investigator & Phone No.
L. J. Burdick
Senior Project Seismologist
(818) 449-7650

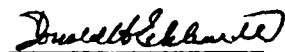
The views and conclusions contained in this document are those of the authors and should not be interpreted as representing the official policies, either expressed or implied, of the Defense Advanced Research Projects Agency or the U. S. Government.

This technical report has been reviewed and is approved for publication.


JAMES F. LEWKOWICZ
Contract Manager


JAMES C. BATTIS
Acting Chief
Solid Earth Geophysics Branch

FOR THE COMMANDER


DONALD H. ECKHARDT
Director
Earth Sciences Division

This report has been reviewed by the ESD Public Affairs Office (PA) and is releasable to the National Technical Information Service (NTIS).

Qualified requesters may obtain additional copies from the Defense Technical Information Center. All others should apply to the National Technical Information Service.

If your address has changed, or if you wish to be removed from the mailing list, or if the address is no longer employed by your organization, please notify AFGL/DAA, Hanscom AFB, MA 01731. This will assist us in maintaining a current mailing list.

Unclassified

SECURITY CLASSIFICATION OF THIS PAGE

REPORT DOCUMENTATION PAGE

1a. REPORT SECURITY CLASSIFICATION			1b. RESTRICTIVE MARKINGS none		
2a. SECURITY CLASSIFICATION AUTHORITY			3. DISTRIBUTION/AVAILABILITY OF REPORT Approved for public release; distribution unlimited.		
2b. DECLASSIFICATION/DOWNGRADING SCHEDULE					
4. PERFORMING ORGANIZATION REPORT NUMBER(S) WCCP-R-85-05			5. MONITORING ORGANIZATION REPORT NUMBER(S) AFGL-TR-85-0321		
6a. NAME OF PERFORMING ORGANIZATION Woodward-Clyde Consultants		6b. OFFICE SYMBOL (If applicable)		7a. NAME OF MONITORING ORGANIZATION Air Force Geophysics Laboratory	
6c. ADDRESS (City, State and ZIP Code) 566 El Dorado St., Suite 100 Pasadena, CA 91101			7b. ADDRESS (City, State and ZIP Code) Hanscom Air Force Base Massachusetts 01731-5000		
8a. NAME OF FUNDING/SPONSORING ORGANIZATION DARPA		8b. OFFICE SYMBOL (If applicable)		9. PROCUREMENT INSTRUMENT IDENTIFICATION NUMBER F19628-85-0036	
8c. ADDRESS (City, State and ZIP Code) 1400 Wilson Blvd. Arlington, VA 22209			10. SOURCE OF FUNDING NOS.		
11. TITLE (Include Security Classification) see block 16 - unclassified			PROGRAM ELEMENT NO. 62714E		TASK NO. DA
			PROJECT NO. 5A10		WORK UNIT NO. AV
12. PERSONAL AUTHOR(S) Jeffrey S. Barker, L. J. Burdick and Terry C. Wallace					
13a. TYPE OF REPORT Scientific Report #1		13b. TIME COVERED FROM 3/5/85 TO 9/5/85		14. DATE OF REPORT (Yr. Mo. Day) 15 September 1985	
15. PAGE COUNT 132					
16. SUPPLEMENTARY NOTATION Analysis of Near-field Seismic Waveforms from Underground Nuclear Explosions					
17. COSATI CODES			18. SUBJECT TERMS (Continue on reverse if necessary and identify by block number)		
FIELD	GROUP	SUB. GR.	Mueller-Murphy and Helmlberger-Hadley source functions, Near-field seismic observations, Nuclear explosions, Dry tuff, Alluvium, Seismic detection of Nuclear Explosions		
19. ABSTRACT (Continue on reverse if necessary and identify by block number) <p>This report consists of three parts. In the first, we compare the Mueller-Murphy and Helmlberger-Hadley source representations and investigate whether there are any features of the near-field observations which tend to favor one over the other. We found that the scaling relations in the two formalisms are such that the spectra are virtually indistinguishable between 2 and 5 Hz. Although the Mueller-Murphy source is too rich in high frequency energy, a moderately low Q value for the near-field crust can make it agree with the observations. There are significant differences in the spectra of the two source representations in the frequency band from 0.5 to 2 Hz, which controls the amplitude of the short-period, teleseismic P waves. If the Mueller-Murphy source is assumed, the global average t^* value for events at NTS is slightly larger than 1.0 sec. If the Helmlberger-Hadley source is used, it is about 0.7 sec. Further research on teleseismic and crustal attenuation will be needed before a firm conclusion that the Mueller-Murphy source is in significant error will be warranted.</p>					
20. DISTRIBUTION/AVAILABILITY OF ABSTRACT UNCLASSIFIED/UNLIMITED <input checked="" type="checkbox"/> SAME AS RPT <input type="checkbox"/> OTIC USERS <input type="checkbox"/>			21. ABSTRACT SECURITY CLASSIFICATION Unclassified		
22a. NAME OF RESPONSIBLE INDIVIDUAL James Lewkowicz			22b. TELEPHONE NUMBER (Include Area Code)		22c. OFFICE SYMBOL AFGL/IWH

In the third part, ~~we have~~ introduced a method for the simultaneous inversion of near-field waveforms for source and structure parameters. The source may be parameterized by any of several effective source functions. The structure model is parameterized as a layered stack in which the free parameters are the velocity at the top of the layer, the gradient within the layer, and the depth to the top of the layer. For each observation, the residuals consist of the normalized cross-correlation coefficient between the data and synthetics (a measure of waveform fit), the difference in the normalization factors (a measure of absolute amplitude), and the time lag to the peak of the cross-correlation function (a measure of absolute travel time). Numerical partial derivatives are computed using asymptotic generalized ray theory, and the problem is solved using an iterative generalized inverse. Test inversions have been performed for simple structure models, and yield valuable information on the weighting of parameters and residuals and the trade-offs between parameters.

Accession For

NTIS GRA&I	<input checked="" type="checkbox"/>
DTIC TAB	<input type="checkbox"/>
Unannounced	<input type="checkbox"/>
Justification	

Dist

A-1

TABLE OF CONTENTS

	<u>Page</u>
PREFACE	v
 <u>PART I - A COMPARISON OF THE MUELLER-MURPHY AND HELMBERGER-HADLEY SOURCE FUNCTIONS</u>	
INTRODUCTION	3
YIELD SCALING RELATIONSHIPS	5
COMPARISONS OF SPECTRA AND WAVEFORMS	10
ATTENUATION IN THE CRUST	26
DISCUSSION	33
REFERENCES	35
APPENDIX	37
 <u>PART II - MODELING NEAR-FIELD OBSERVATIONS FROM NUCLEAR EXPLOSIONS IN DRY TUFF AND ALLUVIUM</u>	
INTRODUCTION	63
NEAR-FIELD MODELING	65
THE DATA	73
DISCUS THROWER	73
MUDPACK	79
MERLIN	82
DISCUSSION	83
CONCLUSIONS	90
REFERENCES	93

TABLE OF CONTENTS (cont'd)

	<u>Page</u>
<u>PART III - SIMULTANEOUS INVERSION OF NEAR-FIELD DATA</u>	
<u>FOR SOURCE AND STRUCTURE PARAMETERS -</u>	
<u>A PRELIMINARY ASSESSMENT</u>	
INTRODUCTION	96
BACKGROUND	97
INVERSION METHOD	101
PRELIMINARY ASSESSMENT	108
CONCLUSIONS	121
REFERENCES	125

PREFACE

This mid-term report includes a discussion of a timely and controversial issue, a continuation of a fruitful line of research, and an introduction of a new direction of research, all oriented toward the modeling of near-field records from underground nuclear explosions. In the first part, we compare the Mueller-Murphy and Helmberger-Hadley effective source functions, and discuss their applicability to near-field waveform modeling. Our goal is to attempt to identify and reconcile the resolvable differences between these source representations so that consistent yield scaling relations may be obtained. The second part of this report includes a waveform modeling study aimed at determining yield scaling relations for nuclear explosions in dry tuff and alluvium at Yucca Flats. This is a continuation of the approach we have used for modeling near-field data from the Amchitka and Pahute Mesa test sites. An additional point of interest, however, is the apparent identification of the elastic radius. Beyond a scaled slant range of about 130 m, elastic waveform modeling predicts observed peak velocities quite well, but inside that range, the observations are overpredicted. In the final part of this report, we introduce a method for the simultaneous inversion of near-field data for source and structure parameters. This is desirable in order to obtain quantitative information on the trade-offs between parameters and also to enable the modeling of near-field data from sites for which no structure model previously exists. Preliminary tests are presented for the structure inversion portion of the method by inverting synthetic data sets from simple models.

PART I

A COMPARISON OF THE MUELLER-MURPHY
AND HELMBERGER-HADLEY SOURCE FUNCTIONS

by

L. J. Burdick and J. S. Barker

INTRODUCTION

One of the most important goals in the field of nuclear seismology is the development of an accurately scaled representation of the reduced displacement potential. An early attempt at accomplishing this was made by Haskell (1967). The most widely accepted and acknowledged representation was later presented by Mueller and Murphy (1971). (An equivalent though mathematically simpler version of this representation was developed by von Seggern and Blandford (1972).) Haskell (1967) chose the algebraic form for his RDP representation so that it was simple and so that it did not predict discontinuities in displacement, velocity or acceleration. Mueller and Murphy (1971) derived their representation by assuming a form for the pressure time history on the walls of a spherical cavity. The function they adopted for the pressure history is discontinuous, and it predicts velocity pulses that are discontinuous and acceleration pulses that are singular. von Seggern and Blandford (1972) noted that observed near-field pulses often have rise times so short that they can be closely approximated by a discontinuous pulse. In a more recent modeling study of near-field velocity records, Helmberger and Hadley (1981) found that the velocity records they were studying did have a resolvable rise time. To model this information, they introduced an RDP representation which allows velocity pulses to have finite rise times. Their formalism was later utilized by Burdick, et al. (1984) and Hartzell, et al. (1983) in similar modeling studies for the same reasons. It is unfortunate that more than one formalism for representing the RDP is in current use since comparison of the results of different studies is made difficult. The purpose of this investigation is to find whether there actually are any features of

the near-field observations which might tend to favor either of the two alternate RDP representations over the other. A slightly modified mathematical representation in which the Mueller and Murphy (1971) source might be used in modeling studies is explored such that the rise time of the velocity pulse is resolvably greater than zero.

The key results of the investigation can be previewed as follows. It is widely believed that the most significant difference between the two alternate RDP representations is that Mueller and Murphy's (1971) has a high frequency falloff rate of f^{-2} and Helmberger and Hadley's (1981) has a rate of f^{-3} . We found that the scaling relations in the two formalisms are such that the spectra are virtually indistinguishable for frequencies from 2 and 5 Hz. Between 5 and 10 Hz, they diverge only by about a factor of two. It has been found that the Mueller-Murphy spectra are definitely too rich in high frequency energy in this band to satisfy the near-field observations. However, if a moderately low Q value is postulated for the near-field crust, the Mueller-Murphy source can be made to agree with the observations. In other words, though the Mueller-Murphy velocity pulse is discontinuous, which disagrees with the data, the attenuation corrected pulse is not. The corrected Mueller-Murphy spectra can be made to agree with the data about as well as the Helmberger-Hadley spectra from 2 to 10 Hz. There are significant differences in the spectra of the two source representations in the frequency band from 0.5 to 2.0 Hz. This is the band which controls the amplitude of the short period teleseismic P waves. If the Mueller-Murphy source is assumed, the global average t^* value for events at NTS comes out to be slightly larger than 1.0 sec. If the Helmberger-Hadley source is used it comes out to be about 0.7 sec. Other lines of evidence as to what this value should be might

be used in the future to differentiate between the two source representations in the 0.5 to 2.0 sec band.

YIELD SCALING RELATIONSHIPS

The algebraic representations for the RDPs contain various free parameters dependent on yield and depth. Actually, the functional forms are similar enough so that plots of the RDPs versus time will not appear to be significantly different for comparable values of the free parameters. von Seggern and Blandford (1972) discuss how to relate the Mueller-Murphy free parameters to those in other RDP formalisms. The algebraic expression for the Mueller-Murphy RDP is given by the convolution integral

$$\Psi(t) = \frac{r_{el} v_p^2}{4\mu} P(t) * F(t)$$

$$P(t) = ((P_{0s} - P_{0c}) \exp(-\alpha t) + P_{0c}) H(t)$$

$$F(t) = \sin(bt) \exp(at) / 8b$$

For a tuff-rhyolite emplacement medium,

$$r_{el} = 1490 Y^{0.33} / h^{0.42}$$

$$r_c = 31.4 Y^{0.29} / h^{0.11}$$

$$P_{0c} = 0.8 \mu (r_c / r_{el})^3$$

$$P_{0s} = 1.5 \rho g h$$

$$\alpha = 1.5 \omega_0 = 1.5 V_p / r_{el}$$

$$\beta = (\lambda + 2\mu) / 4\mu$$

$$a = -\omega_0 / 2\beta$$

$$b = \omega_0 (\beta - 0.25)^{0.5} / \beta$$

Y is yield in kt, h is source depth in m, ρ is the density in g/cm³, V_p is the compressional velocity at the source in km/s, and λ and μ are Lamé's constants. The expression for the Helmberger-Hadley RDP is

$$\Psi(t) = \Psi_\infty (1 - \exp(-kt) P(t))$$

$$P(t) = 1 + kt + \frac{1}{2}(kt)^2 - B(kt)^3$$

The Helmberger-Hadley scaling relationships for the same media (events at Pahute Mesa below the water table) are (Hartzell, et al., 1983)

$$\Psi_\infty = 6.72 \times 10^8 Y / h^{0.27}$$

$$k = 4.04 h^{0.42} / Y^{0.33}$$

$$B = 1$$

As discussed in detail by Lay, et al. (1984), the choice of $B = 1$ at all yields was made arbitrarily since it is very difficult to resolve its actual value from body wave data of any kind. For events at the Amchitka test site, the scaling relations become (Burdick, et al., 1984)

$$\Psi_{\infty} = 9.5 \times 10^8 Y/h^{0.27}$$

$$k = 4.7 h^{0.42}/Y^{0.33}$$

$$B = 1$$

The most meaningful way to compare the source representations is to compare the spectra they predict in the 0.5 to 10 Hz band. Graphs for yields of 1000 and 100 kt are shown in Figures 1 and 2, respectively. The most striking feature that emerges from this comparison is the strong agreement between the Pahute Mesa spectra between 2 and 10 Hz. The two different sets of scaling laws were based on comparable data, but the data were analyzed in very different ways. The agreement might thus be interpreted to mean that the source spectrum is well resolved in this band. Note that particularly at a yield of 1000 kt, the fact that the Mueller-Murphy source is decaying as f^{-2} and the Helmberger-Hadley as f^{-3} is not significant. The differences in the scaling of the corner frequency compensate for the differences in the high frequency slope. The agreement in the 2 to 10 Hz band is not quite as close at 100 kt as 1000 kt, but the Hartzell, et al. (1983) data set contained no records from events this small. Most of the records analyzed were from events larger than 500 kt. In any event, the strongest differences between the predicted Pahute Mesa source spectra at either yield are in the location of the corner frequency and the level of the spectral peak. The Amchitka spectra

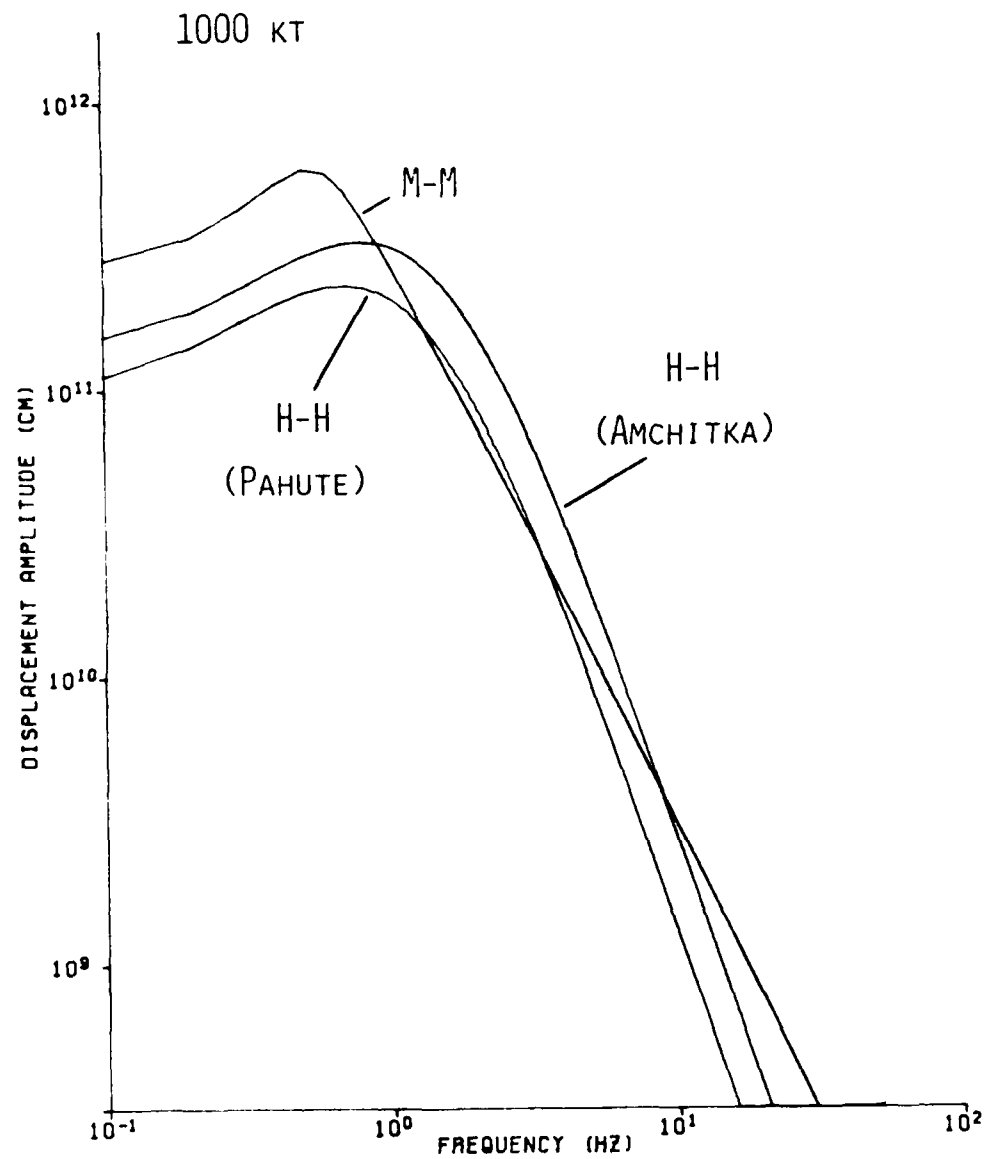


Figure 1. A comparison of the Mueller-Murphy and Helmberger-Hadley yield scaled RDP spectra. This particular case is for 1000 kt. Helmberger-Hadley spectra are shown for both Pahute Mesa and Amchitka.

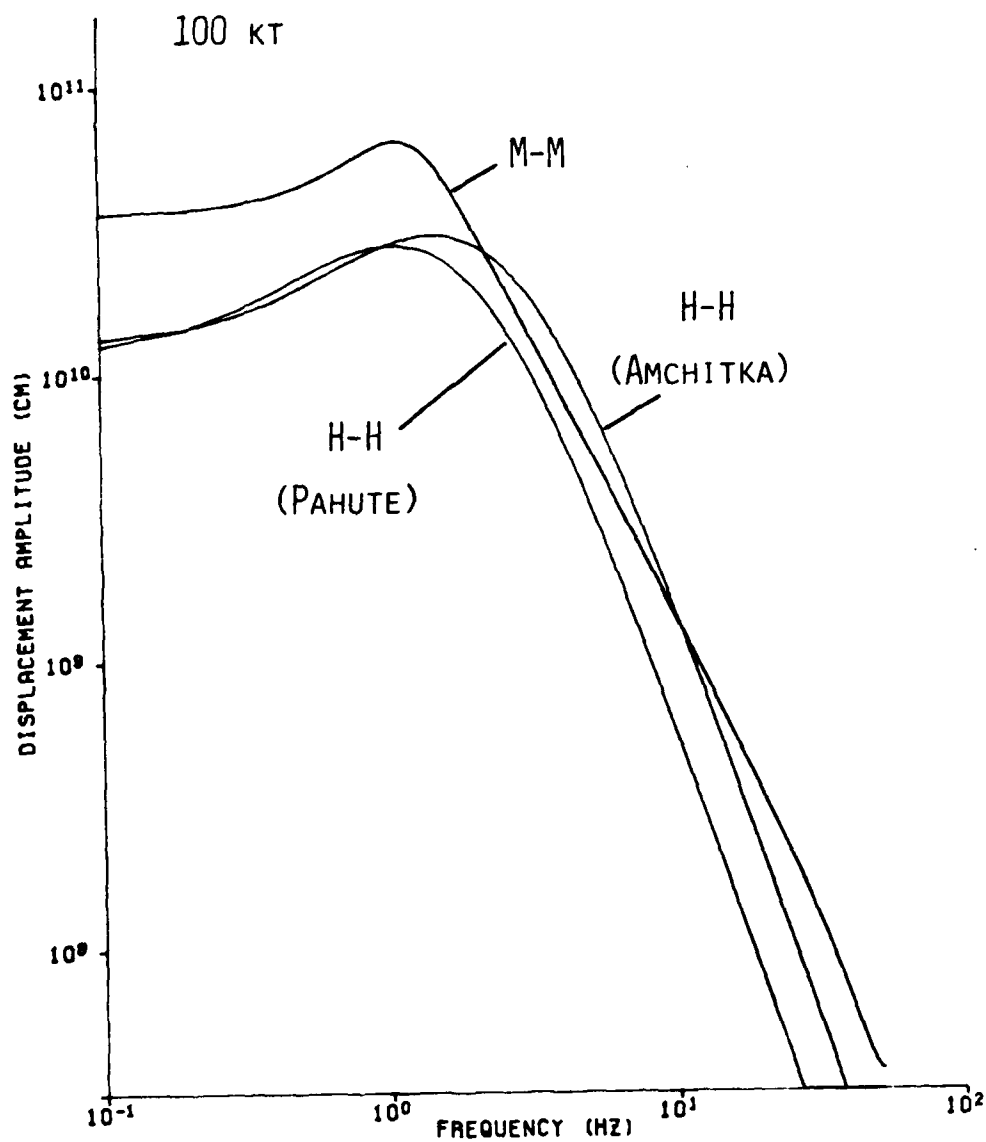


Figure 2. A comparison of the Mueller-Murphy and Helmlberger-Hadley yield scaled RDP spectra. This particular case is for 100 kt. Helmlberger-Hadley spectra are shown for both Pahute Mesa and Amchitka.

are shown in Figures 1 and 2 to illustrate the point that the Helmberger-Hadley source was observed to scale differently at the two different test sites. An important point of controversy is whether the characteristics of source spectra of well coupled events below the water table vary significantly from site to site. The results of the Hartzell, et al. (1983) and the Burdick, et al. (1984) study seem to indicate that they do. This is not predicted by the Mueller and Murphy (1971) correction factors for varying emplacement media. No additional light has been shed on this question in this study, but it is important to point out this significant difference between the Mueller-Murphy and Helmberger-Hadley scaling laws.

COMPARISONS OF SPECTRA AND WAVEFORMS

In this section, we will compare the predictions of the Mueller-Murphy and Helmberger-Hadley sources to observed near-field spectra and waveforms from well-coupled Pahute Mesa events. We find that the Helmberger-Hadley representation fits better, but this is not surprising since we are considering the data originally used to constrain the source model. On the other hand, the Mueller-Murphy model was based on similar data from some of the same events.

The types of comparisons to be considered in this section are between completely synthetic spectra and waveforms and their corresponding observations. Computation of the synthetics requires a correction for the effects of wave propagation through the crust. To calculate these corrections, we will use the crustal model for Pahute Mesa developed by

Hartzell, et al. (1983) and a generalized ray computer algorithm. The model of Hartzell, et al. (1983) is compared to other crust models for Pahute in Figure 3. The model has no unusual properties and is very comparable to those found by Hamilton and Healy (1969) and Carroll (1966). The most important point for this discussion is that to P waves in the frequency band of interest, the crust appears to have a smooth positive gradient. This means that for the direct P, geometric ray theory is relatively accurate. The beginning of the Green's function of the crust is a delta function arriving at the retarded time, and if the source pulse initially contains a discontinuity then the arriving pulse will as well. It is assumed in the calculations shown in this section that the Q in the crust is high enough so that anelastic effects are not significant. In the following section, the implications of this assumption will be considered in detail.

It is generally useful to consider time domain information before proceeding with a spectral analysis in order to illuminate exactly what the spectra represent. Also, many significant spectral characteristics can be observed in and understood from the time domain pulses. Figures 4 and 5 show samples of near-field P waves from Pahute Mesa. Figure 4 shows a record from SCOTCH (155 kt announced) and BOXCAR (1300 kt announced). Synthetics predicted by the Helmberger-Hadley source are shown in dashed line and those by Mueller-Murphy in dotted line. The time window shown covers about 1.5 seconds after the direct arrival, which is comparable to the window used in the spectral analysis. An examination of the generalized ray synthetics shows that the dominant energy in this window consists of direct P and turning rays of the downgoing P type and the pP type. The direct upgoing ray is about equal in amplitude to the turning ray. Near-field converted PS and the

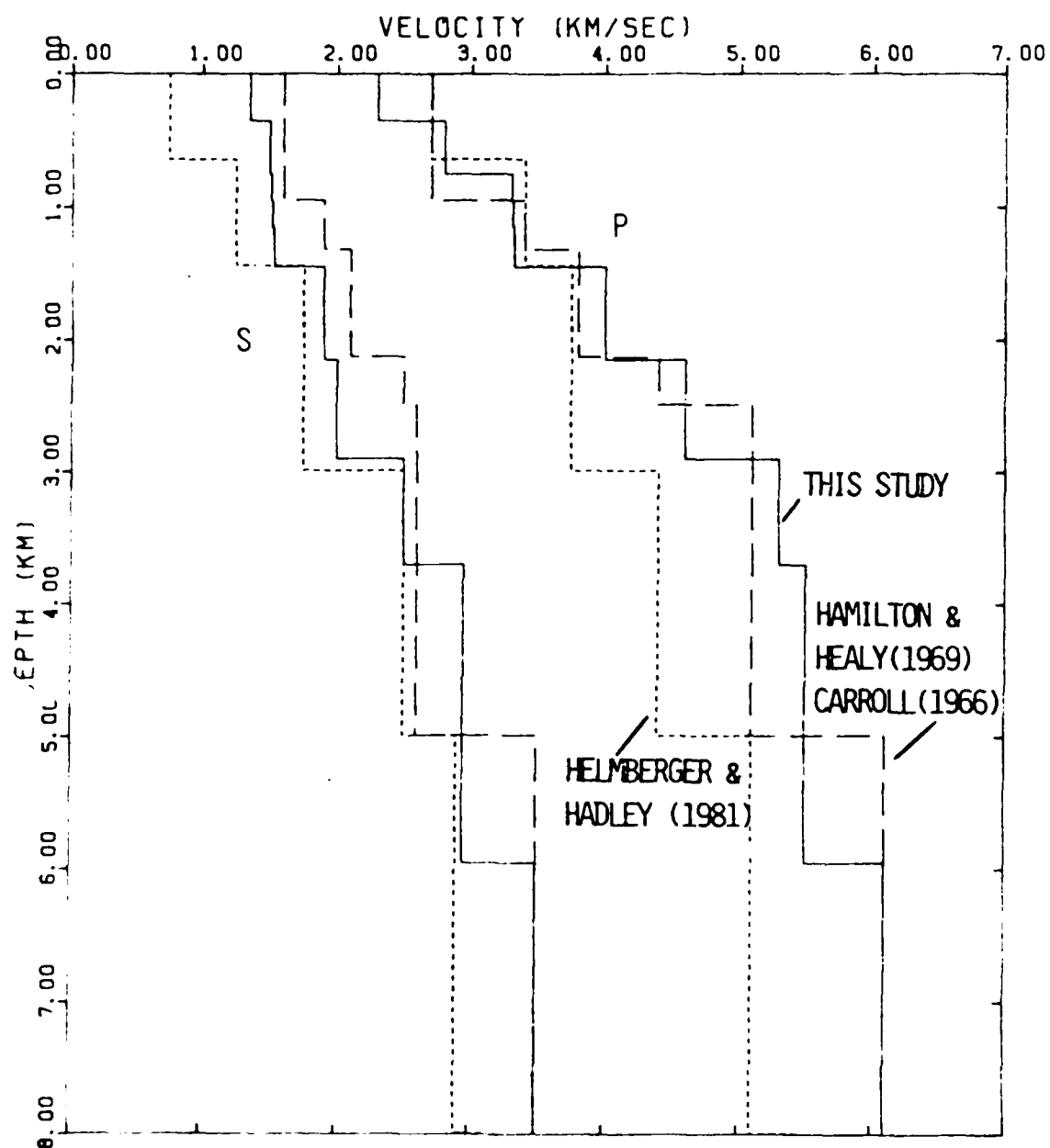


Figure 3. P and S wave velocity structures for Pahute Mesa (from Hartzell, et al., 1983).

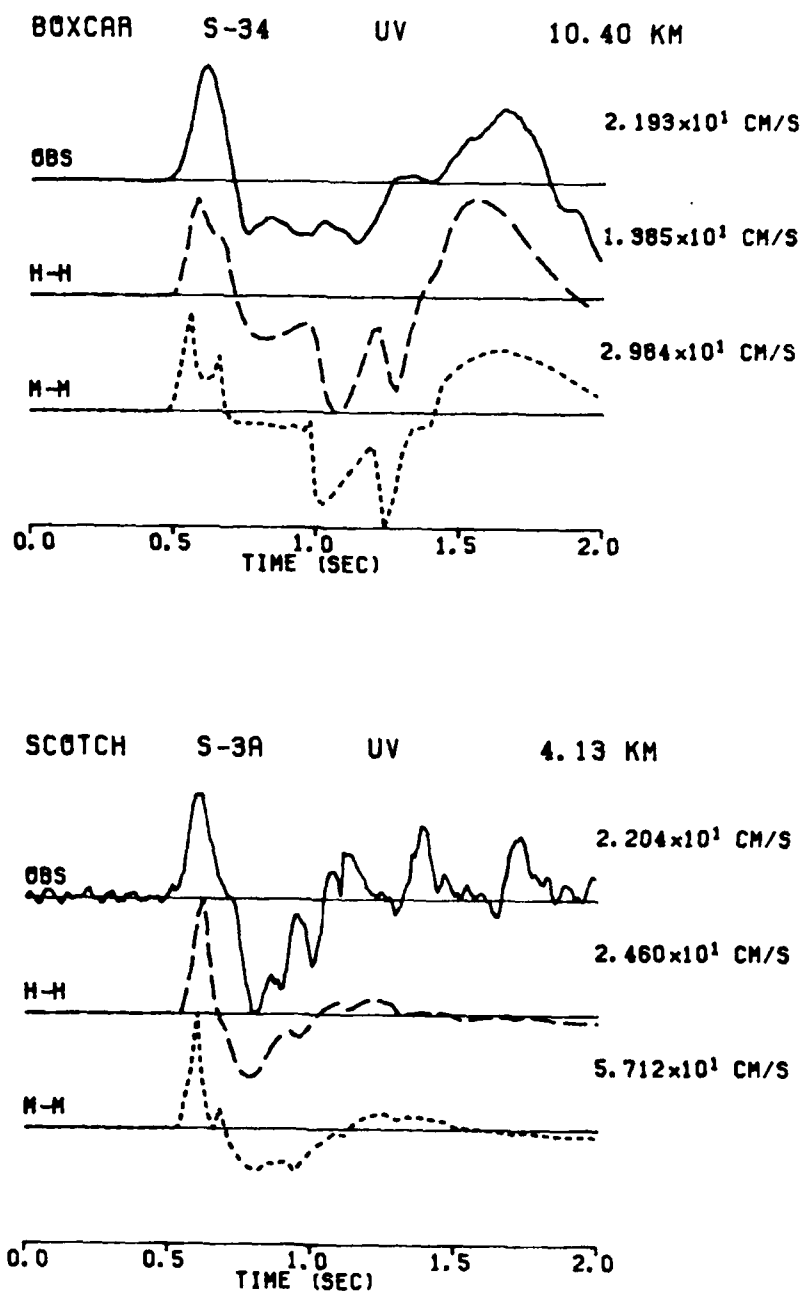
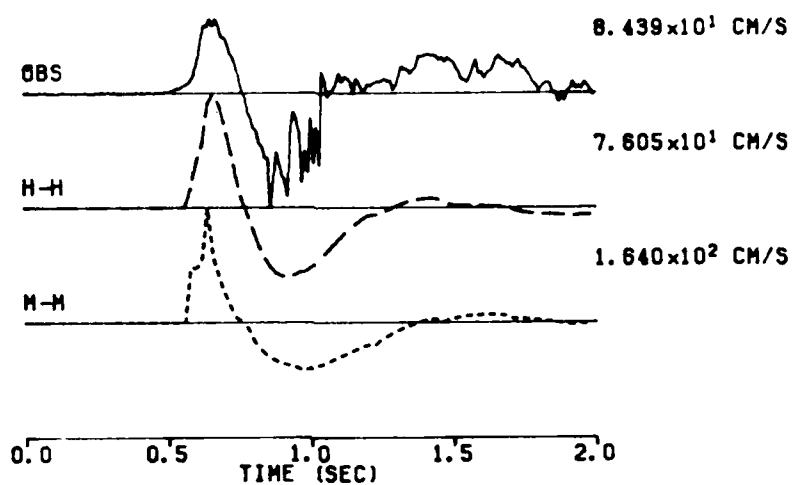


Figure 4. A comparison of observed (solid line) and synthetic (dashed Helmberger-Hadley or dotted Mueller-Murphy) near-field P waves for BOXCAR (above) and SCOTCH (below). The Mueller-Murphy source is clearly too high in frequency content. The trace amplitude is indicated on the right.

ALMENDRO L-03

UVH 3.20 KM



ALMENDRO L-06

UVH 10.00 KM

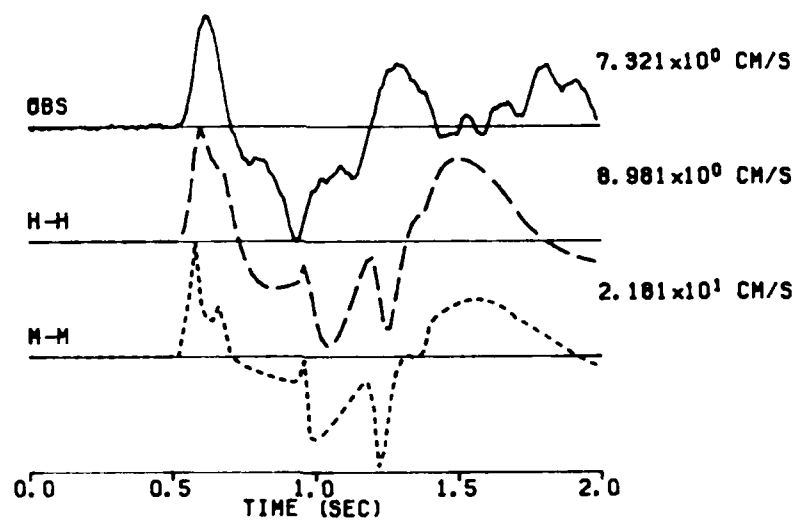


Figure 5. A comparison of observed (solid line) and synthetic (dashed Helmberger-Hadley or dotted Mueller-Murphy) near-field P waves for ALMENDRO at ranges of 3.2 (above) and 10 km (below). The Mueller-Murphy source is clearly too high in frequency content. The trace amplitude is indicated on the right.

Rayleigh wave arrive later. The most obvious difference in the Mueller-Murphy and Helmlinger-Hadley synthetics is that the former predicts a much shorter duration first arrival. It is much too high in frequency to match the observations. Figure 5 shows a comparison of data and synthetics for ALMENDRO (566 kt estimated) at two different ranges. The fact that the Mueller-Murphy synthetics are too high in frequency does not appear to depend on the range. At the ranges less than 5 km, the pulses are relatively simple and propagation effects are easily modeled, so spectral comparisons of data and synthetics should yield meaningful results. At the larger ranges in Figures 4 and 5, multiple reverberations become more important. They are more unstable and difficult to model so the match between data and synthetics is poorer.

Since the first positive peak is always clear in the data and can unambiguously be associated with the direct P arrival, it is instructive to consider its absolute amplitude in the time domain. An inspection of the trace amplitudes in Figures 4 and 5 indicates that the predicted values for the Mueller-Murphy source are generally 50 to 100% higher than the observed values, as should be expected if it is too enriched in high frequency energy. The complete set of predicted versus observed first peak amplitudes as well as the relative percent error for both sources are given in Table 1. We define the relative percent error as

$$\text{Error} = 200 (\text{synthetic-observed})/(\text{synthetic+observed}).$$

As illustrated in Figure 6, the Mueller-Murphy amplitudes are too high for all events considered. The event average of the relative percent errors of the Mueller-Murphy amplitudes are indicated by squares while those of the

Table 1 - Predicted and Observed Peak Amplitudes

		Observed	Helmberger-Hadley		Mueller-Murphy	
	Range (km)	Amplitude (cm/s)	Amplitude (cm/s)	Error (%)	Amplitude (cm/s)	Error (%)
<u>BOXCAR</u>						
S-12*	3.8	82.11	89.79	8.9	190.1	79.3
S-16*	4.9	60.90	65.10	6.7	149.3	84.1
S-24	7.3	30.91	29.24	-5.5	59.66	63.5
S-34	10.4	21.93	11.95	-58.9	26.38	18.4
S-74	22.5	2.01	3.81	61.8	8.69	124.8
<u>ALMENDRO</u>						
L-03	3.2	67.98	76.05	11.2	164.0	82.8
L-04	3.2	67.03	76.05	12.6	164.0	83.9
ECHO	3.4	58.25	59.30	1.8	114.8	65.4
L-05	5.1	34.00	47.85	33.8	112.2	107.0
L-02	6.1	29.19	28.78	-1.4	53.53	58.8
L-06	10.0	7.41	8.70	16.0	21.81	98.6
L-01	12.6	16.78	5.65	-99.2	9.67	-53.8
<u>MAST</u>						
S-5	3.65	43.51	45.37	4.2	112.0	88.1
S-6	5.47	13.94	33.24	81.8	77.01	138.7
S-7	7.30	8.18	17.72	73.7	36.04	126.0
<u>SCOTCH</u>						
S-3A	4.13	20.05	24.60	20.4	57.12	96.1
S-4	6.06	17.28	17.32	0.2	35.13	68.1
<u>INLET</u>						
S-5	1.63	74.29	78.38	5.4	167.5	77.1
S-6	3.27	28.17	39.29	33.0	80.09	95.9
S-7	6.53	22.07	19.90	-10.3	38.65	54.6
<u>HALFBEAK</u>						
S-5	2.13	91.43	78.93	-7.3	123.8	30.1
S-7	2.13	74.15	78.93	6.2	123.8	50.2
S-8	2.28	51.62	81.51	44.9	116.6	77.2
S-6	3.05	58.80	52.04	-12.2	91.62	43.6

* only marginally outside spill zone.

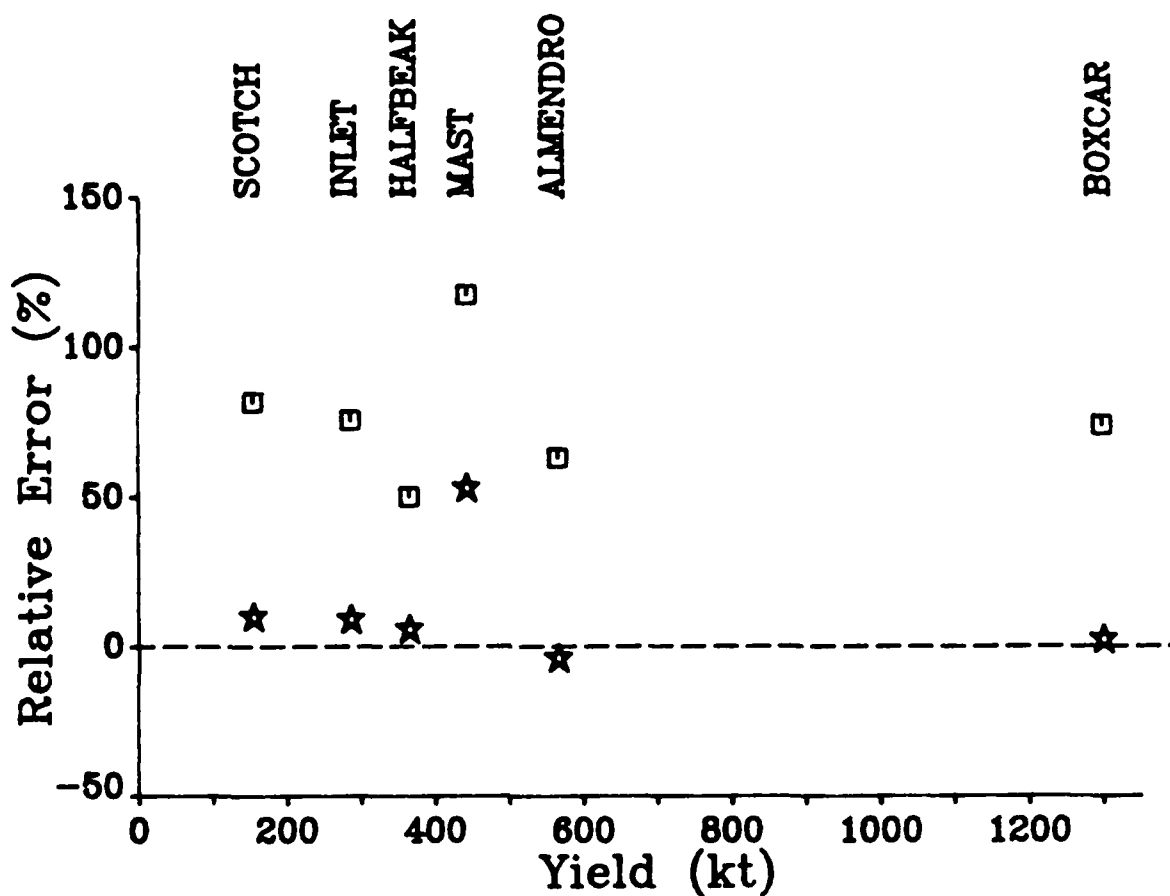


Figure 6. Average relative error of the predicted near-field amplitude of the Mueller-Murphy source (squares) and the Helmberger-Hadley source (stars) as a function of yield. The Mueller-Murphy source typically predicts P-wave amplitudes which are 50 to 100% too large while the Helmberger-Hadley source is generally accurate.

Helmberger-Hadley source are shown as stars. The only significant mismatch of the latter source is for MAST. Hartzell, et al. (1983) suggest that this mismatch is due to the fact that several of the MAST recordings were very noisy. The key point of this brief time domain analysis is that it is clear from this comparison that the Mueller-Murphy source is too rich in high frequencies to satisfy the data.

The data set used in the spectral analysis contained 24 records from 6 well-coupled events at Pahute Mesa. The data were originally recorded on magnetic tape by Sandia and subsequently machine digitized to high accuracy at a rate of 1000 samples per second. Thus, there is little question as to the accuracy of the spectra. The major problem in the analysis is in choosing a suitable time window. We have selected a cosine taper window of 2 seconds total duration with a 0.25 second taper at each end. There are 1.5 seconds of unaltered signal. In each example to be shown, an extended record section with the window placement indicated will be displayed along with the spectra so the reader can judge how appropriate the selection of the positioning of the window is.

The observed and synthetic spectra for the four signals shown in Figures 4 and 5 are shown in Figures 7 through 10. The BOXCAR spectra in Figure 7 illustrate most clearly the key results of the analysis. At frequencies between 1 and 5 Hz, the Mueller-Murphy and Helmberger-Hadley spectra agree with each other, and it is difficult to say which agrees with the observed spectra more closely. Between 5 and 10 Hz, the dotted Mueller-Murphy spectrum clearly drifts well above the observed while the Helmberger-Hadley continues to track it. Figure 8 compares the spectra from the SCOTCH record. The same general points are true though perhaps not as clearly. This example was

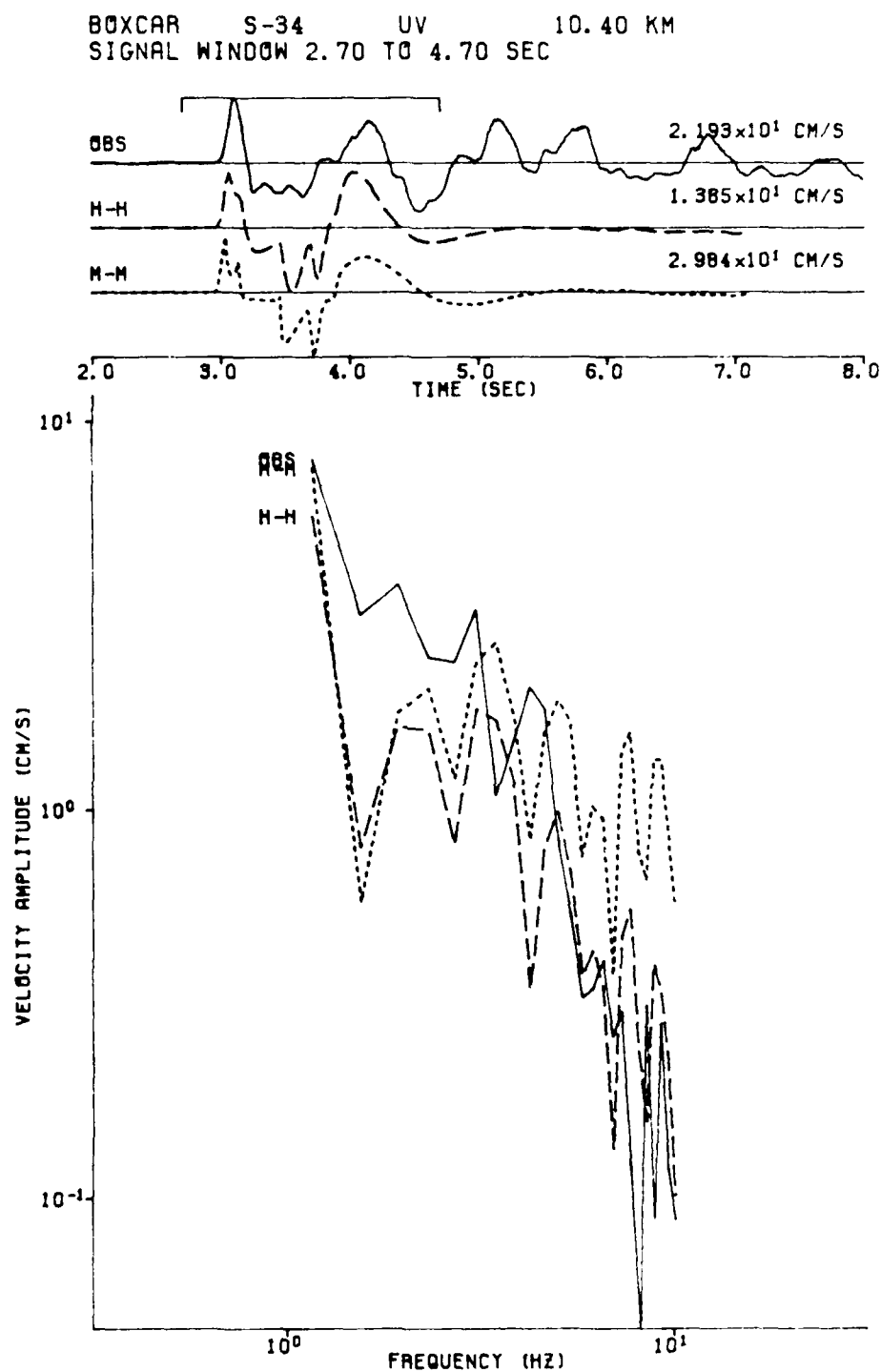


Figure 7. A comparison of the observed (solid line) versus predicted (Mueller-Murphy dotted line or Helmburger-Hadley dashed line) near-field P-wave velocity spectra for BOXCAR. The original observed and synthetic time series are shown at the top with the trace amplitudes indicated. The positioning and length of the signal window is indicated at the very top.

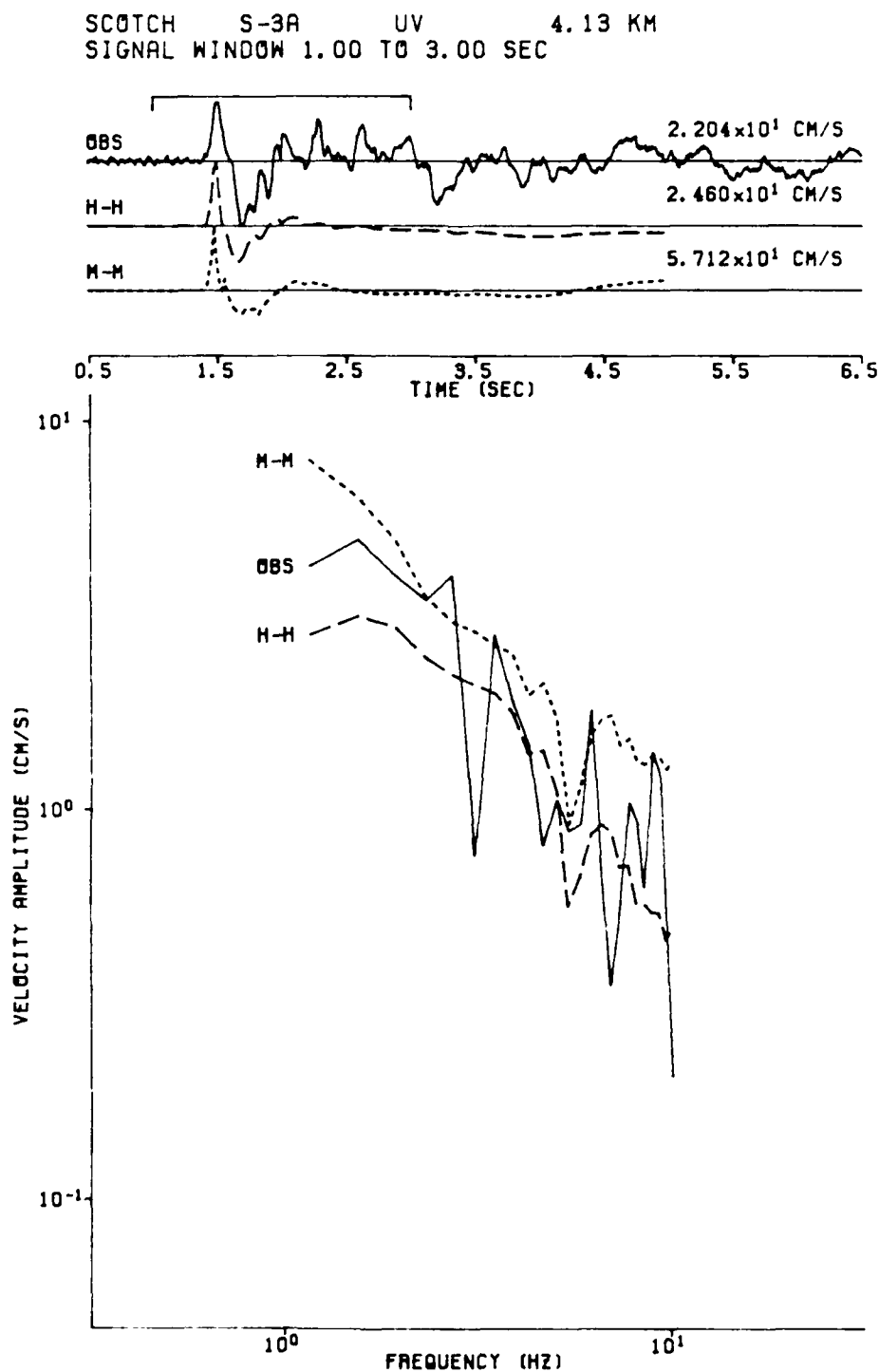


Figure 8. A comparison of the observed (solid line) versus predicted (Mueller-Murphy dotted line or Helmburger-Hadley dashed line) near-field P-wave velocity spectra for SCOTCH. The original observed and synthetic time series are shown at the top with the TRACE amplitudes indicated. The positioning and length of the signal window is indicated at the very top.

ALMENDRO L-03 UVH 3.20 KM
SIGNAL WINDOW 0.80 TO 2.80 SEC

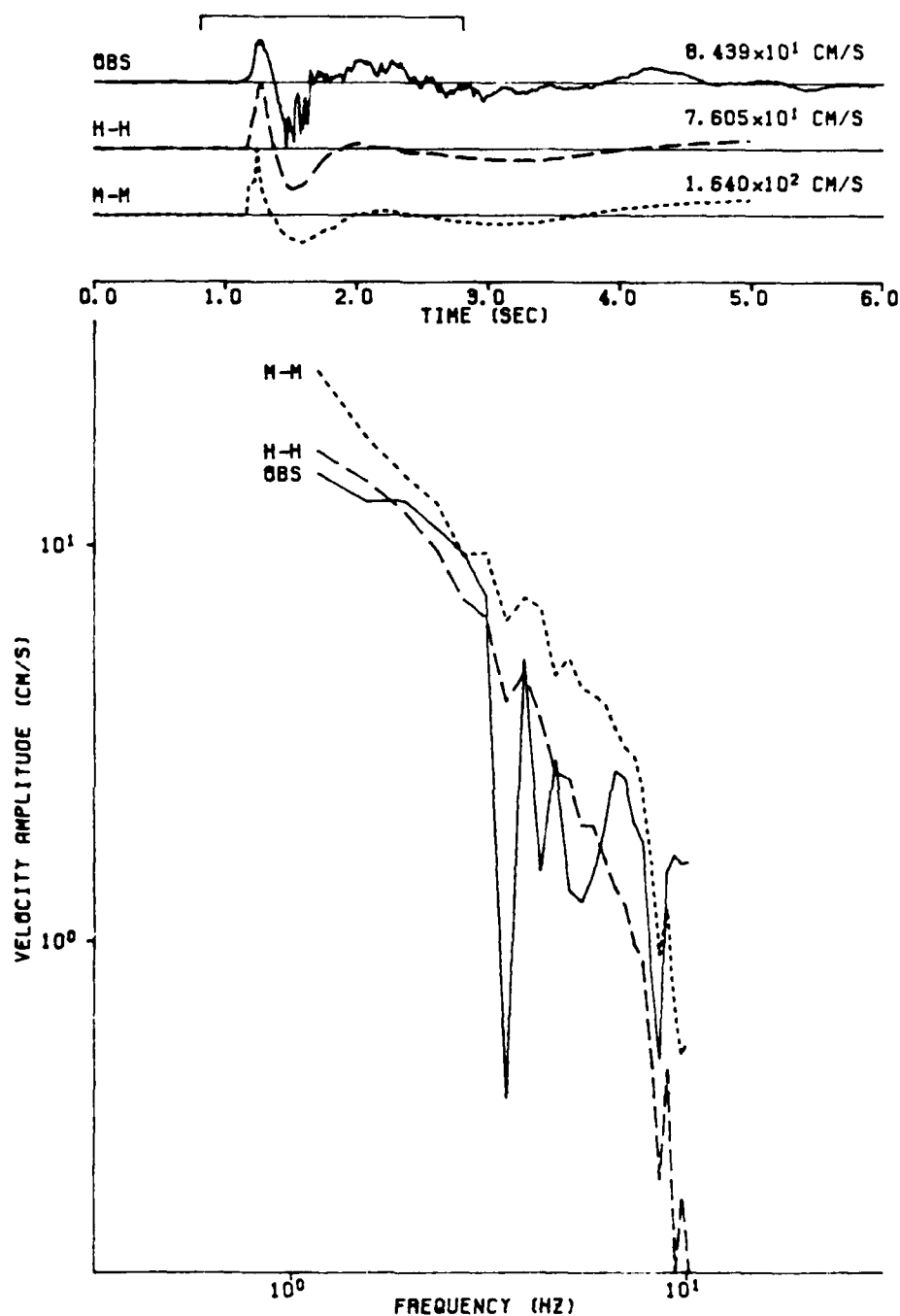


Figure 9. A comparison of the observed (solid line) versus predicted (Mueller-Murphy dotted line or Helmburger-Hadley dashed line) near-field P-wave velocity spectra for ALMENDRO at 3.2 km. The original observed and synthetic time series are shown at the top with the trace amplitudes indicated. The positioning and length of the signal window is indicated at the very top.

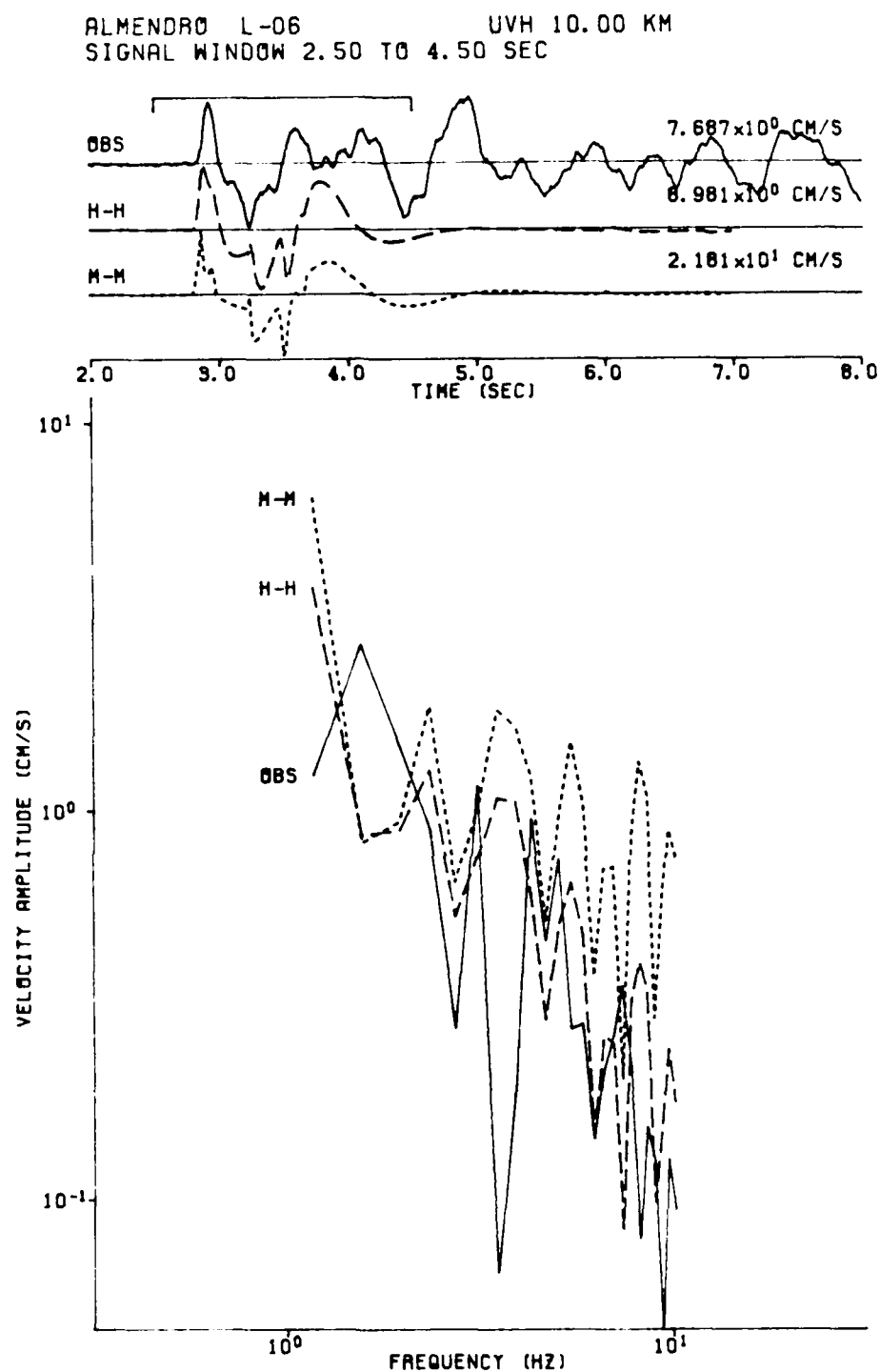


Figure 10. A comparison of the observed (solid line) versus predicted (Mueller-Murphy dotted line or Helmburger-Hadley dashed line) near-field P-wave velocity spectra for ALMENDRO at 10 km. The original observed and synthetic time series are shown at the top with the trace amplitudes indicated. The positioning and length of the signal window is indicated at the very top.

chosen to illustrate that the spectral values out to at least 2 Hz are still fairly sensitive to the characteristics of the window. The two examples from ALMENDRO in Figures 9 and 10 continue to show that the Mueller-Murphy spectra are too high in amplitude at high frequency, and furthermore that the mismatch does not appear to depend on range. The spectra at the more distant stations exhibit more complexity and the choice of window is much more problematical.

All 24 of the near-field P-wave spectra are shown in the Appendix. It is not fruitful to consider them on a case by case basis since their exact form is fairly unstable. It is necessary to find some objective way of averaging the results to isolate the stable characteristics. We elected to average the ratios of the predicted/observed spectra. This ratio would be unity at all frequencies if the synthetics fit the observations exactly. The results of the averaging of the 24 sets of spectra are shown in Figure 11. The HelMBERGER-HADLEY source fits better than the Mueller-Murphy at all frequencies greater than 5 Hz. The error in the Mueller-Murphy source increases steadily with frequency. In the 1 to 5 Hz band, the two models fit equally well but again the details of the spectral ratio in this range are highly dependent on the choice of window. In Figure 12, we show a similar spectral stack but in this instance we have increased the window length from 2 to 3 seconds. The instability of the low-frequency results is clear. There is some change in the high-frequency results as well, but it is not significant. The Mueller-Murphy spectral stack does not drift upward as strongly and the HelMBERGER-HADLEY stack drifts slightly downward. The reason for this is that the window has been extended beyond the range where the synthetics are accurate at high frequency. The ray sum has been truncated so the synthetic has no high frequency energy in the extended window while the

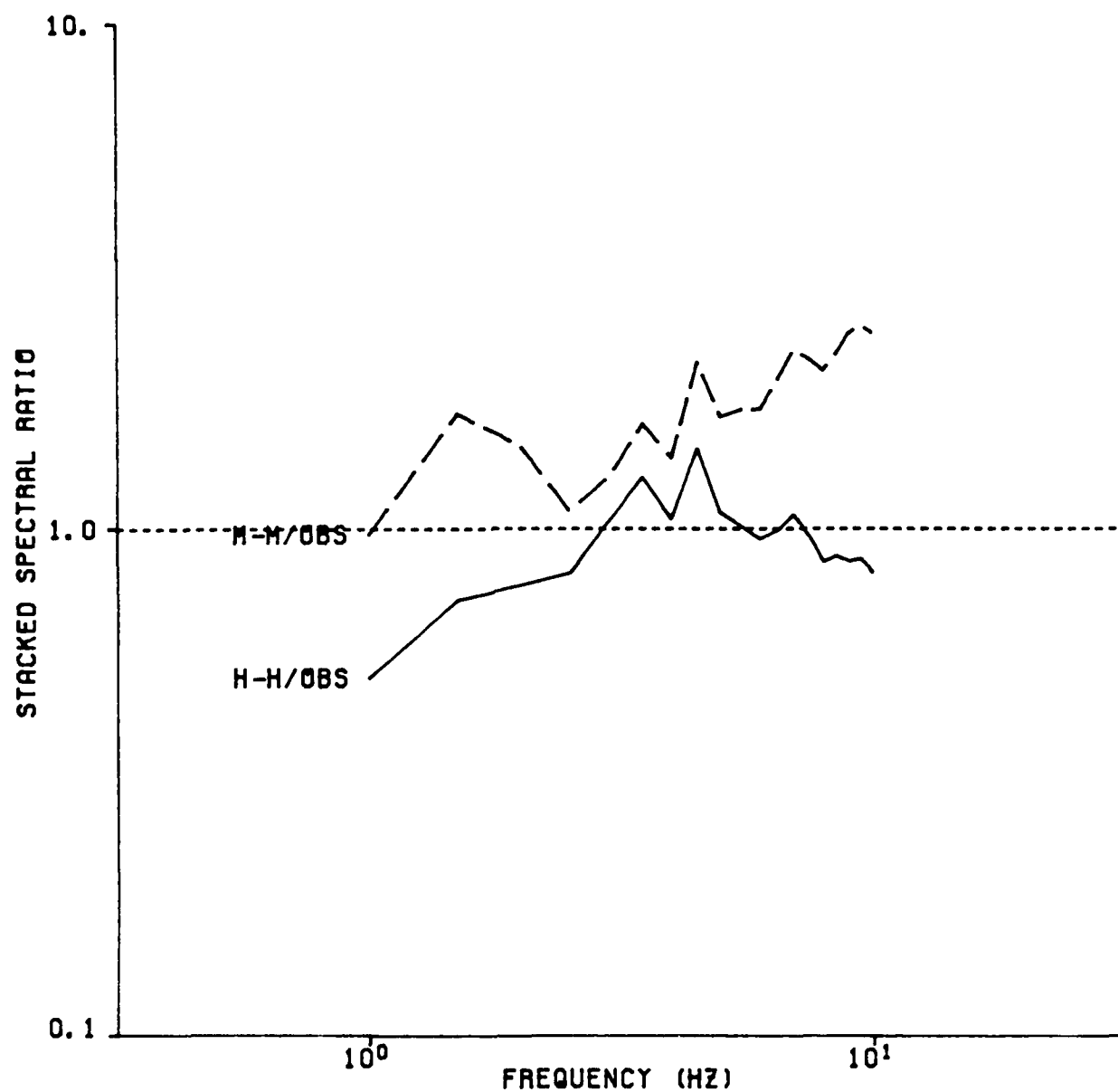


Figure 11. The average error in predicted/observed spectra. The observed and synthetic near-field P waves shown in the appendix were windowed and Fourier transformed. In each case, the ratio of predicted/observed spectra was formed and the average taken. The Mueller-Murphy ratios show a significant upward drift between 5 and 10 Hz.

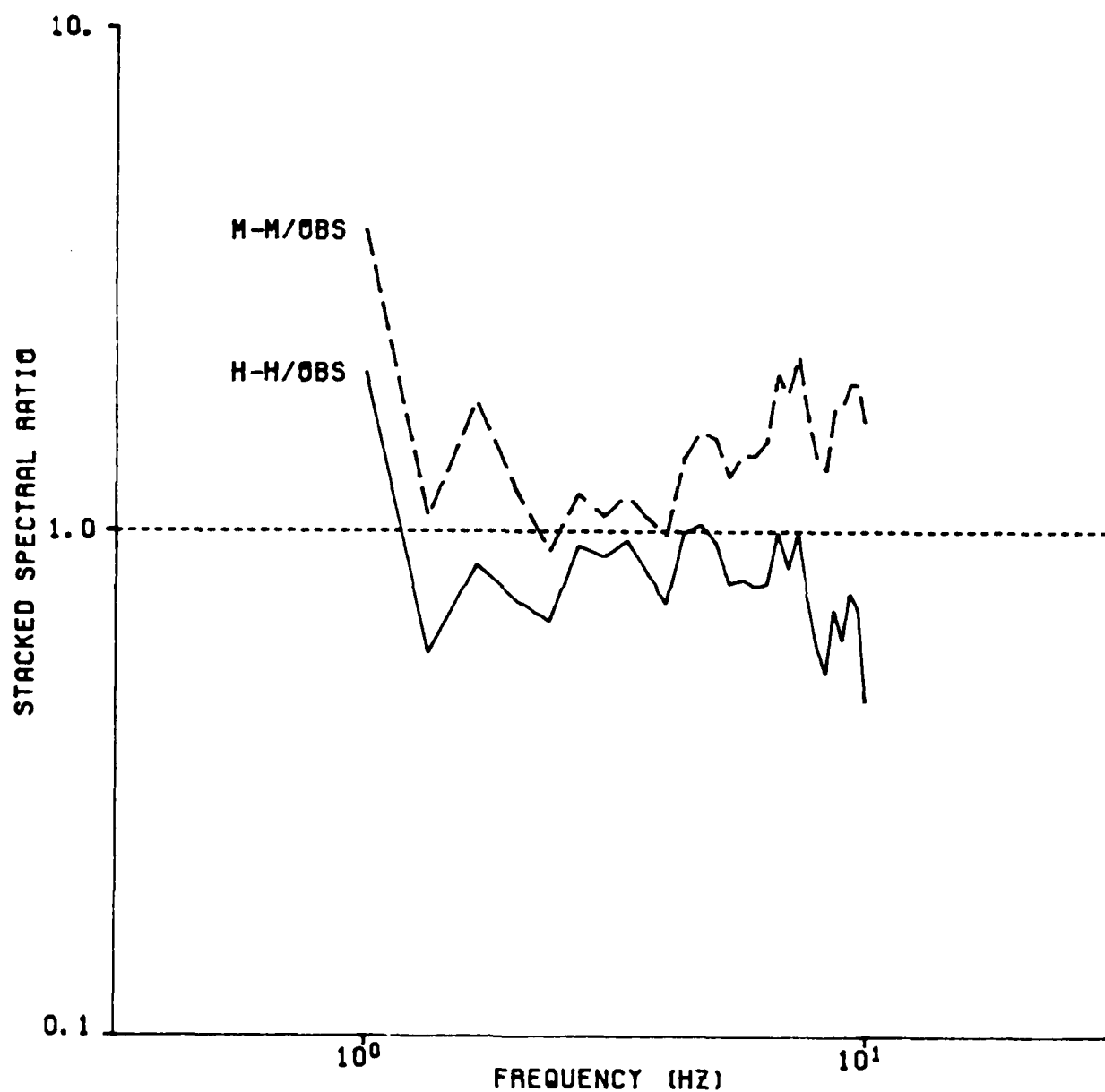


Figure 12. The average error in predicted/observed spectra for an extended window length. This is the same error measure displayed in Figure 11, but the sampling window has been extended from 2 to 3 sec.

observations do. An examination of the time domain signals displayed in the appendix makes it clear that extending the window length by a full second without adding more rays is inaccurate at high frequencies in most cases.

ATTENUATION IN THE CRUST

The preceding discussion has made it clear that the Mueller-Murphy source is too rich in high frequency energy to satisfy near-field observations from well-coupled events at Pahute Mesa when used in the analysis procedure followed by Helmberger and Hadley (1981), Burdick, et al. (1984) or Hartzell, et al. (1983). The important question is, can the procedure be modified so that the Mueller-Murphy scaled sources could be used? The key assumption to examine is that the effects of attenuation are negligible for near-field P waves. If relatively low values of Q are assumed for the crust, attenuation will obviously remove some of the high frequency energy from the Mueller-Murphy source pulse. To state the problem more precisely, can a Q distribution of depth, z , and frequency, f , be found which effectively translates the Mueller-Murphy source into the Helmberger-Hadley? If such a distribution could be found, we would compute from it an attenuation operator, A , as a function of range, r , which we would apply to our synthetic seismograms before comparing them to the data. The condition we would like to satisfy is

$$HH(t,Y) = A(r,Q(z,f)) * MM(t,Y)$$

where $*$ represents convolution. A separate attenuation operator must be computed for each path and applied to the appropriate ray before summation. Since A is a smoothing operator, the Helmberger-Hadley source is lower frequency than the Mueller-Murphy and we have very little outside constraint on Q , it is very likely that we can find a Q distribution to at least approximately satisfy this condition. The only point we will address in this discussion is what is the approximate level of crustal Q required to make the Mueller-Murphy source function acceptable. To do this we will approximate A with a Futterman operator, neglect its dependence on ray path and simply find an appropriate level for t^* . We begin by comparing the spectra of synthetics for a 1000 kt shot observed at a range of 10 km as shown in Figure 13 assuming that the effects of attenuation are negligible. Based on the discussion in the preceding section, we can assume that the Helmberger-Hadley synthetic would fit the observations whereas the Mueller-Murphy synthetic would be too high in time-domain amplitude and too rich in high frequency. We found that a t^* value of 0.03 sec makes the spectra of the two synthetics compatible as shown in Figure 14. The travel time to a range of 10 km is very nearly 3 sec so the average Q of the crust would be 100. If the average Q is as high as 300 ($t^* = 0.01$ sec), the effect of the attenuation is definitely not strong enough to make the Mueller-Murphy source acceptable. If we perform a similar calculation at 3 km, as shown in Figures 15 and 16, where travel time is about 1 sec ($t^* = 0.01$ sec for $Q = 100$) the effect of attenuation is again definitely not strong enough. In other words, the range dependence of the misfit of the Mueller-Murphy source is not consistent with a constant average crustal Q value. This is further illustrated in Figure 17 where we plot the misfit in peak time domain amplitude of all of the observations of both the

1000 KT ELASTIC VERT 10.00 KM
SIGNAL WINDOW 2.50 TO 5.50 SEC

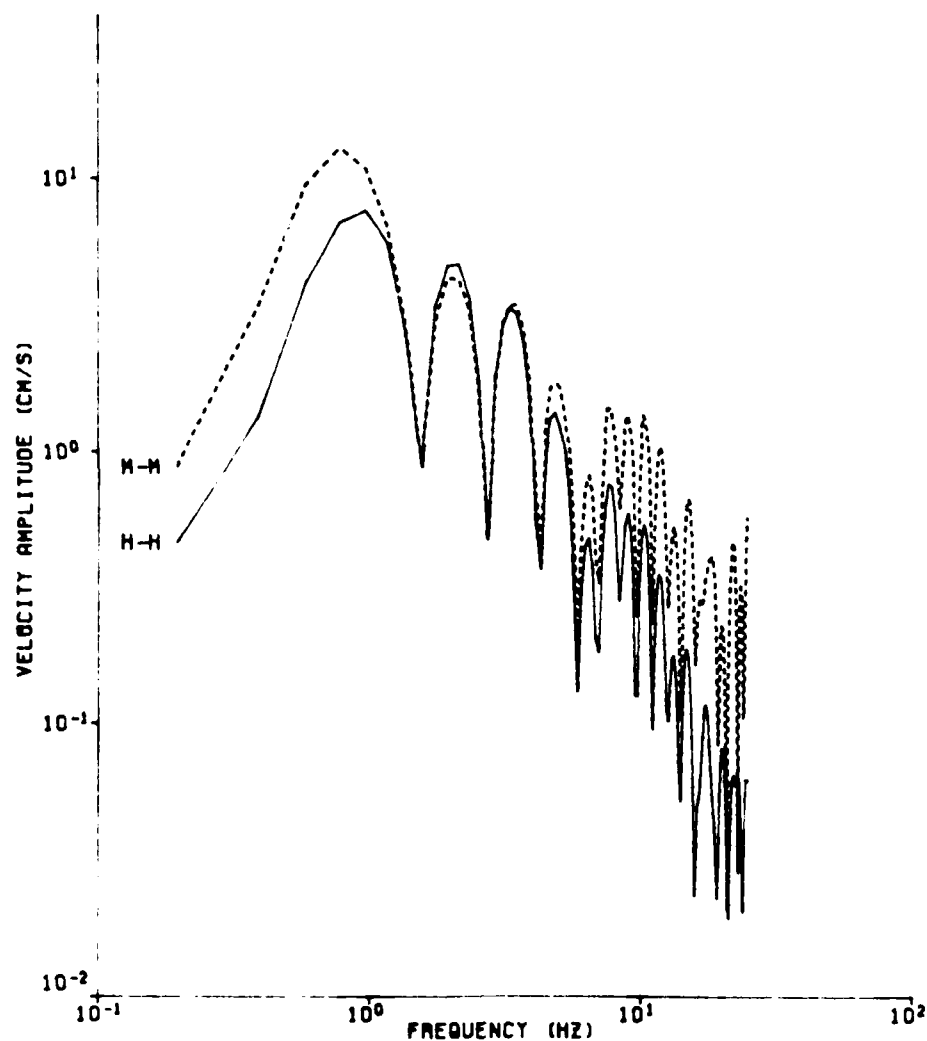
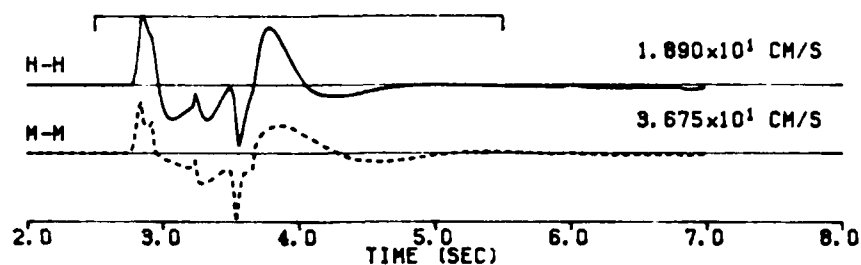


Figure 13. Synthetic spectra for a Helmlberger-Hadley (solid line) and a Mueller-Murphy (dotted line) source in the Pahute Mesa crustal structure at a range of 10 km. Yield is assumed to be 1000 kt. Crustal attenuation is assumed to be negligible. The Mueller-Murphy spectrum is significantly higher at the higher frequencies, and the amplitude in the time domain is also higher.

1000 KT Q=100 VERT 10.00 KM
 SIGNAL WINDOW 2.50 TO 5.50 SEC

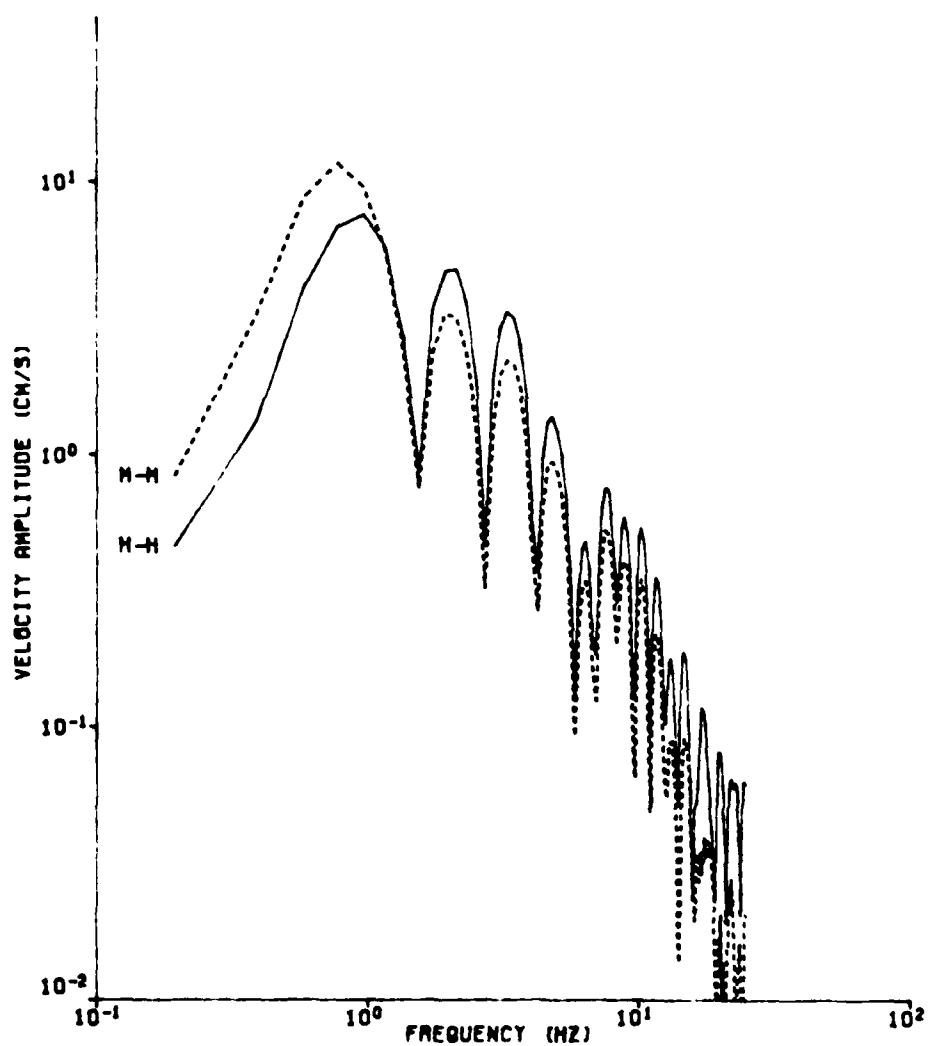
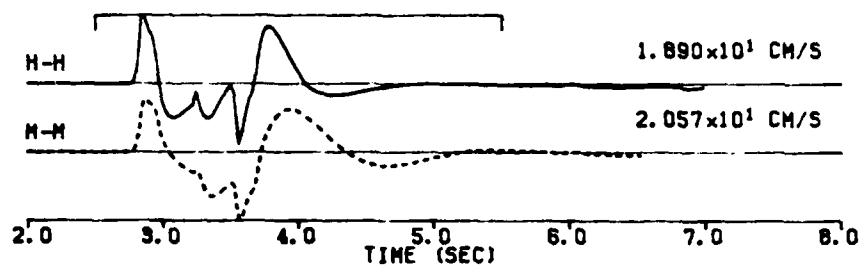


Figure 14. Synthetic spectra for a Helmlberger-Hadley (solid line) and a Mueller-Murphy (dotted line) source in the Pahute Mesa crustal structure at a range of 10 km. Yield is assumed to be 1000 kt. Average crustal Q is assumed to be 100. The spectra and time domain amplitudes now agree.

1000 KT ELASTIC VERT 3.00 KM
SIGNAL WINDOW 0.75 TO 3.00 SEC

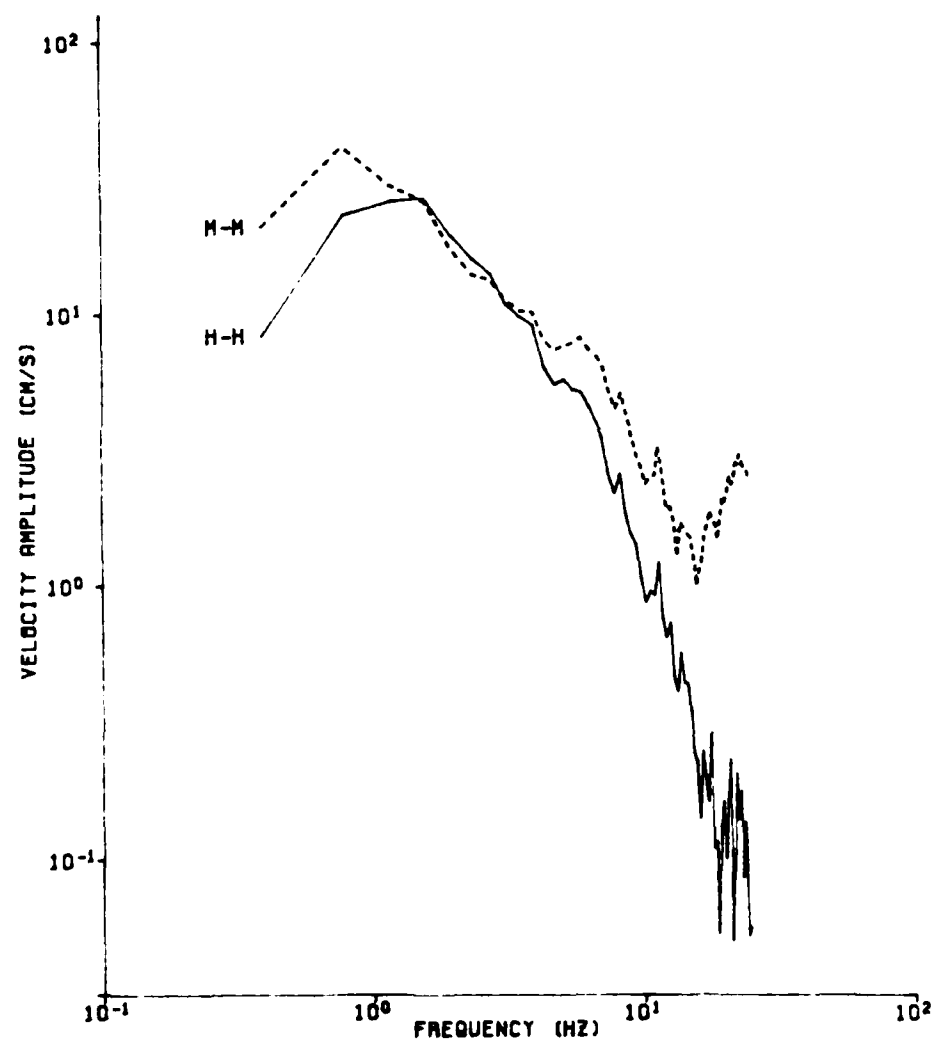
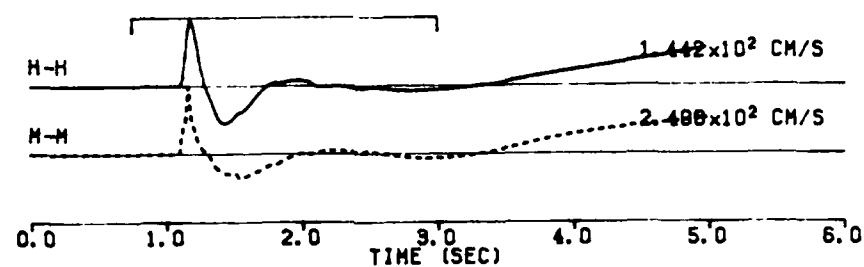


Figure 15. Synthetic spectra for a Helmlberger-Hadley (solid line) and a Mueller-Murphy (dotted line) source in the Pahute Mesa crustal structure at a range of 3 km. Yield is assumed to be 1000 kt. Crustal attenuation is assumed to be negligible. The Mueller-Murphy spectrum is significantly higher at the higher frequencies, and the amplitude in the time domain is also higher.

1000 KT Q=100 VERT 3.00 KM
 SIGNAL WINDOW 0.75 TO 3.00 SEC

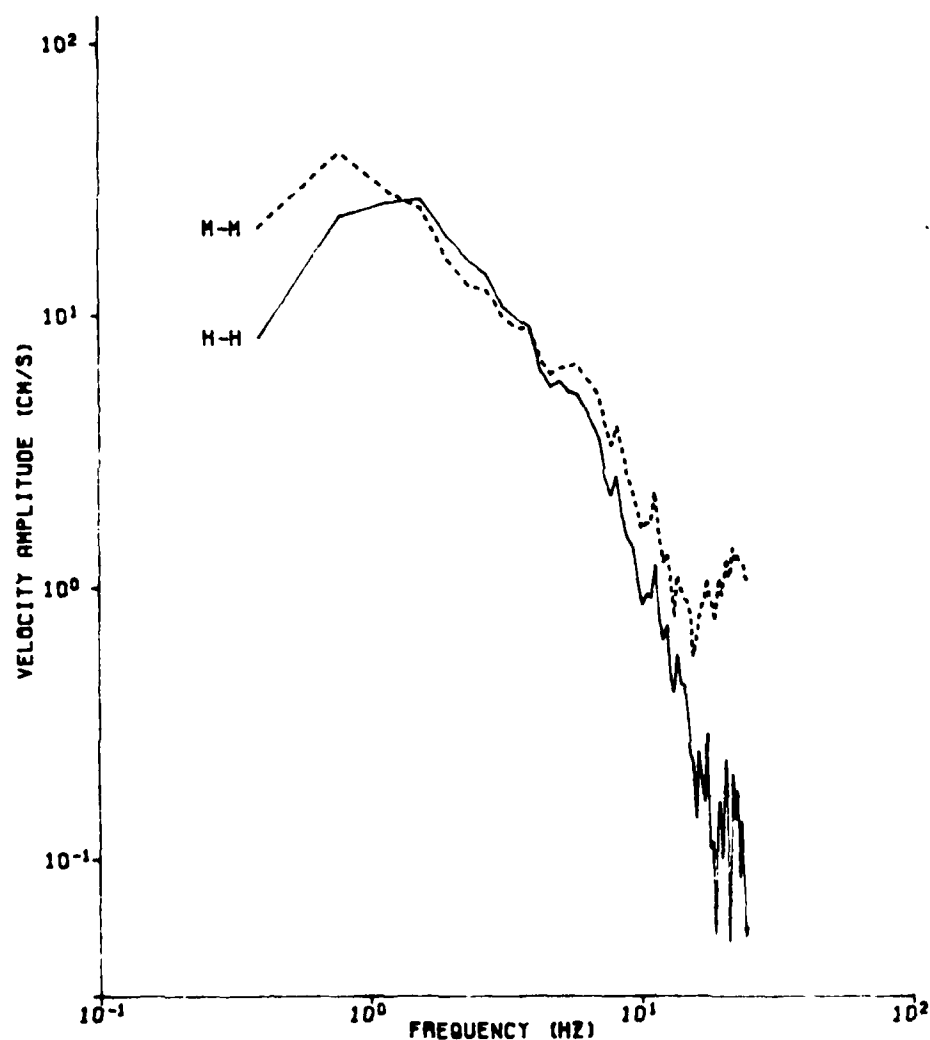
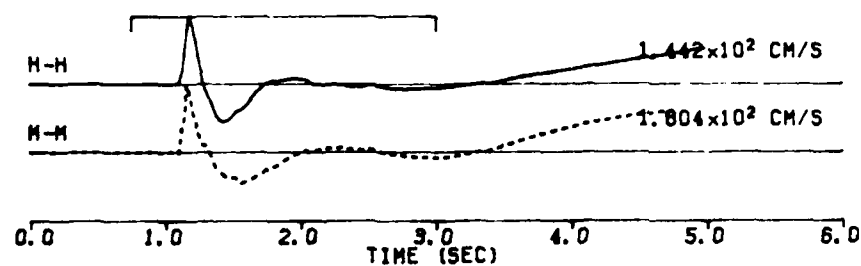


Figure 16. Synthetic spectra for a Helmberger-Hadley (solid line) and a Mueller-Murphy (dotted line) source in the Pahute Mesa crustal structure at a range of 3 km. Yield is assumed to be 1000 kt. Average crustal Q is assumed to be 100. The spectra and time domain amplitudes are still too high.

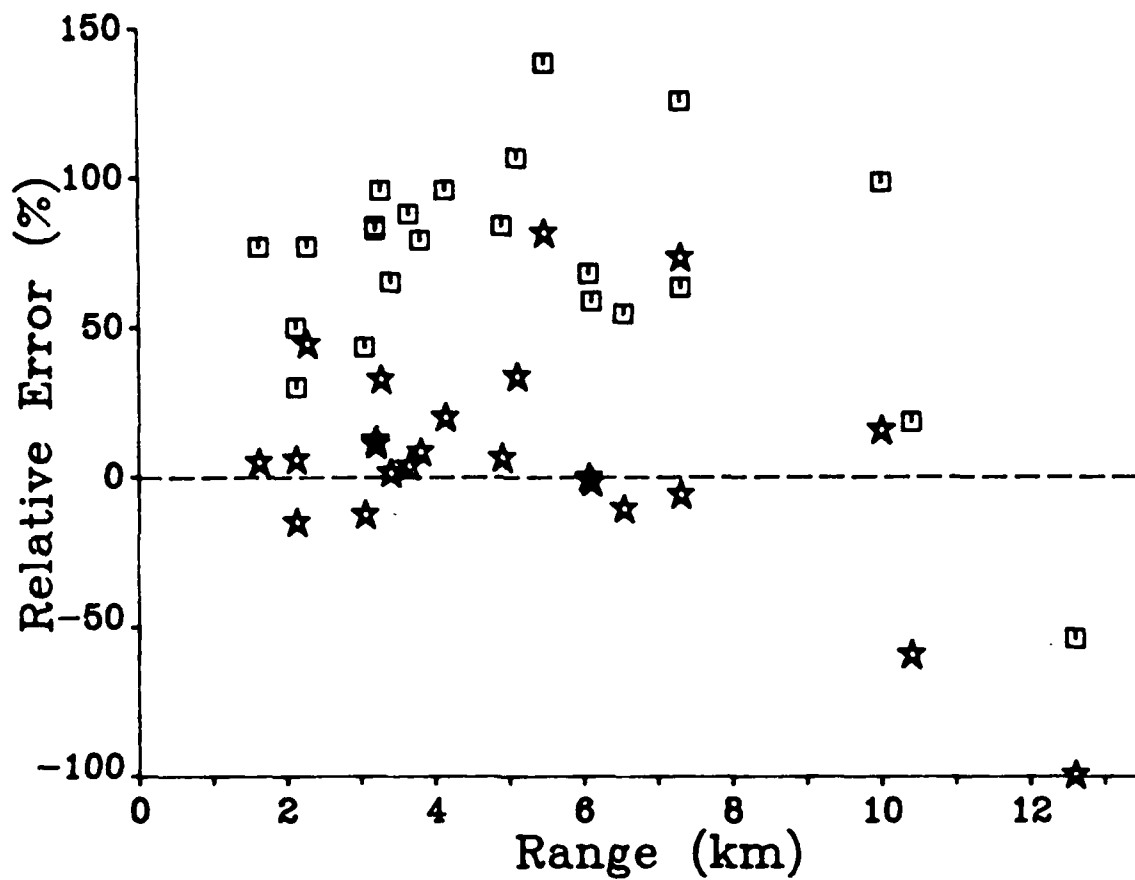


Figure 17. Relative error of the predicted versus observed time-domain amplitudes of the near-field P waves in the data set. Mueller-Murphy values are shown as squares and Helmberger-Hadley as stars.

Helmberger-Hadley and the Mueller-Murphy source as a function of range. The former fits at all ranges under the assumption of negligible attenuation while the latter is about 75% too high at all ranges. This means that if the Mueller-Murphy source is to be used, a Q distribution in the crust must be designed which causes a range independent reduction in frequency content and time-domain amplitude. Such a distribution will probably have to be fairly elaborate in detail, but if one knew a priori that the Mueller-Murphy source was correct, a suitable distribution could probably be found without much difficulty.

DISCUSSION

It is unfortunate that the results of this brief study hinge on the value of Q in the crust since it is such a poorly known quantity. If the value is in the range of 50 to 100, which is not unreasonable, then crustal attenuation has a major effect and the Mueller-Murphy source is acceptable. If it is as high as 300, which is also reasonable, then the effect is much smaller. Because of this large uncertainty, we have no clear reason for favoring one source representation over the other. Additional types of evidence will need to be considered.

One important additional constraint on the accuracy of nuclear event source representations comes from teleseismic, short period P-wave data. The amplitudes of teleseismic P waves scatter considerably, but the average value for an event appears to be a stable and meaningful quantity. Of course, the average value of t^* in the earth needs to be known to correct for attenuation

along the propagation path. What an appropriate average value for t^* is has been a subject of debate for some years, though a consensus seems to be emerging. It is important to always associate values of t^* with a frequency range since it is well established that Q does vary with frequency within the body wave band. At very long periods, such as those observed in multiple ScS waves the value of t^* for P waves exceeds 1 sec. It decreases to less than 1 sec at frequencies higher than 0.5 Hz. In an attempt to utilize this additional constraint, we measured amplitudes of the short period P waves from the Pahute Mesa events for which we had analyzed the near-field data. We used ab amplitudes (first peak to first trough) since these are known to be uncontaminated by pP. We translated the observed amplitude data into a value for m_b and then estimated t^* values on an event by event basis. The results are summarized in Table 2. On average, the Mueller-Murphy RDP predicts a t^* value for teleseismic short period P slightly in excess of 1 sec and the Helmberger-Hadley predicts a value of 0.73 sec. Again the Mueller-Murphy RDP appears to be too rich in high frequency energy. Further research on teleseismic and crustal attenuation will be needed before a firm conclusion that the Mueller-Murphy source is in significant error will be warranted.

Table 2 - t^* Estimates

Event	Mueller-Murphy	Helmberger-Hadley
	t^* (sec)	t^* (sec)
BOXCAR	1.10	0.85
ALMENDRO	0.95	0.70
MAST	1.00	0.75
HALFBEAK	0.95	0.70
INLET	1.00	0.70
SCOTCH	<u>1.10</u>	<u>0.65</u>
average	1.02	0.73

REFERENCES

- Burdick L. J., T. C. Wallace and T. Lay (1984). Modeling near field and teleseismic observations from the Amchitka test site, J. Geophys. Res., 89, 4373-4388.
- Carroll, R. D. (1966). Preliminary interpretation of geophysical logs, UE20f, Pahute Mesa, Nevada Test Site, Technical letter: Special Studies-I-37, Supplement 1, U. S. Geological Survey Open File Report.
- Hamilton, R. M. and J. H. Healy (1969). Aftershocks of the BENHAM nuclear explosion, Bull. Seismol. Soc. Am., 59, 2271-2281.
- Hartzell, S. H., L. J. Burdick and T. Lay (1983). Effective source functions for Pahute Mesa nuclear tests, Final Technical Report WCCP-R-83-3, Woodward-Clyde Consultants, Pasadena.
- Haskell, N. A. (1967). Analytic approximation for the elastic radiation from a contained underground explosion, J. Geophys. Res., 72, 2583-2587.

- Helmberger, D. V. and D. M. Hadley (1981). Seismic source functions and attenuation from local and teleseismic observations of the NTS events JORUM and HANDLEY, Bull. Seismol. Soc. Am., 71, 51-67.
- Lay, T., D. V. Helmberger and D. G. Harkrider (1985). Source models and yield scaling laws for the underground nuclear explosions at Amchitka Island, Bull. Seismol. Soc. Am., 74, 843-862.
- Mueller R. A. and J. R. Murphy (1971). Seismic characteristics of underground nuclear detonations, Part I Seismic scaling law of underground detonations, Bull. Seismol. Soc. Am., 61, 1675-1692.
- von Seggern, D. and R. Blandford (1972). Source time functions and spectra for underground nuclear explosions, Geophys. J. Roy. astr. Soc., 31, 83-97.

APPENDIX

The following figures present the observed and synthetic velocity waveforms and amplitude spectra for the 24 near-field records analyzed in this study. In each figure, the event name, station identification, gage type (vertical velocity in all cases), and station range are indicated at the top of the plot. The window applied to the time domain waveforms is indicated above the waveforms. The window is 2 seconds in total duration with a 0.25 sec cosine taper applied at each end, so the length of unaltered signal being Fourier transformed is 1.5 sec. The spectra are direct transforms of the velocity waveforms, so are true velocity amplitude spectra. Because of windowing effects at low frequencies and noise at high frequencies, only the portions of the spectra from 1 to 10 Hz are plotted. The observed (OBS) waveforms and spectra are plotted as solid lines, the Helmberger-Hadley synthetics (H-H) are dashed and the Mueller-Murphy synthetics (M-M) are dotted. The peak trace amplitude of the time domain waveforms is printed to the right of each trace.

BOXCAR S-12 UV 3.80 KM
SIGNAL WINDOW 1.05 TO 3.05 SEC

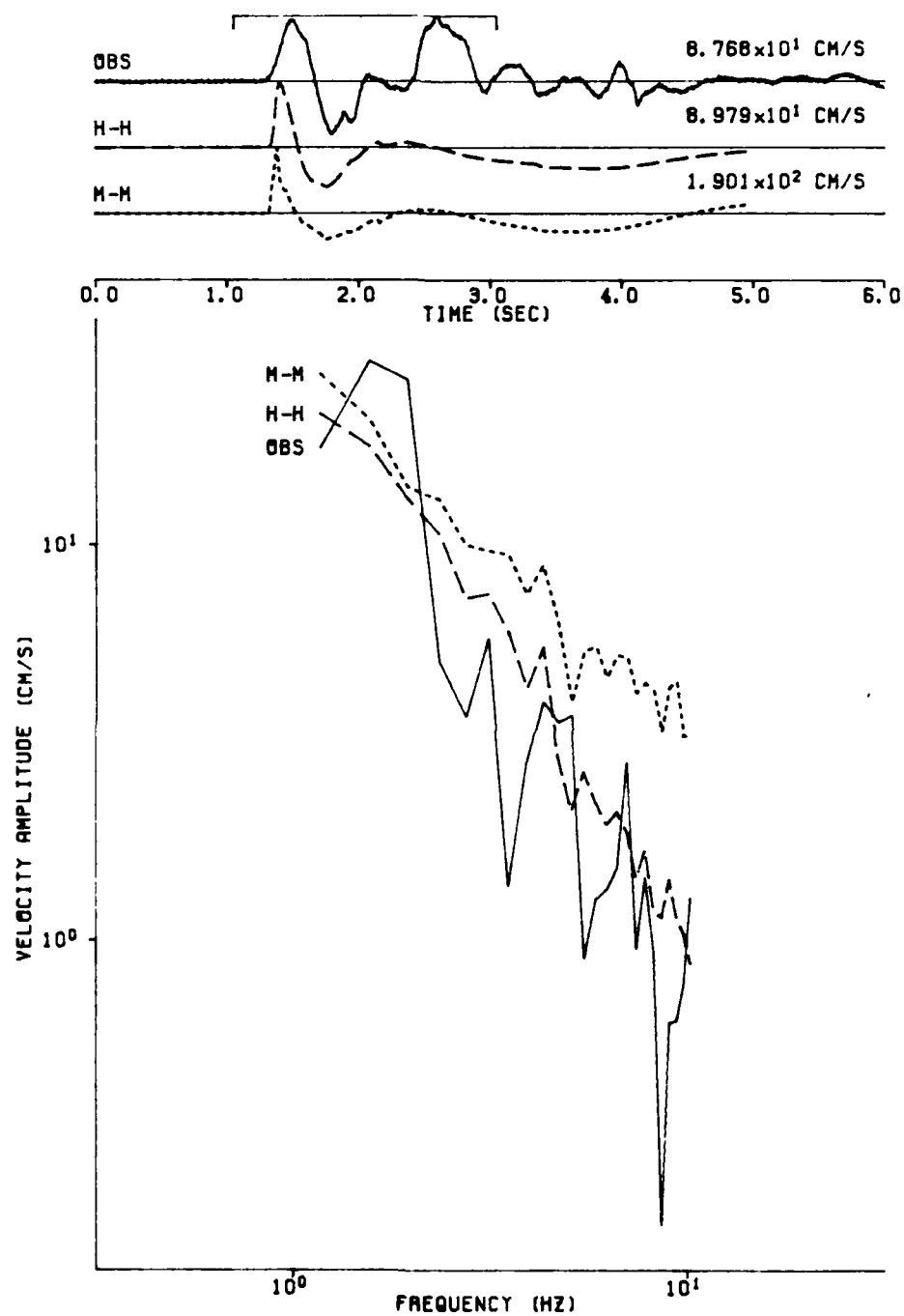


Figure A.1.

BOXCAR S-16 UV 4.90 KM
SIGNAL WINDOW 1.30 TO 3.30 SEC

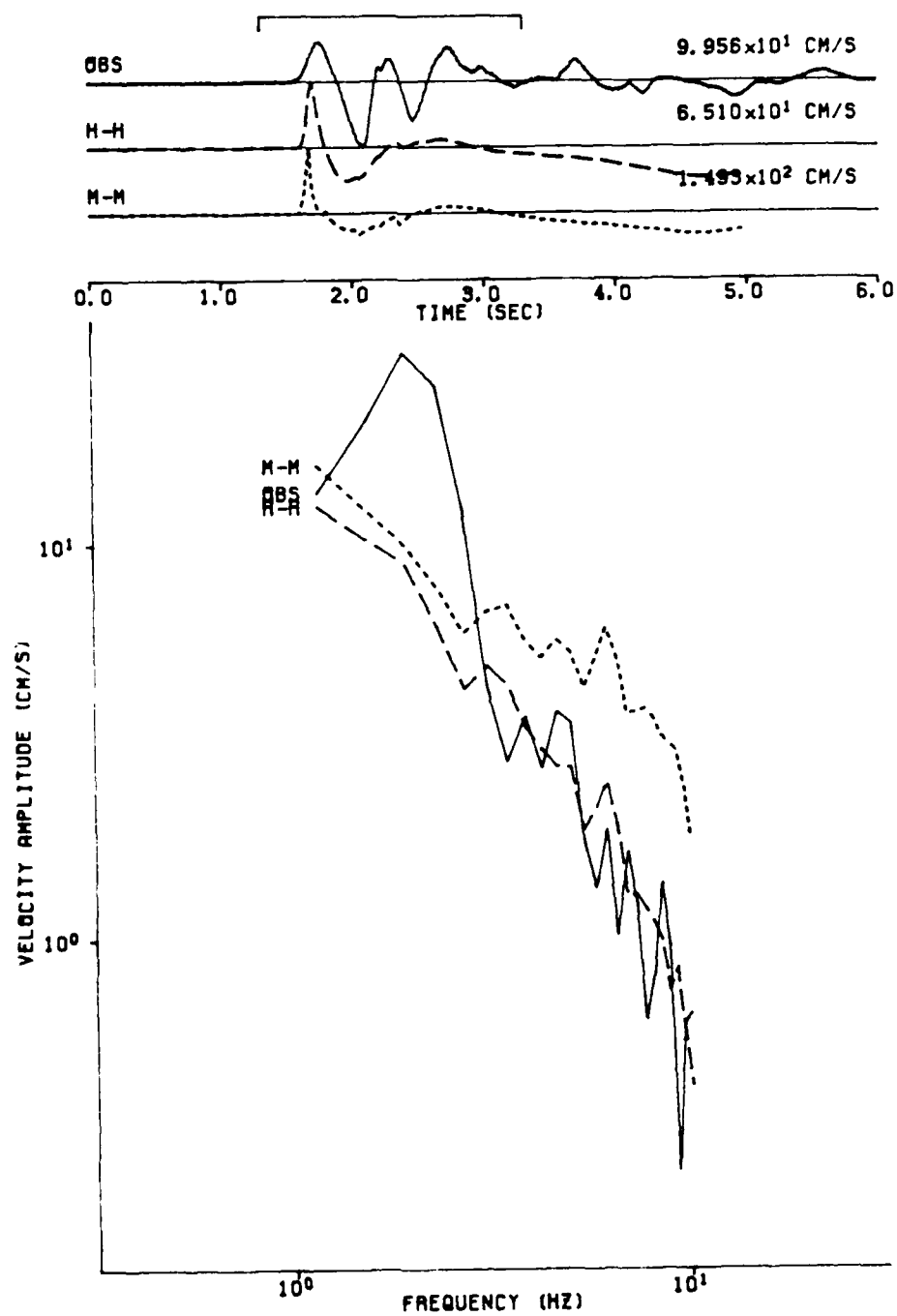


Figure A.2.

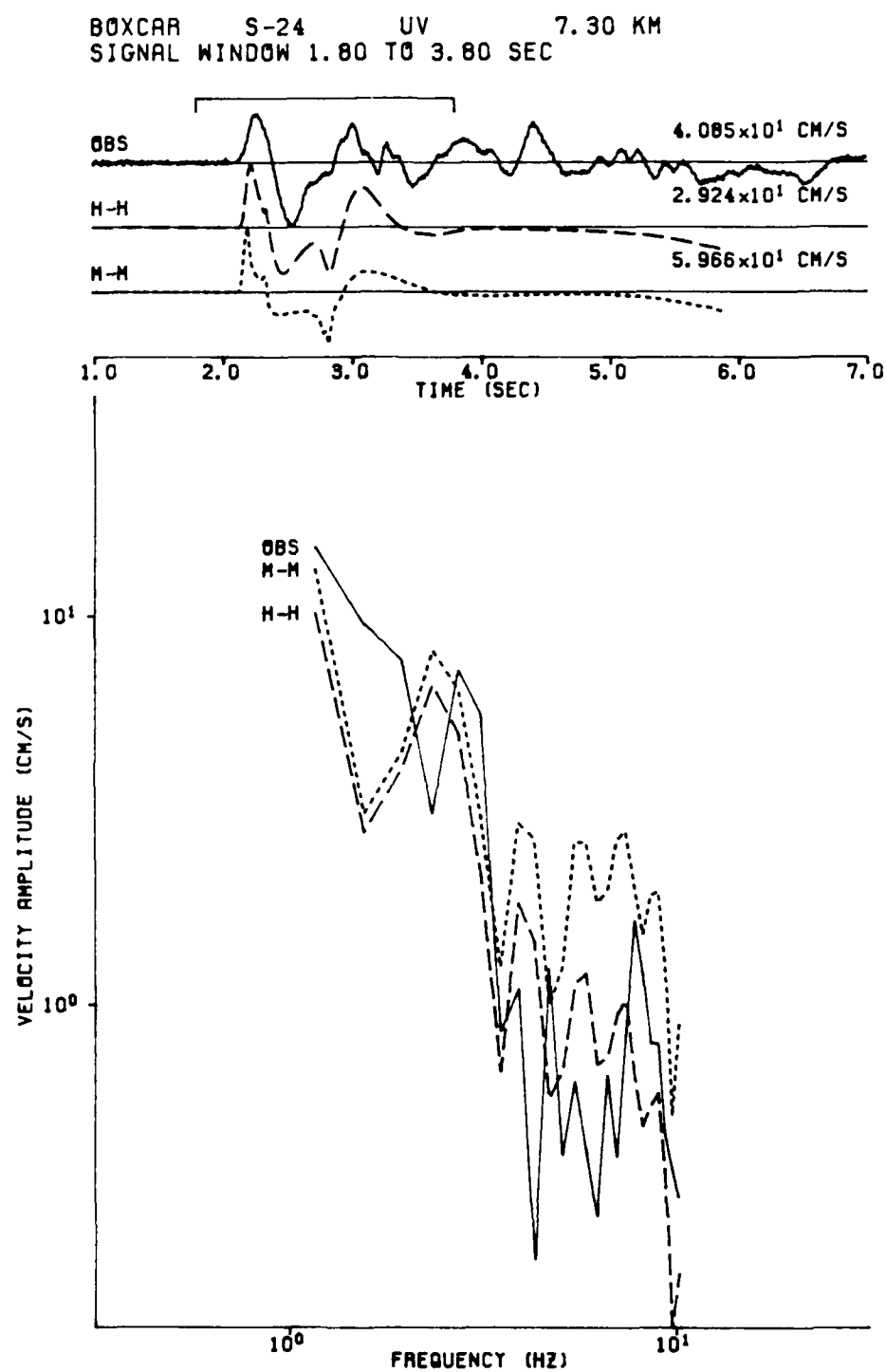


Figure A.3.

BOXCAR S-34 UV 10.40 KM
SIGNAL WINDOW 2.70 TO 4.70 SEC

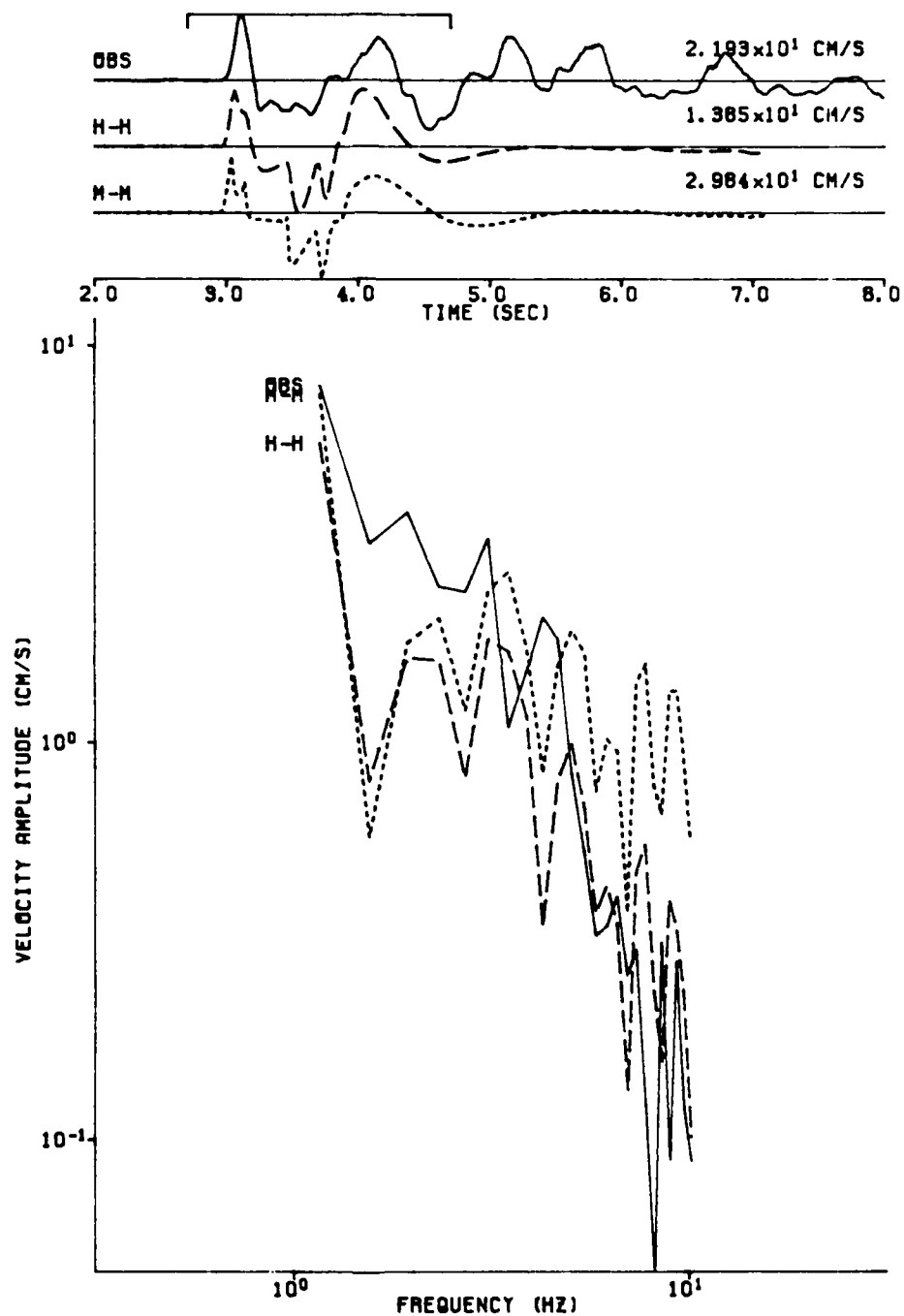


Figure A.4.

BOXCAR S-74 UV 22.47 KM
SIGNAL WINDOW 4.60 TO 6.60 SEC

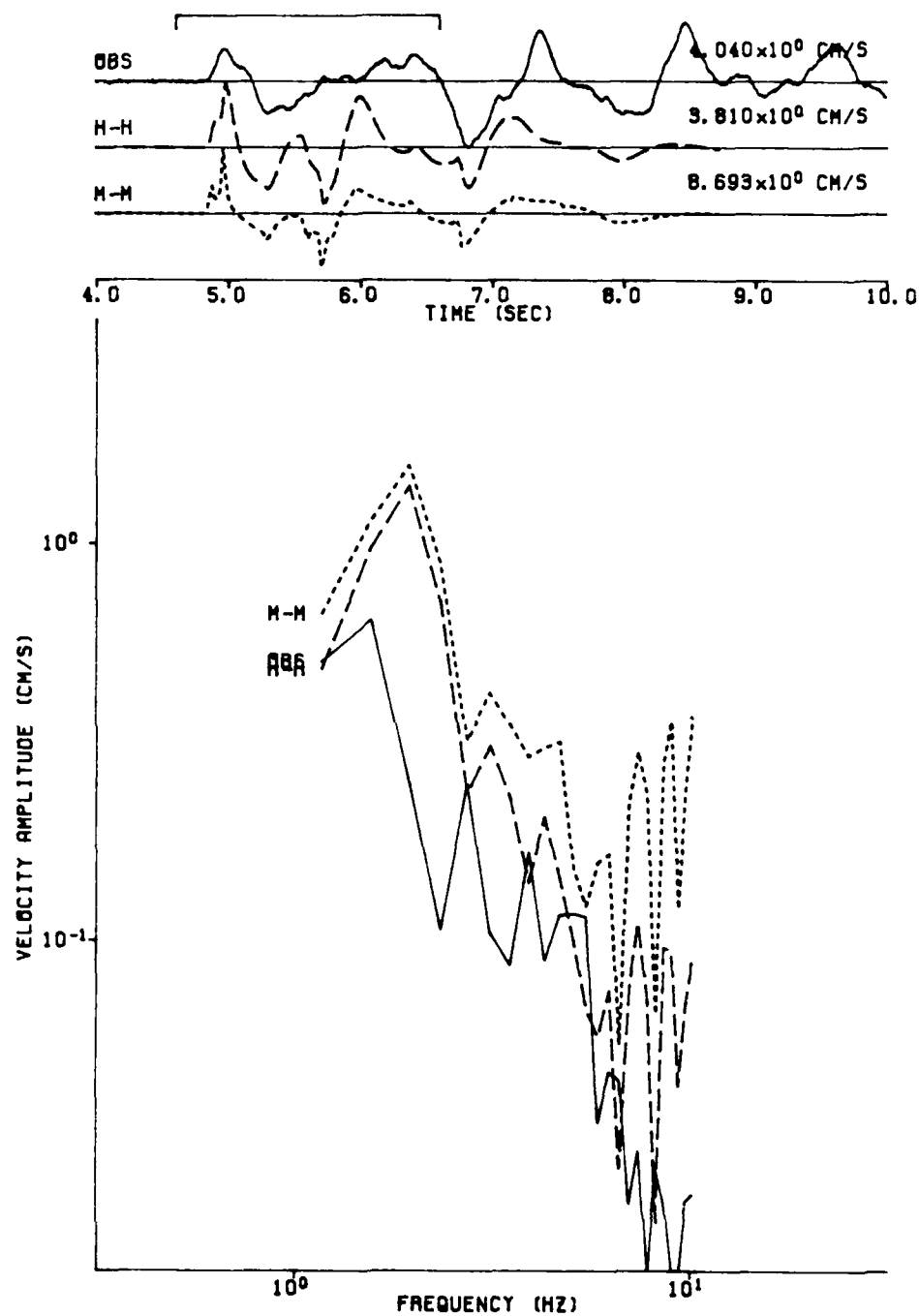


Figure A.5.

ALMENDRO L-03 UVH 3.20 KM
SIGNAL WINDOW 0.80 TO 2.80 SEC

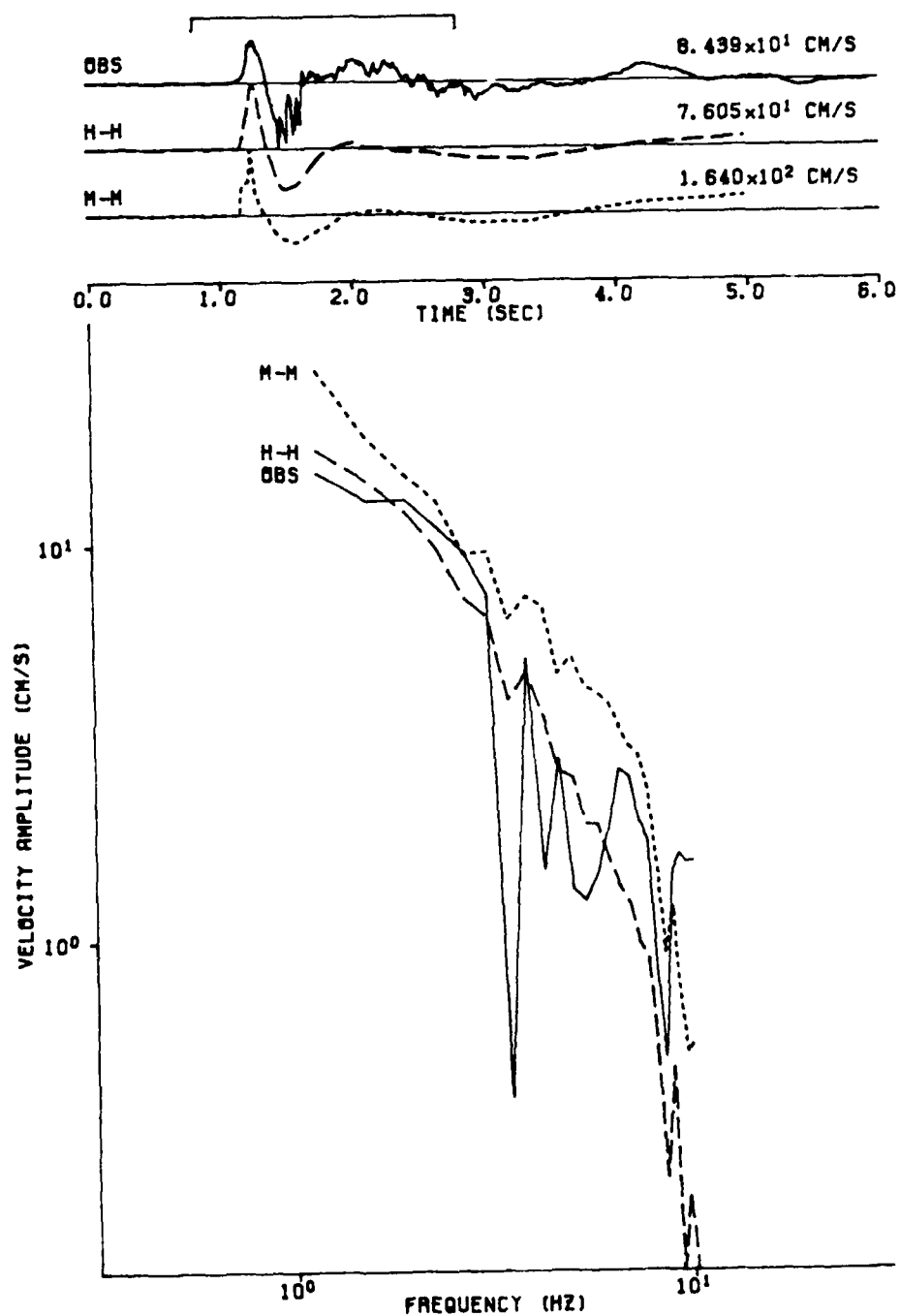


Figure A.6.

ALMENDRO L-04 UVH 3.20 KM
SIGNAL WINDOW 0.90 TO 2.90 SEC

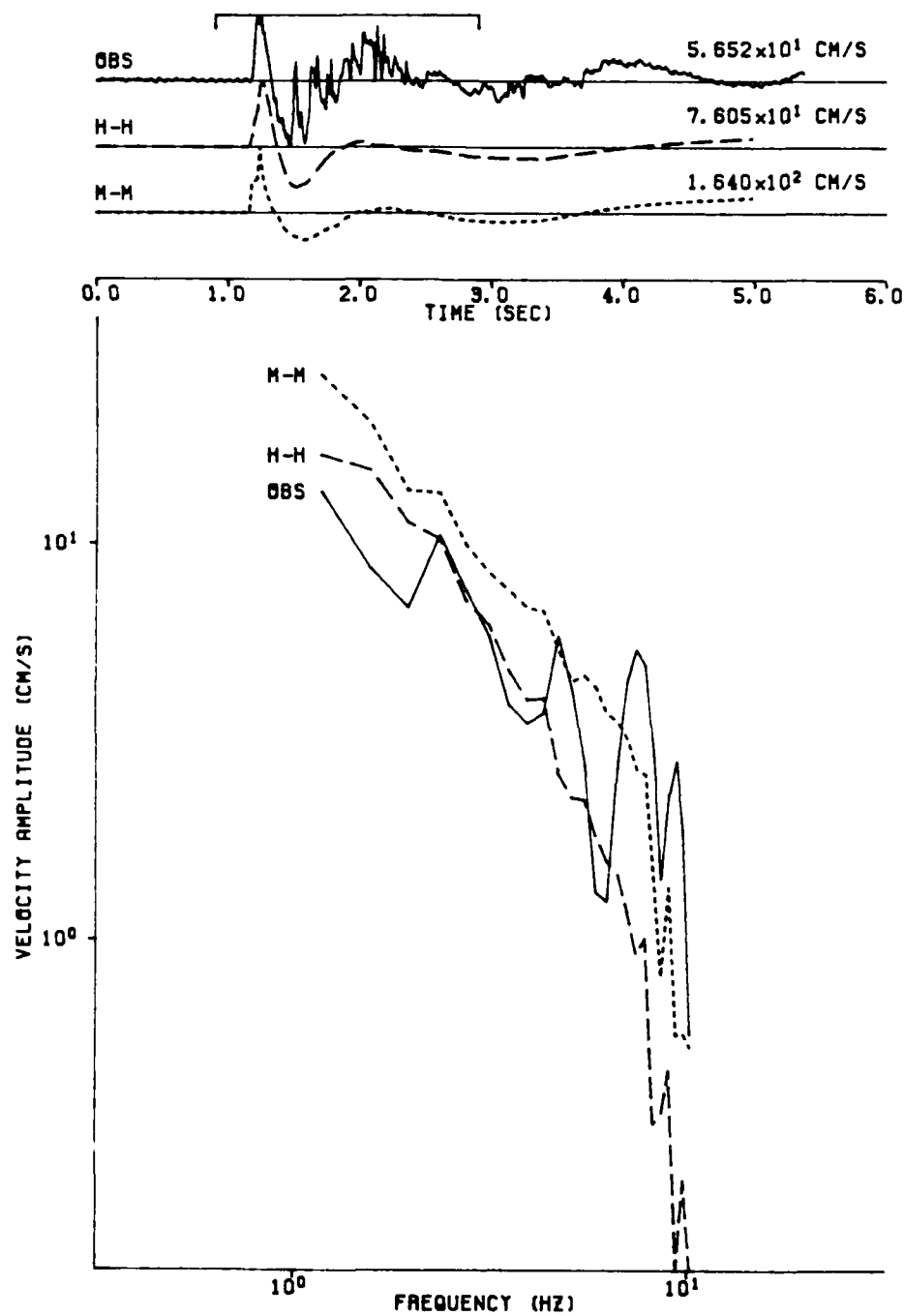


Figure A.7.

ALMENDRO ECHO PEAK UVH 3.40 KM
SIGNAL WINDOW 1.10 TO 3.10 SEC

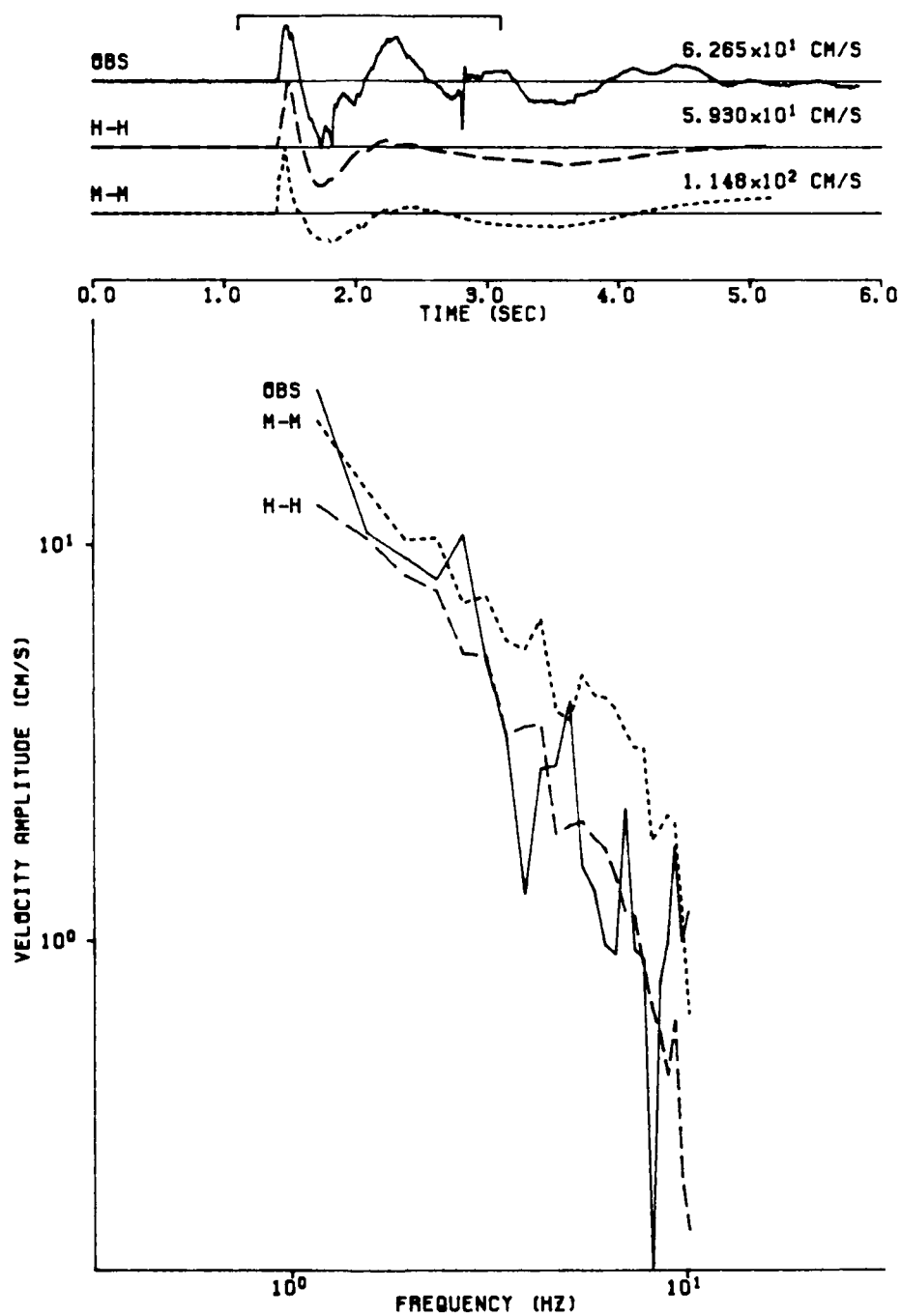


Figure A.8.

ALMENDRO L-05 UVH 5.10 KM
SIGNAL WINDOW 1.40 TO 3.40 SEC

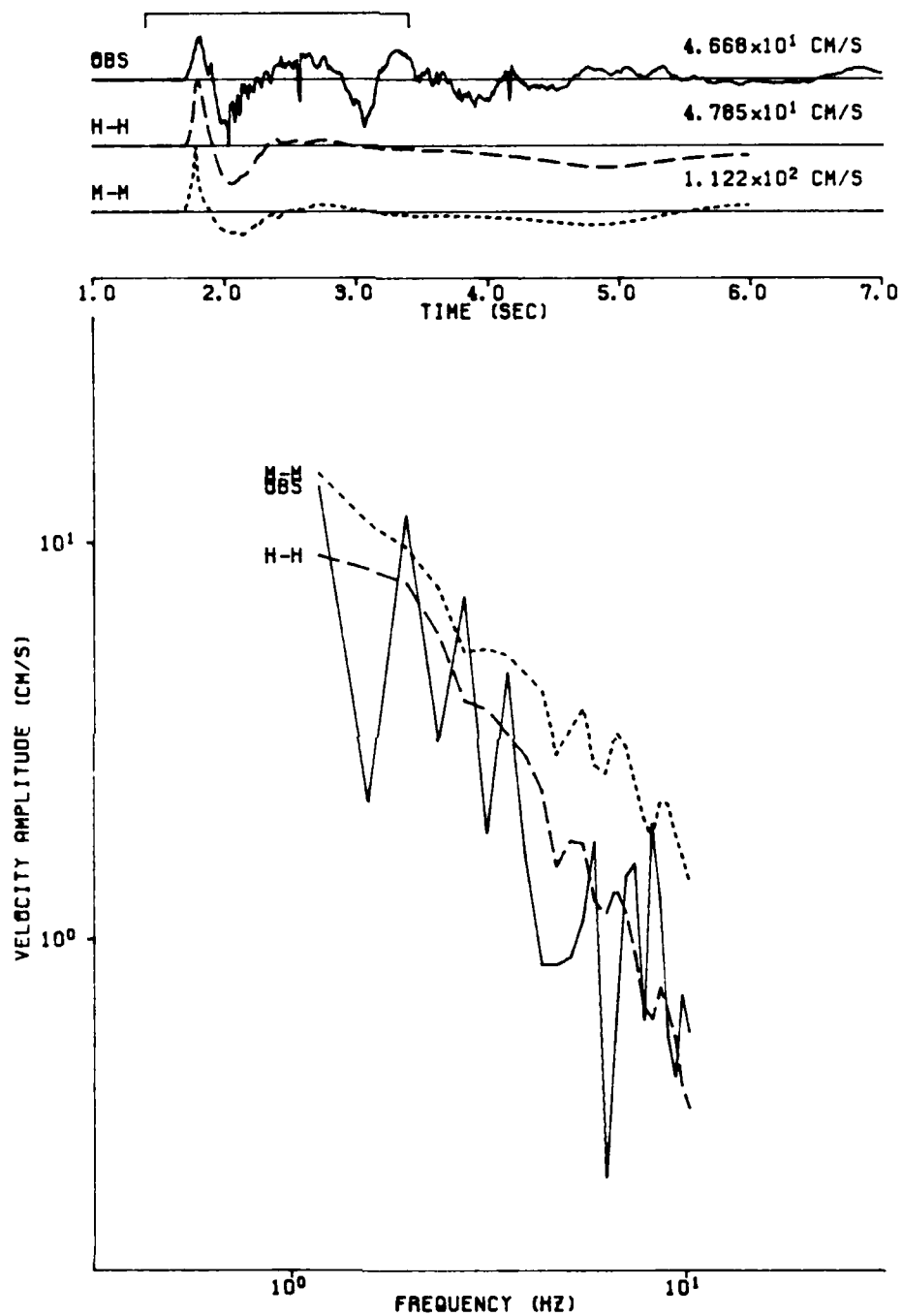


Figure A.9.

ALMENDRO L-02 UVH 6.10 KM
SIGNAL WINDOW 1.60 TO 3.60 SEC

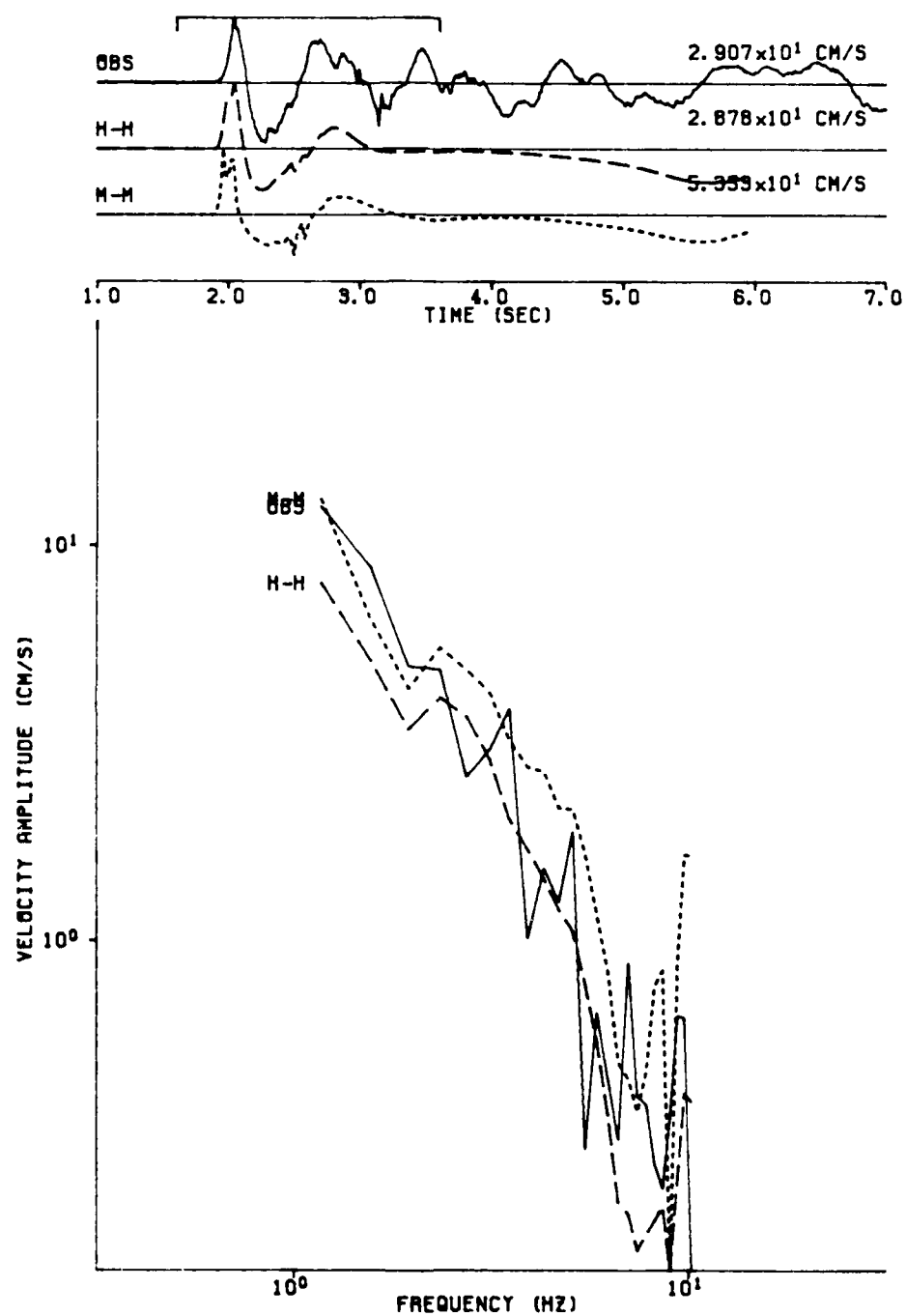


Figure A.10.

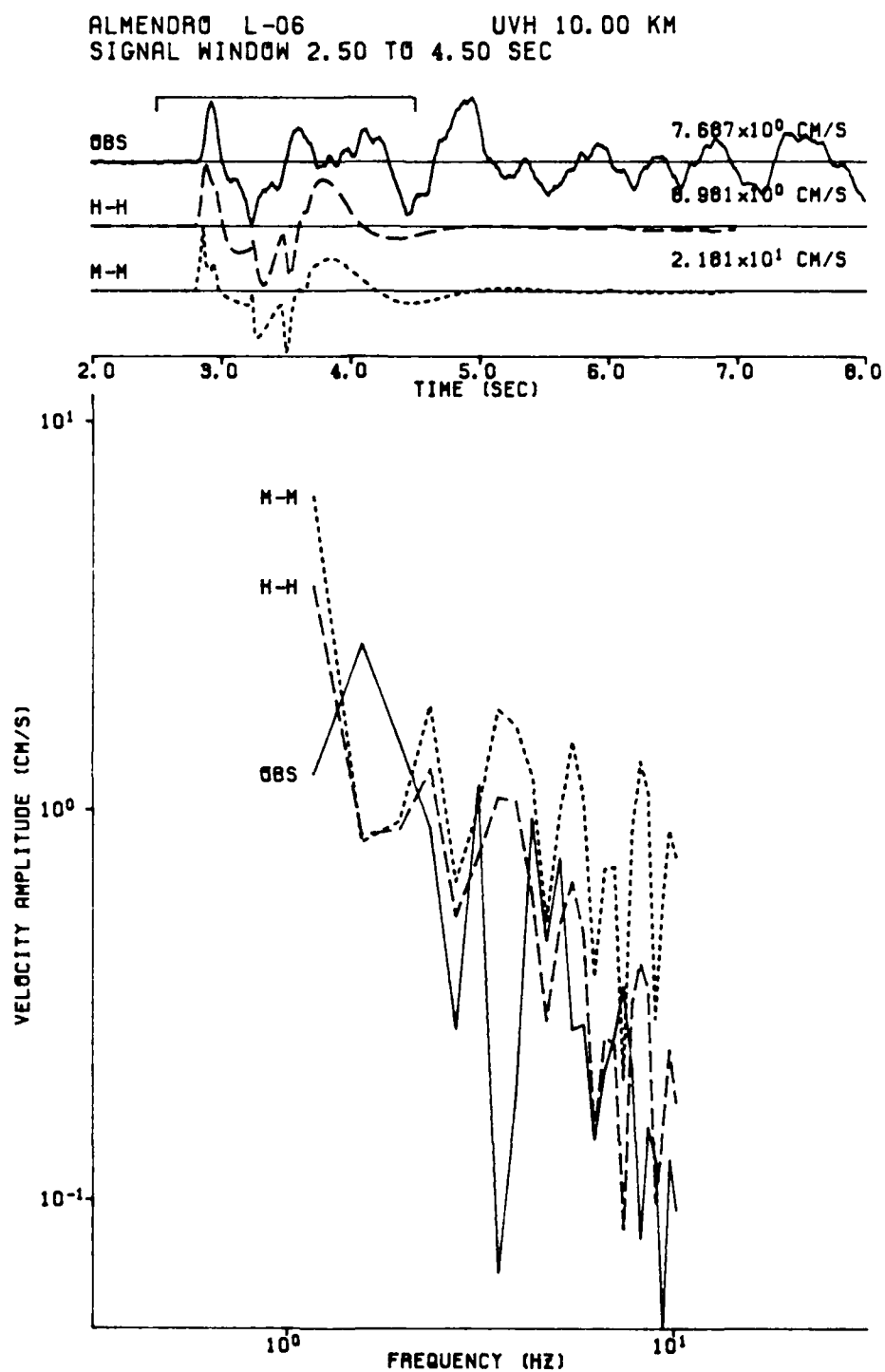


Figure A.11.

ALMENDRO L-01 UVH 12.60 KM
SIGNAL WINDOW 3.00 TO 5.00 SEC

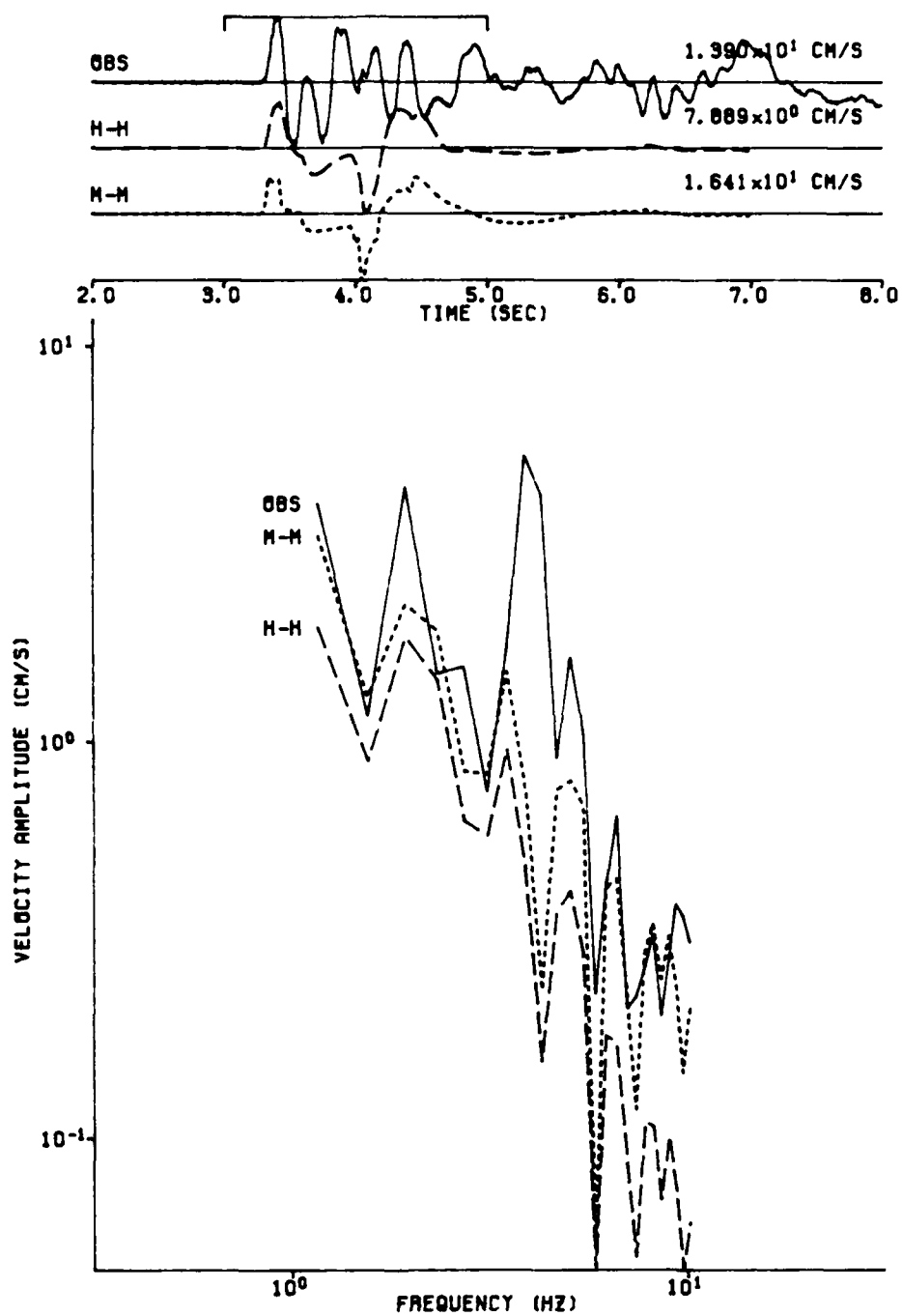


Figure A.12.

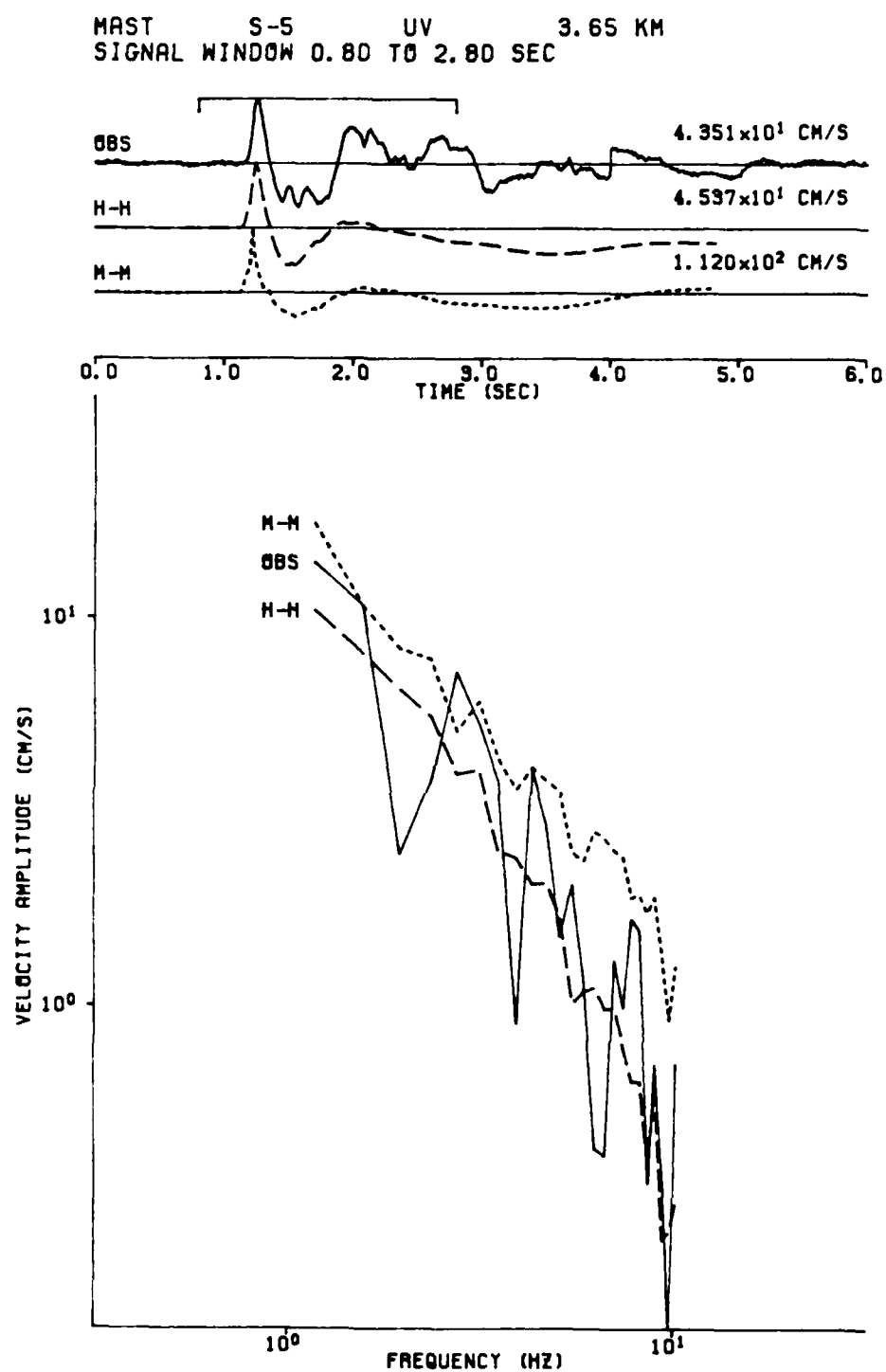


Figure A.13.

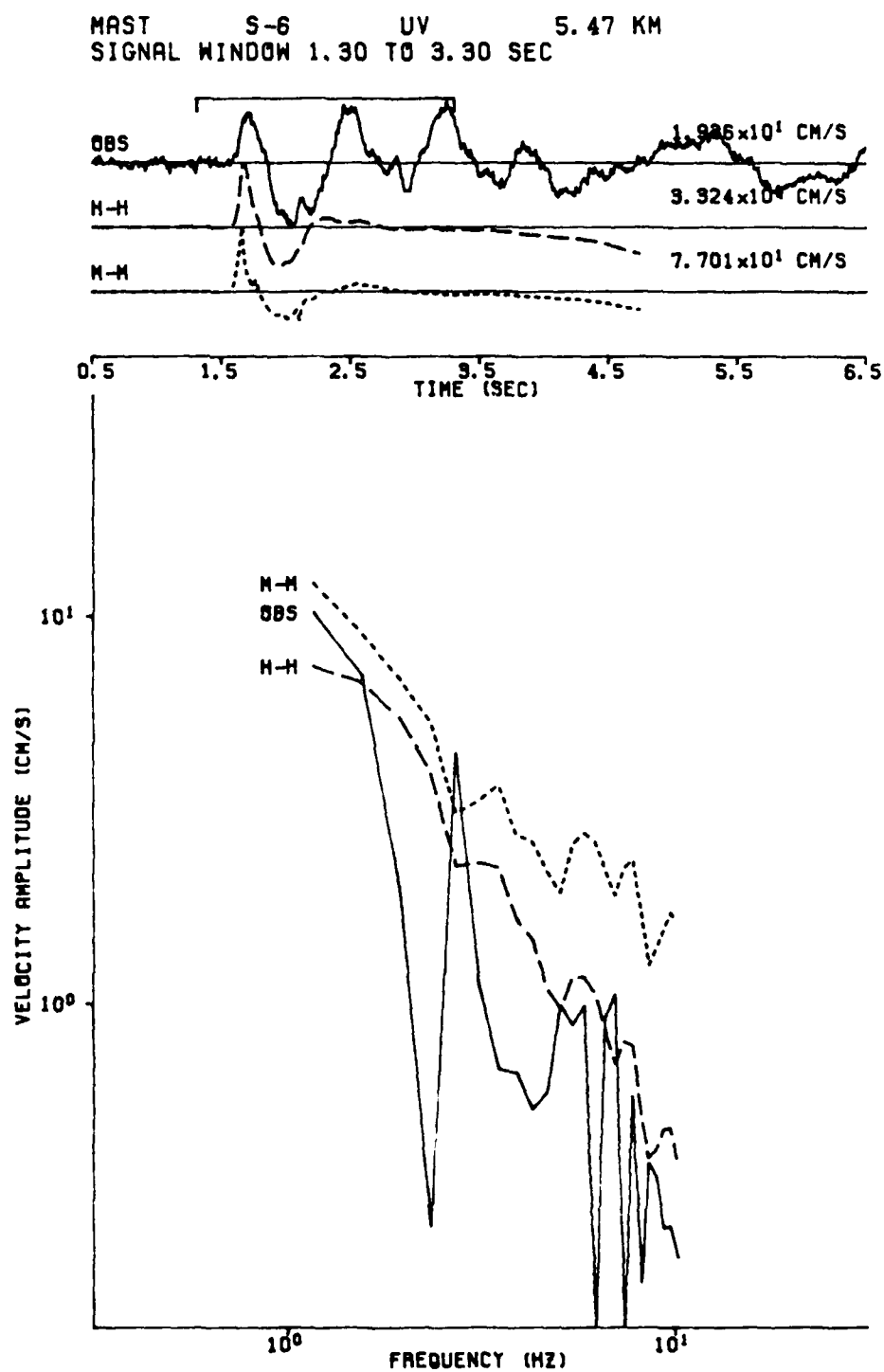


Figure A.14.

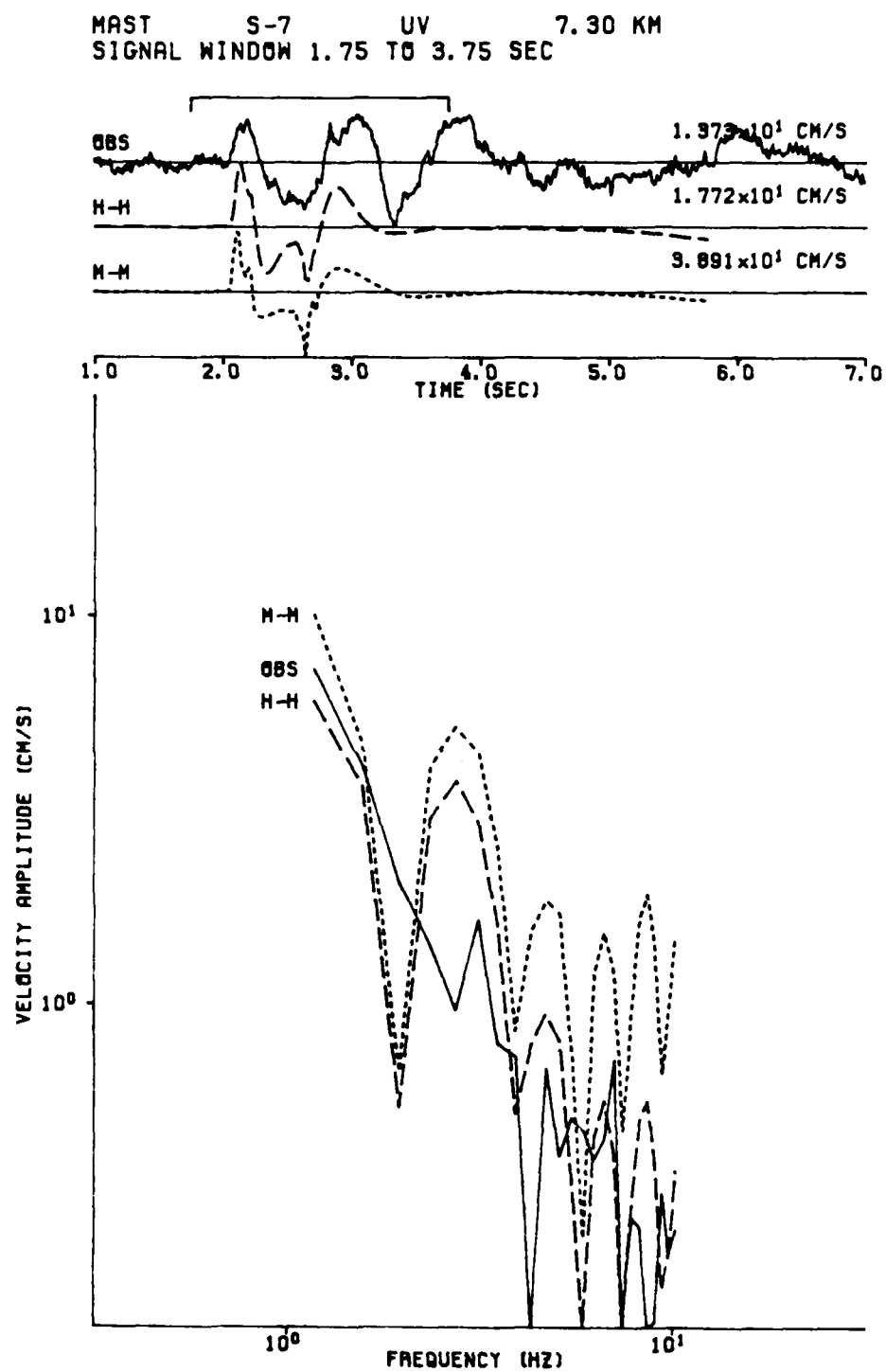


Figure A.15.

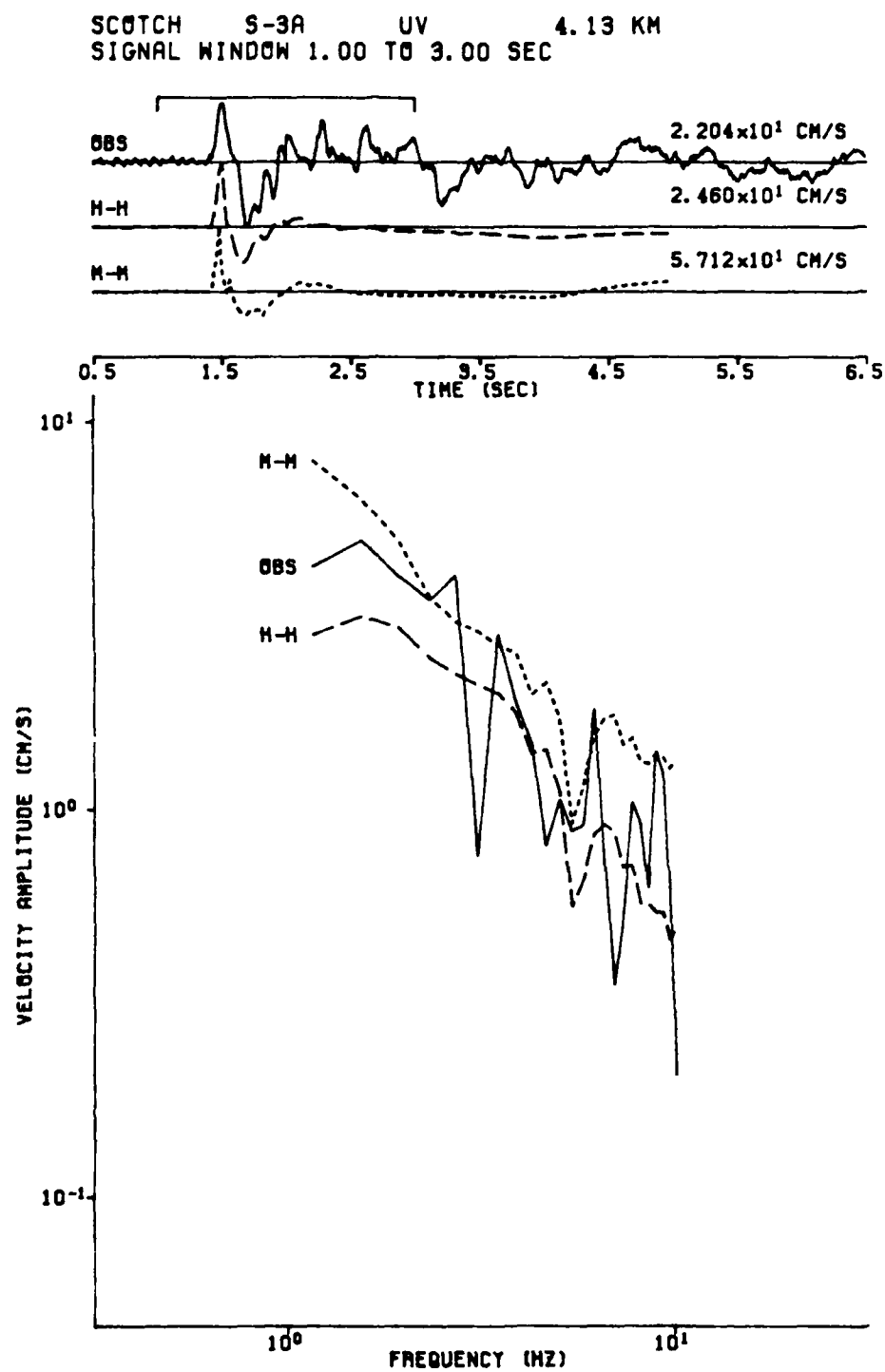


Figure A.16.

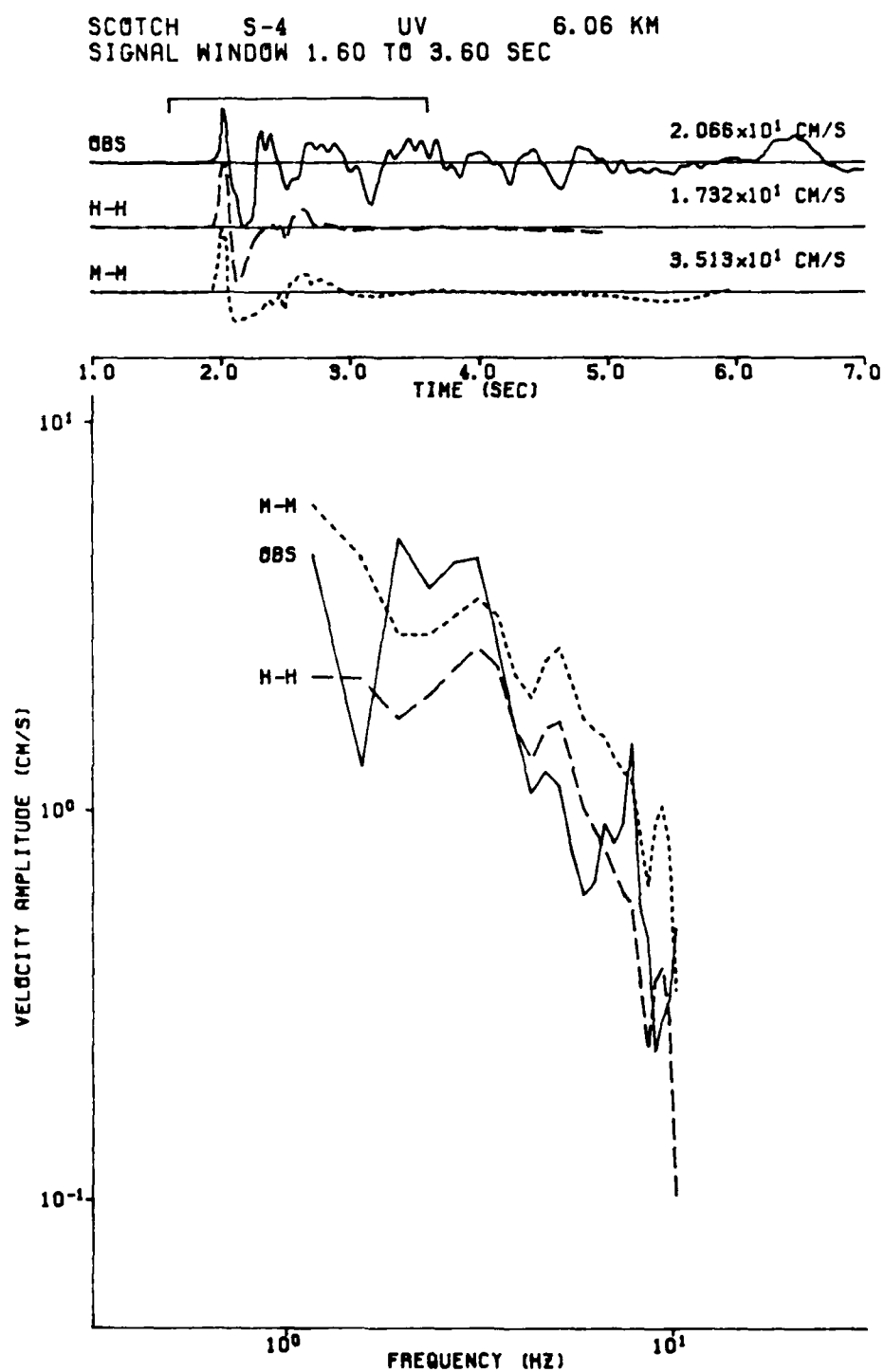


Figure A.17.

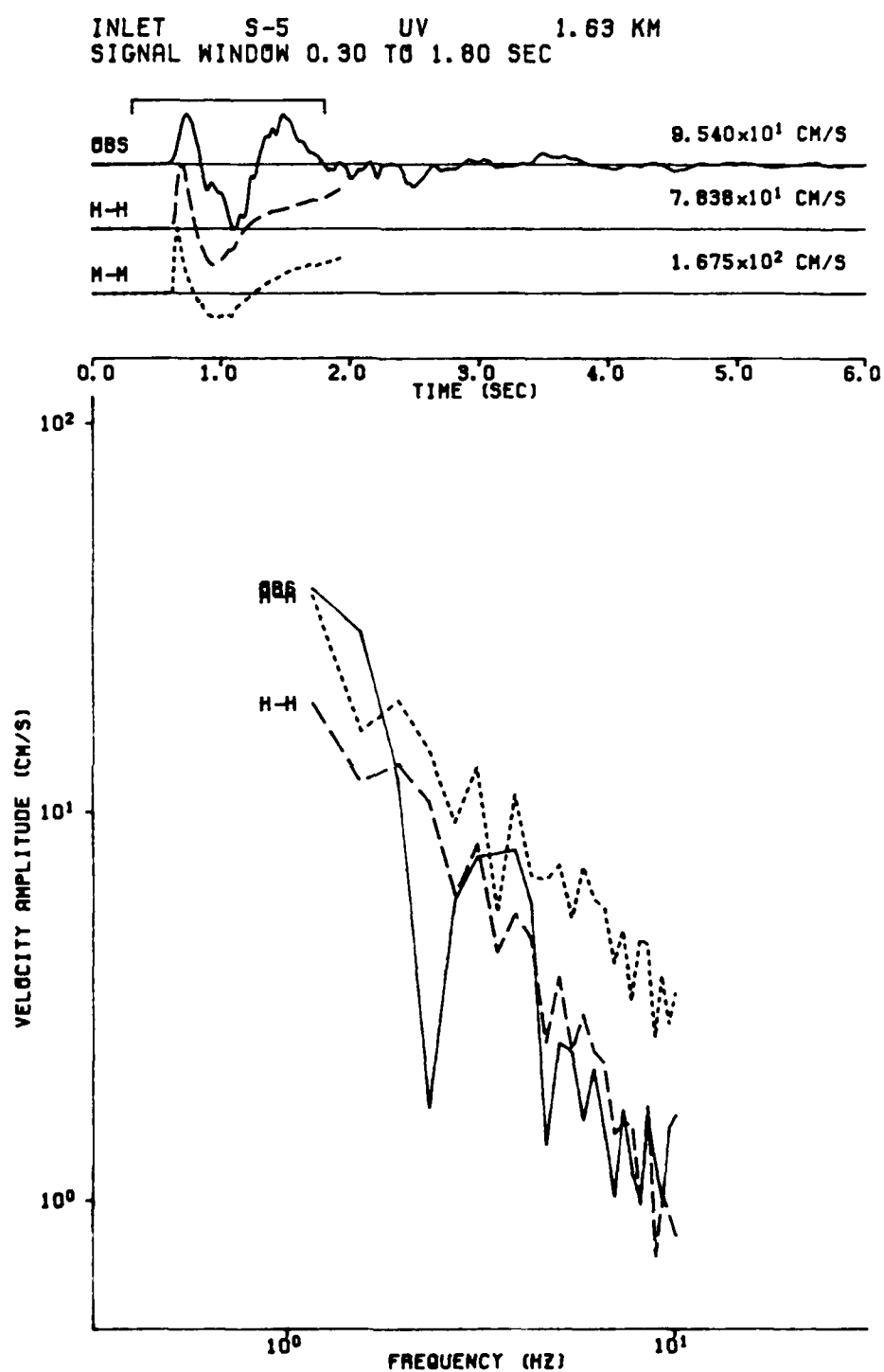


Figure A.18.

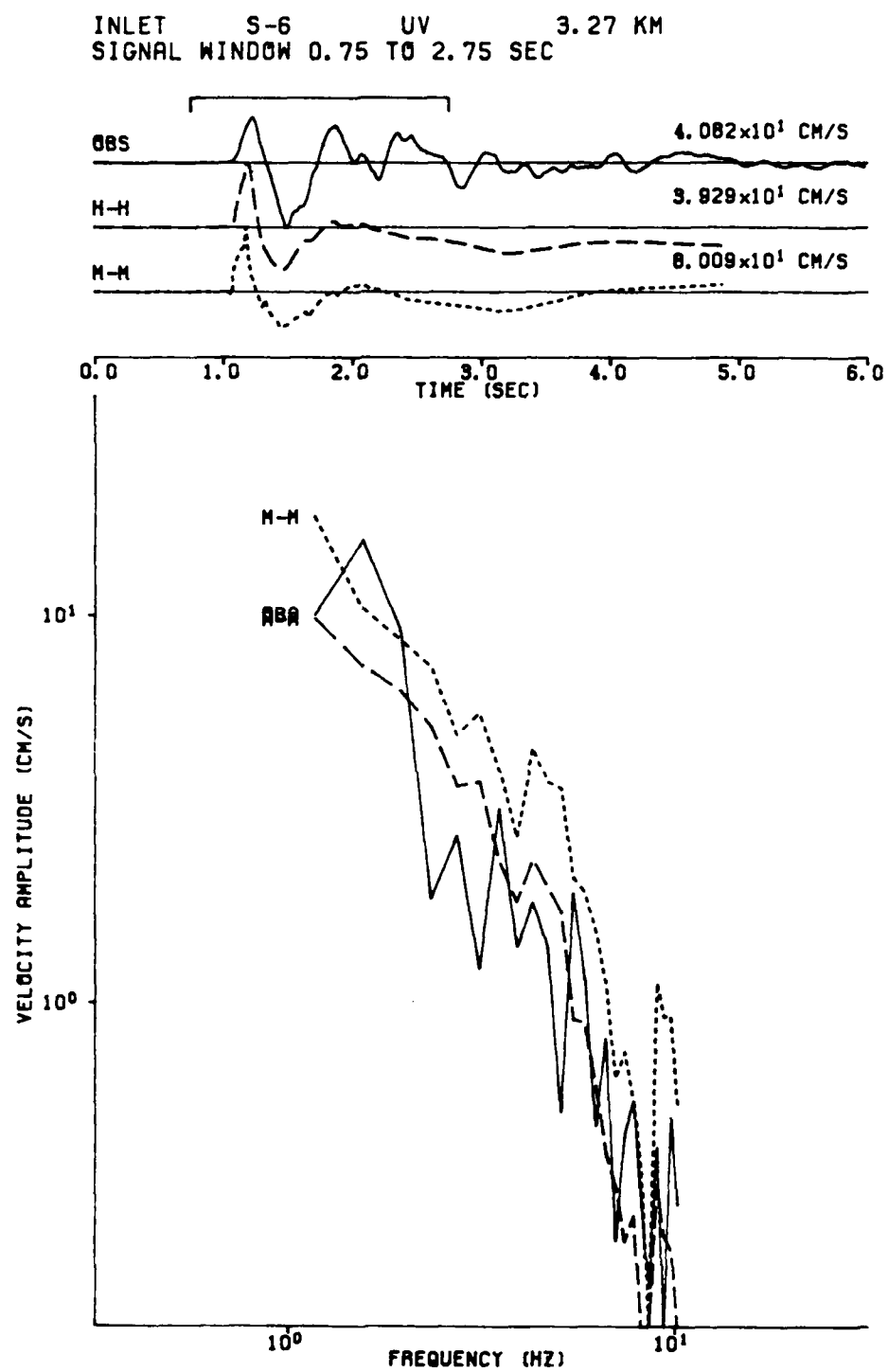


Figure A.19.

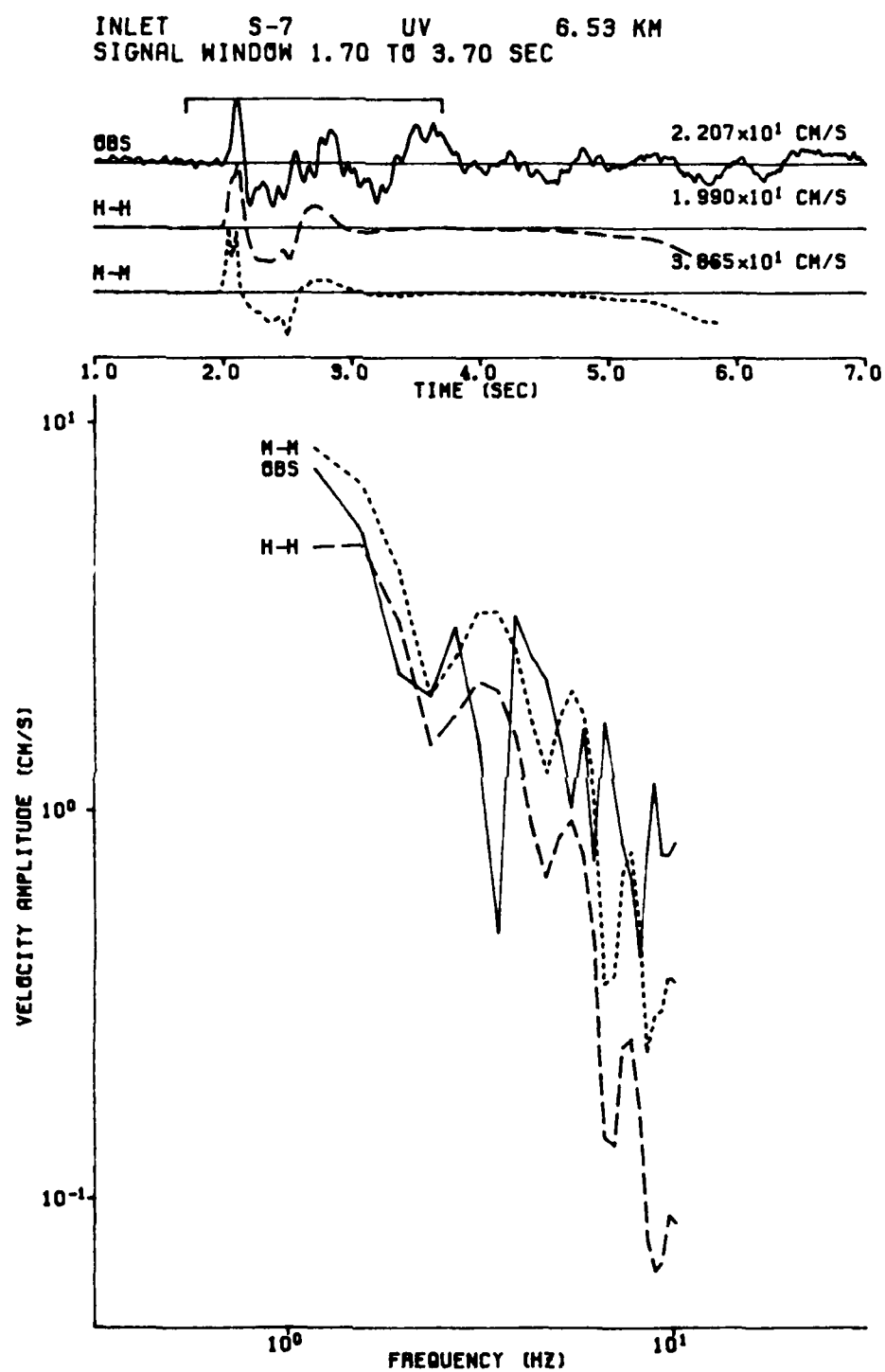


Figure A.20.

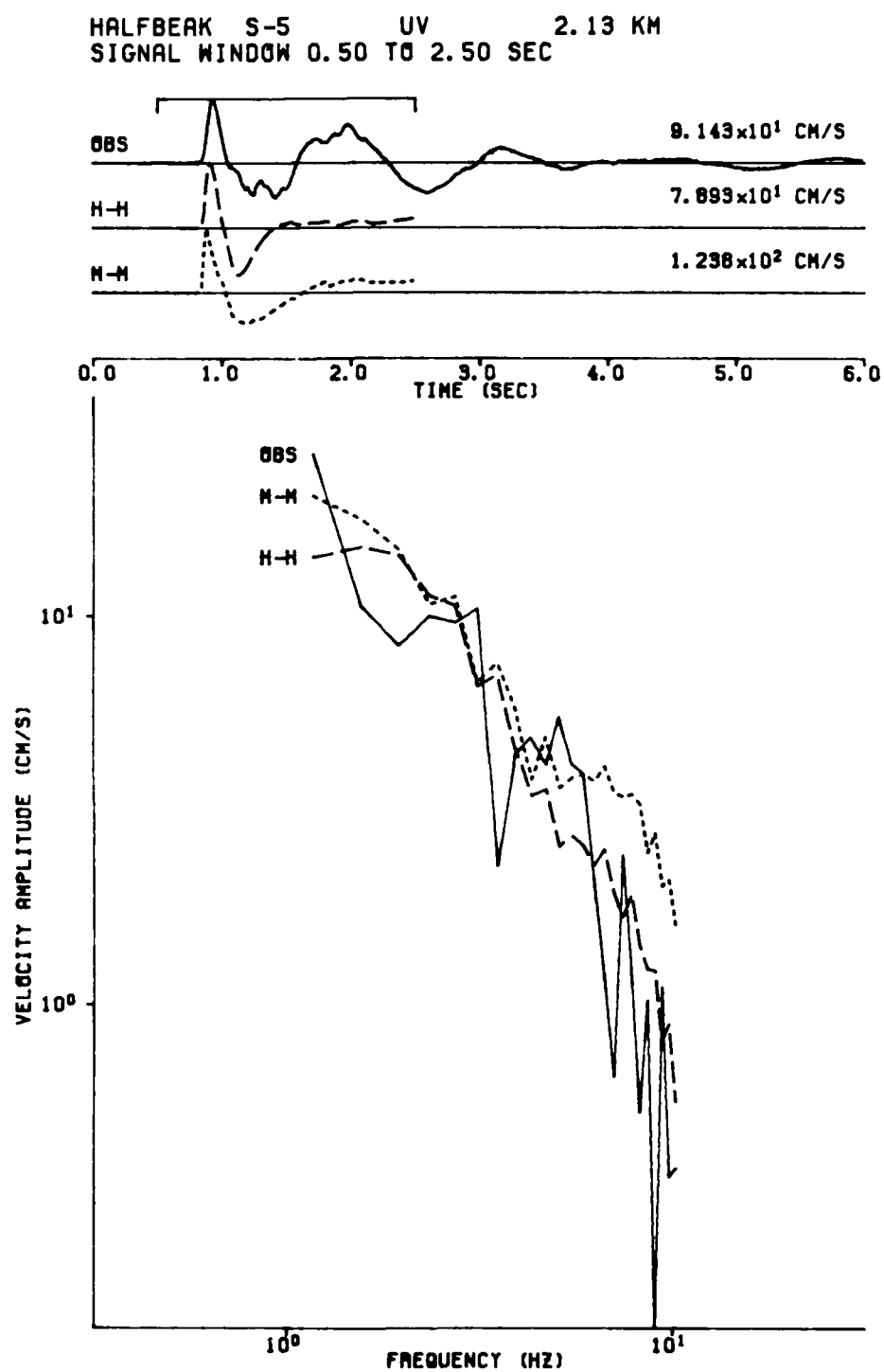


Figure A.21.

HALFBEAK S-7 UV 2.13 KM
SIGNAL WINDOW 0.45 TO 2.45 SEC

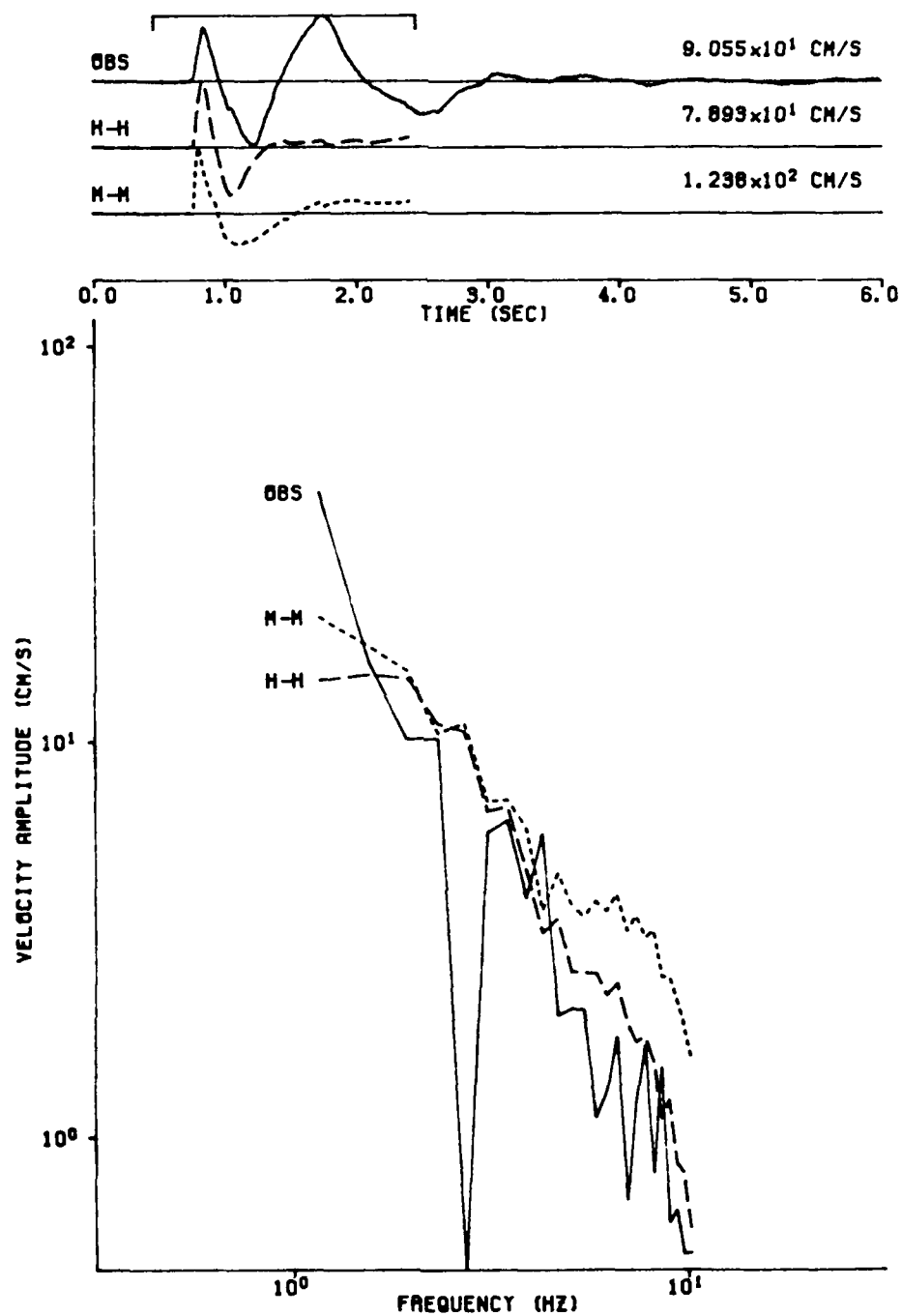


Figure A.22.

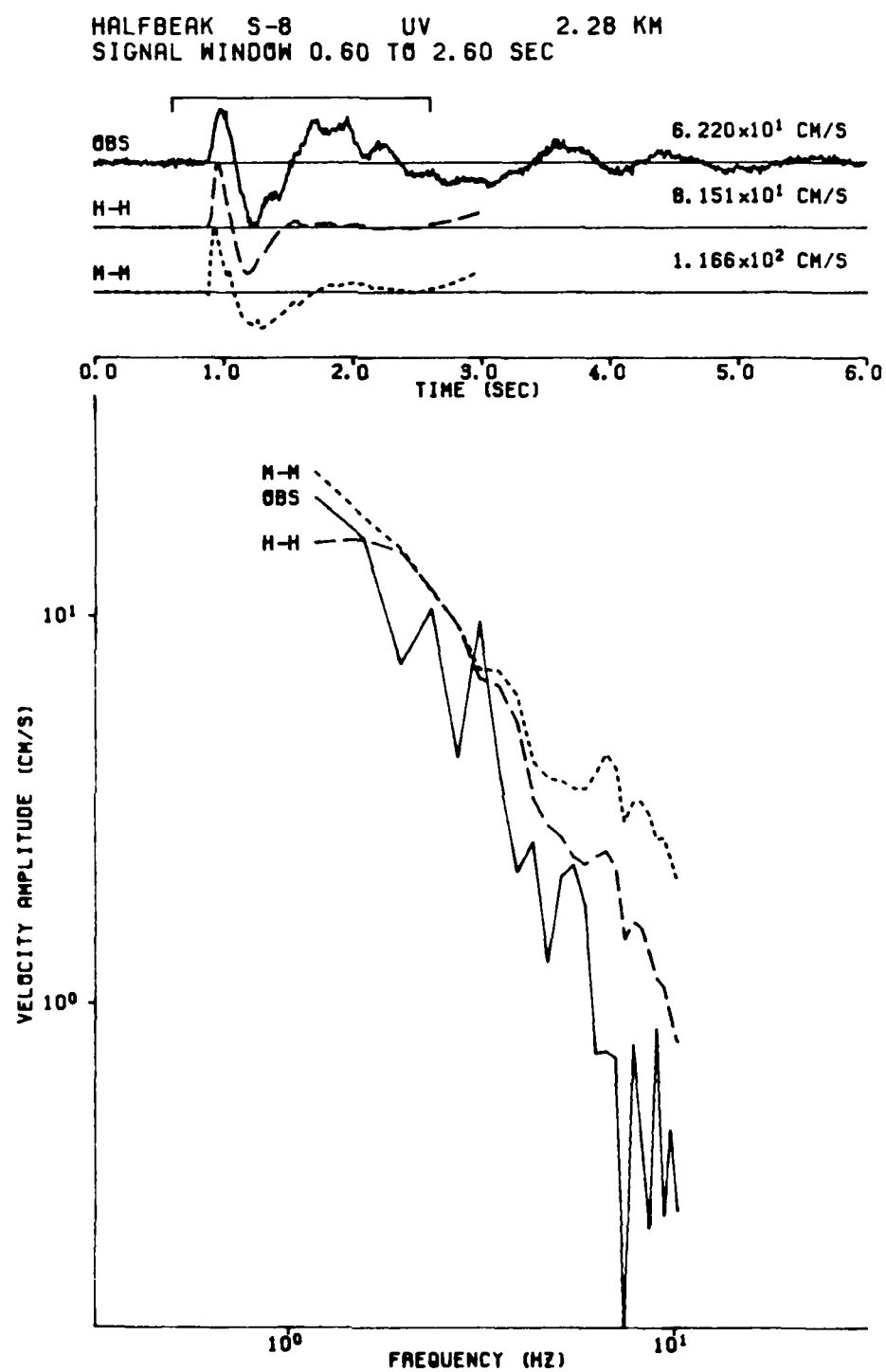


Figure A.23.

HALFBREAK S-6 UV 3.05 KM
SIGNAL WINDOW 0.80 TO 2.80 SEC

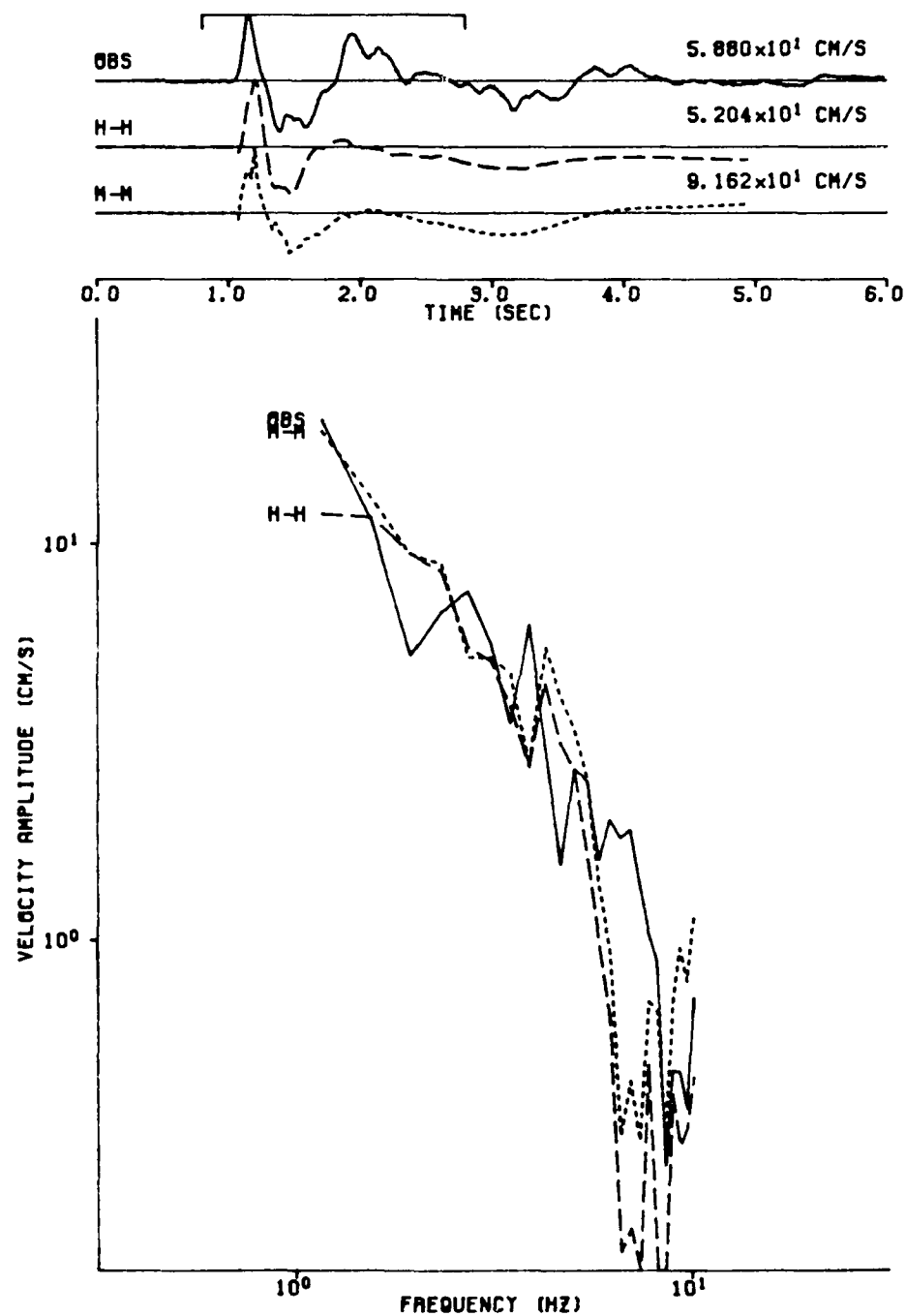


Figure A.24.

PART II

MODELING NEAR-FIELD OBSERVATIONS FROM
NUCLEAR EXPLOSIONS IN DRY TUFF AND ALLUVIUM

by

Terry C. Wallace and Jeffrey S. Barker

INTRODUCTION

The determination of source parameters from any seismic waveform amounts to separating source excitation and propagation phenomena. For underground nuclear explosions, seismic yield determination is usually based on far-field measurements such as short-period P-wave amplitudes. The propagation or path effects are accounted for by correcting for geometric spreading and attenuation. Unfortunately, lateral variations in earth structure (in particular, anelastic attenuation and scattering) can introduce considerable fluctuation in far-field amplitudes. Lay, et al. (1984) have shown that for Pahute Mesa explosions, there is an order of magnitude variation in the corrected amplitude of the first cycle (ab) of short-period P waves with azimuth. This variation in amplitude, which is due to propagation effects, results in uncertainty in the source model.

One way to minimize the variations in path effects is to significantly reduce the path lengths. Helmberger and Hadley (1981), Stump and Johnson (1984) and Burdick, et al. (1984) have shown that it is possible to obtain consistent, detailed explosion source histories from near-field seismograms, especially if there is a priori information about the velocity structure. Near-field records also have the advantage that they allow a high frequency representation of the source and it is possible to separate and account for effects such as spall and slap down.

The major criticism of modeling near-field records concerns the assumption that the material response is linear. In the immediate vicinity of an explosion the rock is vaporized and crushed. The induced stresses are as high as a megabar. The spherical spreading of the stress pulse results in a

reduction of the strain field, and at some distance (the elastic radius), the material will begin to behave like a linear, elastic solid. At distances beyond the elastic radius, elastic theory can be used to recover an effective source function. Seismograms from inside the elastic radius will be grossly inconsistent with predictions based on elastic theory. Failure to recognize the elastic radius results in misinterpretation of the source. The location of the elastic radius is still a subject of considerable controversy (Trulio, 1978; Rodean, 1981; Minster and Day, 1985), and can best be determined by modeling of very well instrumented explosions.

In this section of this report, we model the particle velocity records from surface and borehole gauges for three nuclear explosions (DISCUS THROWER, MUDPACK, and MERLIN) detonated in dry tuff or alluvium. These events are unusual in that they were designed, in part, as experiments to investigate transient wave propagation (Perret, 1971), so considerable care was taken with regard to geologic criteria in their siting. The elastic velocity structure between the source and receivers is known from boreholes and is very nearly planar, with only minimal distortion due to faulting. Since the velocity structure is well determined, it is possible to remove even complicated propagation phenomena such as the interaction between reflected and refracted arrivals. All three events are very well instrumented and allow us to investigate the wavefield over distance ranges from a fraction of the depth of burial to more than ten times that depth. We can see a clear definition of a zone where elastic theory gives consistent estimates of the source. At slant ranges of approximately $130 \text{ m/kt}^{1/3}$ or less, the amplitude of the observed velocity pulse corresponding to the geometric arrival is smaller than expected. The scaled distance of $130 \text{ m/kt}^{1/3}$ corresponds roughly with the

depth of burial, which suggests that elastic waveform modeling can be useful in determining the effective source functions from surface gauges even within the spall zone. Using the announced yields of the three events, we developed a scaling relationship between yield and explosion moment for events in dry tuff and alluvium. The scaling relationship is, in turn, used to estimate the yields of three other Yucca Flats events.

NEAR-FIELD MODELING

The data used in this study are the radial and vertical particle velocity recordings from both surface and borehole gauges for the events DISCUS THROWER, MUDPACK and MERLIN. All three of these events are in the northeastern part of NTS (see Figure 1 and Table 1) and were detonated in dry tuff or alluvium, which has a P-wave velocity of approximately 2.1 km/s. The portions of the seismograms that are modeled are those containing the body wave arrivals. Figure 2 shows a typical data array: the surface recordings from DISCUS THROWER. At the largest distance range (1340 m), the fundamental mode of the Rayleigh wave arrives 0.8 seconds after the first arrival. At the closest ranges (15 and 122 m), the direct P waves are marked by an inflection in the velocity pulse (the maximum amplitude of the P waves is denoted by an arrow in Figure 2). The total record modeled at these ranges is only 0.2 seconds.

The arrival of the body waves is much clearer on the acceleration data. As an example, Figure 3 shows a comparison of the velocity and acceleration records for the event MUDPACK. For the closest station (45.7 m), an

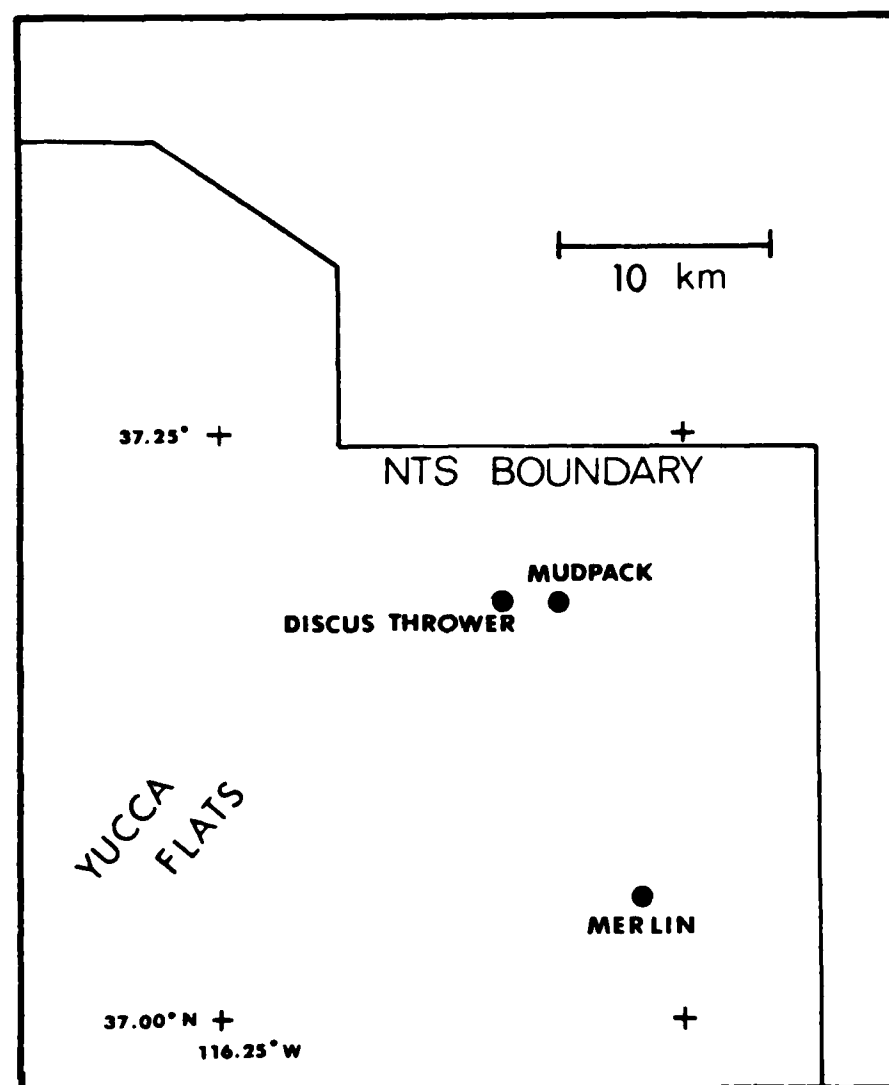


Figure 1. Location of the three events studied in this section of this report: MERLIN (2/16/65), MUDPACK (12/16/64) and DISCUS THROWER (5/27/66).

Table 1 - Event Parameters

<u>Event</u>	<u>Date</u>	<u>Time</u> <u>(GMT)</u>	<u>Lat.</u> <u>(°N)</u>	<u>Lon.</u> <u>(°W)</u>	<u>Depth</u> <u>(m)</u>	<u>Ann. Yield</u> <u>(kt)</u>
DISCUS THROWER	5/27/66	20:00	37.178	116.098	337	21
MUDPACK	12/16/64	20:10	37.178	116.067	155	2.7
MERLIN	2/16/65	17.30	37.052	116.024	296	10

inflection in the broad velocity pulse (with an amplitude of approximately 2 ft/sec) represents the arrival of the direct P wave. This arrival actually represents a peak in the acceleration data. The cause of the shoulder on the peak in acceleration data is not known, although it may be related to spall opening, or to a non-elastic wavefield due to the shockfront from the explosion. At larger ranges, the shoulder disappears. At the farthest station in Figure 3 there is no shoulder; both downgoing and upgoing energy are present. In this study, we model the rise time and amplitude of velocity records. The acceleration records are used to confirm the peak of the body-wave arrival. It is obvious from Figure 3 that studies using only peak velocity measurements will differ significantly from our modeling procedure at small ranges. We prefer to isolate identifiable arrivals and see how well elastic wave propagation theory can predict the observations.

The method we use to calculate the P-wave amplitude is generalized ray theory and the Cagniard-deHoop technique (see Helmberger, 1968; Langston and Helmberger, 1975; Burdick, et al., 1984). It is assumed that the explosion can be represented as a point source and that the geologic structure can be

$$\Psi(t) = \Psi_{\infty} \left\{ 1 - e^{-kt} \left\{ 1 + kt + \frac{1}{2}(kt)^2 + \frac{1}{6}(kt)^3 - B(kt)^4 \right\} \right\} \quad (2)$$

where Ψ_{∞} represents the static value of the RDP with dimensions of volume, k is the inverse of the rise time of the source function, and B is a measure of the overshoot. vonSeggern and Blandford (1972) modified Haskell's source representation by truncating it to a quadratic, based on the observed f^{-2} spectral decay of teleseismic, short-period body waves. We have chosen to use a representation of the source introduced by Helmberger and Hadley (1981):

$$\Psi(t) = \Psi_{\infty} \left\{ 1 - e^{-kt} \left\{ 1 + kt + \frac{1}{2}(kt)^2 - B(kt)^3 \right\} \right\} \quad (3)$$

The parameters have the same meaning as in Haskell's model, although, except for Ψ_{∞} which is identical for any of the source representations discussed, the values of rise time and overshoot will vary between models. Section I of this report provides justification for our use of (3) rather than a f^{-2} model: both are consistent with the data within the near-field frequency band (2 - 5 Hz) as long as the latter is used in conjunction with a depth-dependent crustal attenuation model. For lack of sufficient a priori information on crustal attenuation at Yucca Flats, we have chosen to use (3) as the simpler model.

There are three parameters that must be modeled in (3): Ψ_{∞} , k and B . As discussed by Burdick, et al. (1982) and Hartzell, et al. (1983), it is not possible to resolve B from local strong-motion data because the short duration precludes sufficient long-period energy. At the frequencies of interest, B trades off directly with Ψ_{∞} . Since the main conclusions we reach in this

study do not depend on knowing the absolute value of the $B-\psi_{\infty}$ pair, we assume a value for $B = 1$. Since the scaling relations which we use were derived with this constraint, the errors in the assumption of B will not adversely affect yield estimates. Lay, et al. (1984) showed that the amount of overshoot in the RDP decreases with yield (and hence with increasing depth of burial) for the Amchitka test site. Using the Lay, et al. (1984) scaling law gives a value of about 2.0 for B for the events modeled in this study. If one prefers the higher value for B , then ψ_{∞} scales down accordingly.

The rise time parameter, k , controls the corner frequency. For the smallest event studied (MUDPACK), the corner frequency is higher than the data frequency, and it is impossible to resolve k . Hartzell, et al. (1983) developed scaling laws for k and B from strong-motion data from several Pahute Mesa events:

$$k = 4.04 h^{\frac{1}{2.4}} / Y^{\frac{1}{3}} \quad (4)$$

where h is the depth of burial in meters and Y is the yield in kilotons. We used (5) to determine k for MERLIN and DISCUS THROWER, found that the agreement with observationally determined values was very consistent, so we used (5) to calculate k for MUDPACK.

The static value of the RDP was determined by comparing the observed amplitude with the synthetic responses. The consistency of ψ_{∞} determined from the different data is a measure of the ability of linear theory to predict the amplitude. Theoretically, the RDP must satisfy the condition that it is invariant with distance. Therefore, assuming the propagation effects are

modeled correctly, any systematic variation in ψ_{∞} with distance will reflect non-linear or non-symmetric behavior.

THE DATA

DISCUS THROWER: The DISCUS THROWER experiment was detonated May 27, 1966 at 20:00:00.0 GMT. The working point was at a depth of 337 m in dry tuff (above the water table). Figure 4 shows a geologic cross-section along the line of boreholes. There are three basic units in the geologic section: (1) dry desert alluvium with an average thickness of about 170 m, (2) a bedded ashflow tuff, and (3) a sequence of Paleozoic carbonate rocks. Also shown in Figure 4 are the locations of various recording instruments. The length of the array is 1.3 km, and the maximum surface relief is approximately 20 m. Except for a minor fault with a total offset of only about 21 m, there is no major deviation from planar interfaces along the contact between units. DISCUS THROWER was detonated only 30 m from the carbonate-tuff interface.

All of the available borehole and surface gauge data were modeled for rise time and ψ_{∞} . Table 2 gives the velocity structure used in calculating the Green's functions for the synthetics. The P-wave velocities and densities are taken from Perret and Kimball (1971). The S-wave velocities are arbitrarily set, with the exception of the alluvium layer, which is adjusted so that the velocity model accurately predicts the travel time of the Rayleigh wave to station 12S. Minor adjustments were required in the layer thicknesses as compared to that observed from the borehole cuttings. For example, we have adjusted the tuff-carbonate interface to be 90 m below the working point.

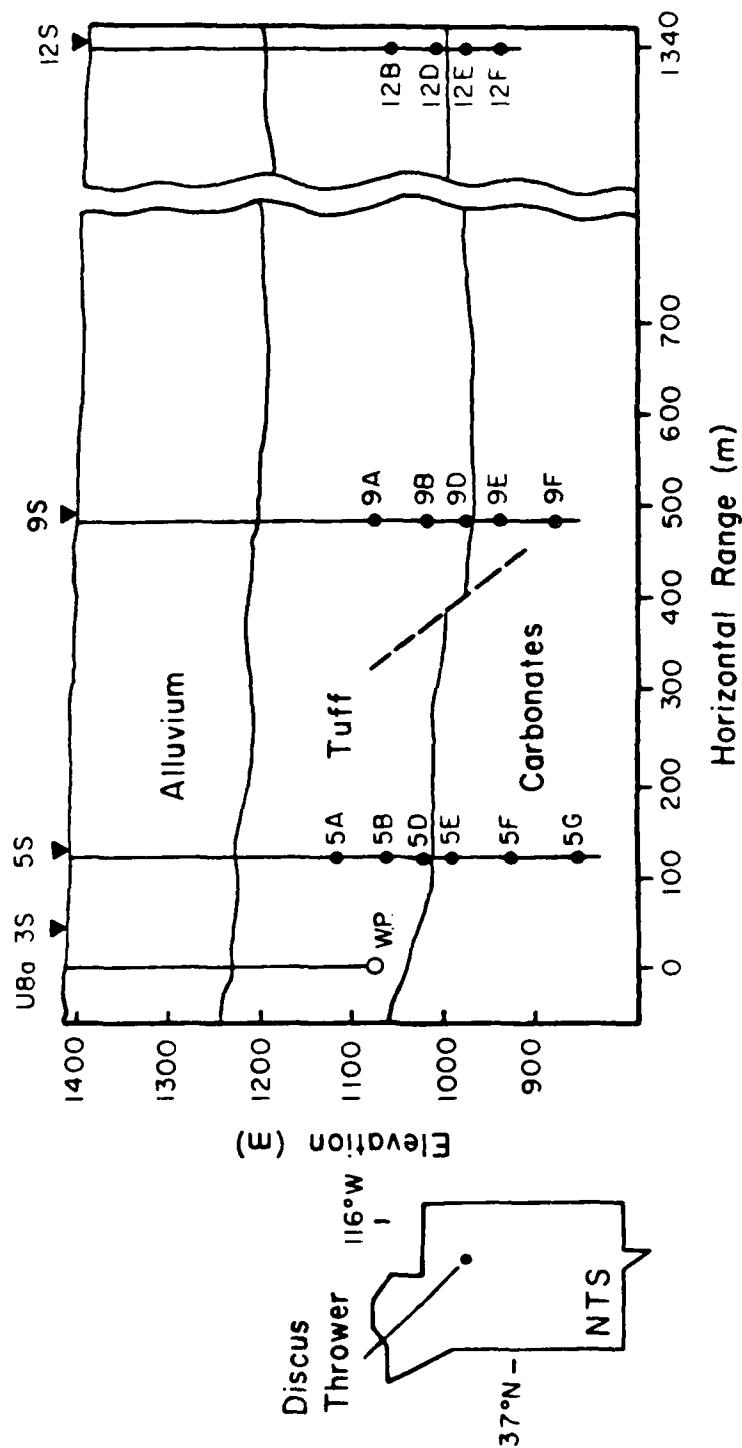


Figure 4. Surface and borehole station locations for DISCUS THROWER. The tuff-carbonate interface marks a major acoustic impedance contrast.

Table 2 - Velocity Structure for DISCUS THROWER and MUDPACK

Medium	V_p (km/s)	V_s (km/s)	Density (g/cm^3)	Thickness (m)
Alluvium	1.7	0.9	1.6	168
Tuff	2.1	1.3	1.9	258
Carbonate	5.2	2.8	2.7	halfspace

This is largely the result of the gentle dip of the interface along the profile. The synthetic modeling of the 12S waveforms, as discussed below, requires the greater tuff thickness. Since stations such as 9D and 12E are very close to the interface, their depths were adjusted on the basis of their distance from the interface. As expected, the velocity model does an excellent job of predicting the travel time to all stations.

The proximity of the working point to an interface with such a large acoustic impedance contrast makes the modeling difficult. Three basic rays influence the P waveforms: (1) the direct arrival, (2) an arrival that is reflected at the interface, and (3) an arrival that is refracted along the interface. As an example of the importance of these three arrivals, Figure 5 shows the vertical and radial observations at station 12S and the fit of the synthetic waveforms decomposed into these three rays. The peculiar shape of the radial waveform is diagnostic. The small first arrival is identified as the head wave. The direct and reflected arrivals must interfere in such a way as to give not two distinct pulses, but rather the single large second arrival. It is this modeling result that required the adjustment to the tuff

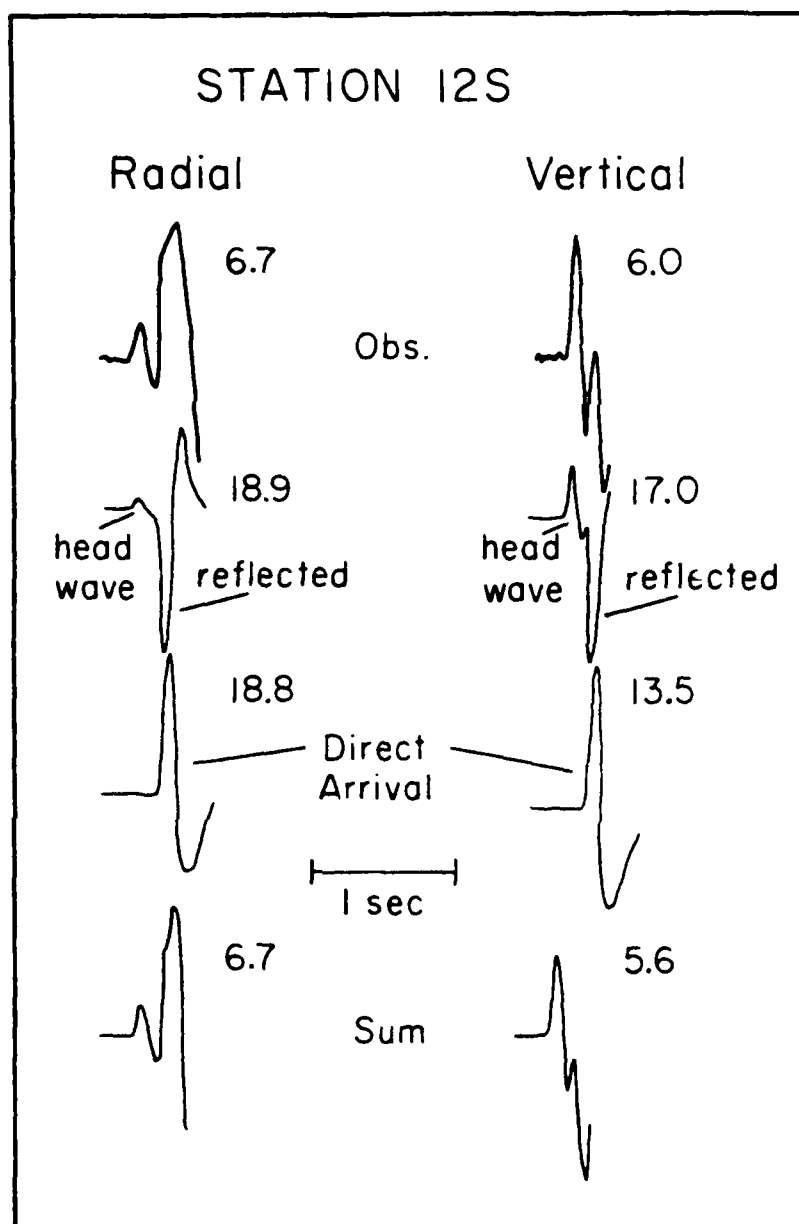


Figure 5. Modeling of surface station 12S for DISCUS THROWER. The observed records can be modeled as the sum of three rays: (1) the direct arrival, (2) the reflection from the tuff-carbonate interface and (3) the head wave along that interface. The working point is so close to the interface that direct and reflected arrivals interfere.

layer thickness. The interaction between reflected and refracted arrivals can be seen in the borehole data at station 12D (Figure 6). At this distance, the station is just beyond the crossover distance at which the refracted wave becomes the first arrival. This interference can be seen by the double peak in the first swing on the radial component.

The best average value for the inverse rise time parameter, k , for the DISCUS THROWER data was determined to be 16 sec^{-1} . Table 3 gives the values of Ψ_{∞} for the surface recordings. The average value is $1.22 \times 10^9 \text{ cm}^3$ with a standard deviation of $0.32 \times 10^9 \text{ cm}^3$. Ψ_{∞} from the closest station, 3S, which is only 15 m from the device borehole, appears to be inconsistent with the other values. The average from the three farther stations is $1.37 \times 10^9 \text{ cm}^3$ with a standard deviation of $0.16 \times 10^9 \text{ cm}^3$.

There is considerably more uncertainty in modeling borehole gauges than those at the free surface. Typically, these waveforms have phases or arrivals that are difficult to explain; also, many of the gauges are located near the large velocity contrast. For this reason, static RDP values from the borehole instruments were determined separately from those of the surface data and compared. Table 4 gives Ψ_{∞} for 9 different subsurface stations. There is a substantial difference between the values determined from the vertical component and those determined from the radial component. The average value of Ψ_{∞} determined from the verticals is $1.09 \times 10^9 \text{ cm}^3$ with a standard deviation of $0.17 \times 10^9 \text{ cm}^3$. This value is in fair agreement with that from the surface recordings. The average value of Ψ_{∞} determined from the subsurface radial components is $0.78 \times 10^9 \text{ cm}^3$ with a standard deviation of $0.52 \times 10^9 \text{ cm}^3$. For a given borehole, the values from the radial components below or above the interface are consistent, but they are not consistent

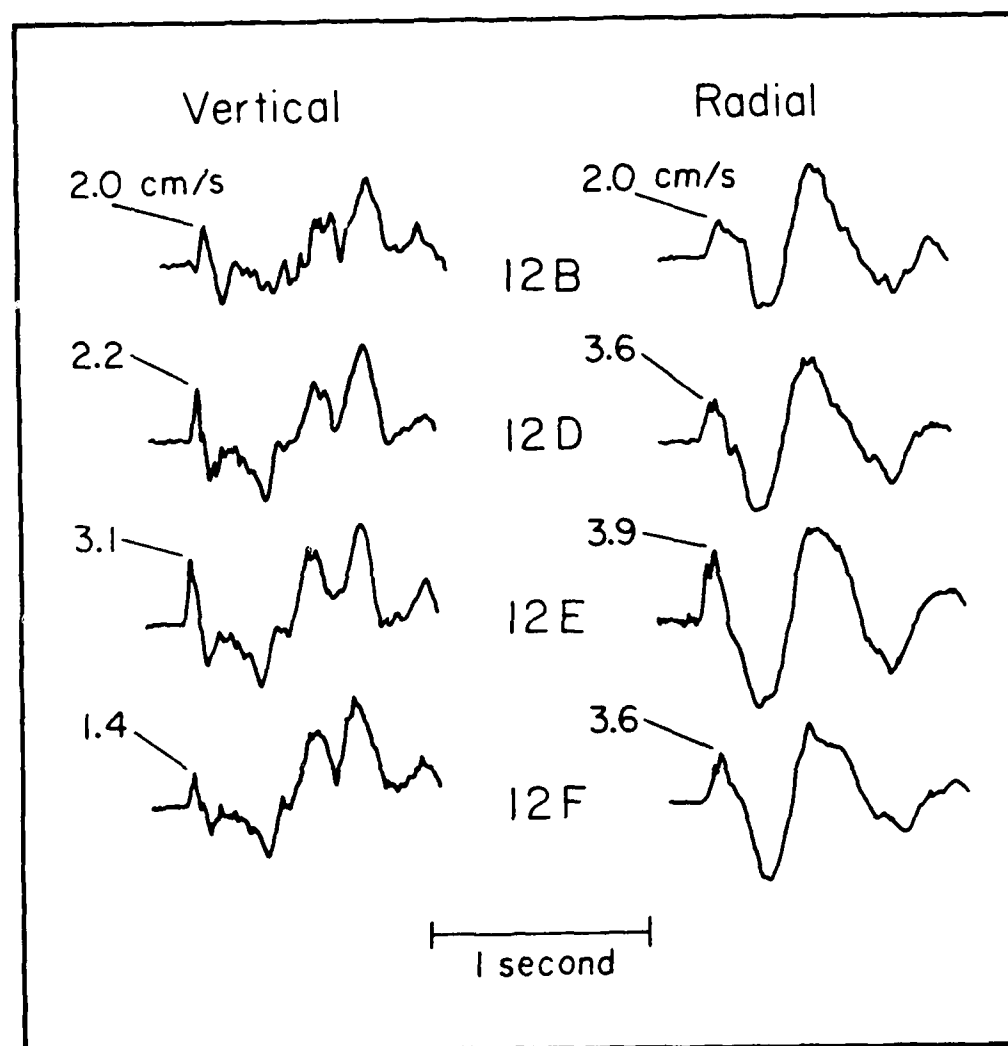


Figure 6. Vertical and radial borehole seismograms from site 12 for DISCUS THROWER. The tuff-carbonate interface is located at a depth between gages 12D and 12E.

Table 3 - Static RDP values for surface recordings
from DISCUS THROWER

<u>Station</u>	<u>Vertical (cm³)</u>	<u>Radial (cm³)</u>
3S	0.83 x 10 ⁹	0.68 x 10 ⁹
5S	1.40 "	1.41 "
9S	1.33 "	1.22 "
12S	1.66 "	1.21 "

across the interface. The vertical components of the velocity do not appear as sensitive to the interface.

Figure 7 compares the predicted and observed amplitudes of the initial P wave as a function of slant range. The value of ψ_{∞} used is an average from both surface and subsurface values. The predictions are quite good, even though the amplitudes change by a factor of 30 and the distance varies by a factor of 10.

MUDPACK: The MUDPACK experiment was detonated on December 16, 1964 at 20:10:00.0 GMT. The working point was at a depth of 155 m and was very close to that of DISCUS THROWER. It was assumed that the velocity structures of the two events were identical. As with DISCUS THROWER, the event was well instrumented, with borehole gauges both above and below the carbonate interface.

Table 5 gives the values of ψ_{∞} determined by modeling the P waves. The announced yield of MUDPACK was only 2.7 kt, so the rise time could be modeled

Table 4 - Static RDP values for subsurface recordings
from DISCUS THROWER

<u>Station</u>	<u>Vertical (cm³)</u>	<u>Radial (cm³)</u>
9A	1.18 x 10 ⁹	1.71 x 10 ⁹
9B	1.20 "	1.31 "
9D	1.01 "	0.39 "
9E	0.98 "	0.38 "
9F	0.90 "	0.21 "
12B	1.09 "	0.39 "
12D	1.43 "	0.55 "
12E	1.11 "	1.16 "
12F	0.89 "	0.95 "

with any value of the k parameter greater than 20. For this reason, we assumed the scaling relation of Hartzell, et al. (1983) and calculated a k value of 23 sec⁻¹. As with DISCUS THROWER, the values of Ψ_{∞} determined from the vertical component of the velocity record are very consistent and appear to be independent of gauge location, with the exception of the very closest ranges (e.g., station N1).

The average value determined for Ψ_{∞} from the surface gauges is 9.9×10^7 cm³. The borehole average is somewhat smaller (9.2×10^7 cm³) but is consistent when the closest stations are eliminated from the average. The radial gauges show significantly more scatter. The average value is 7.1×10^7 cm³, but if station N1 is eliminated the average becomes 8.6×10^7 cm³.

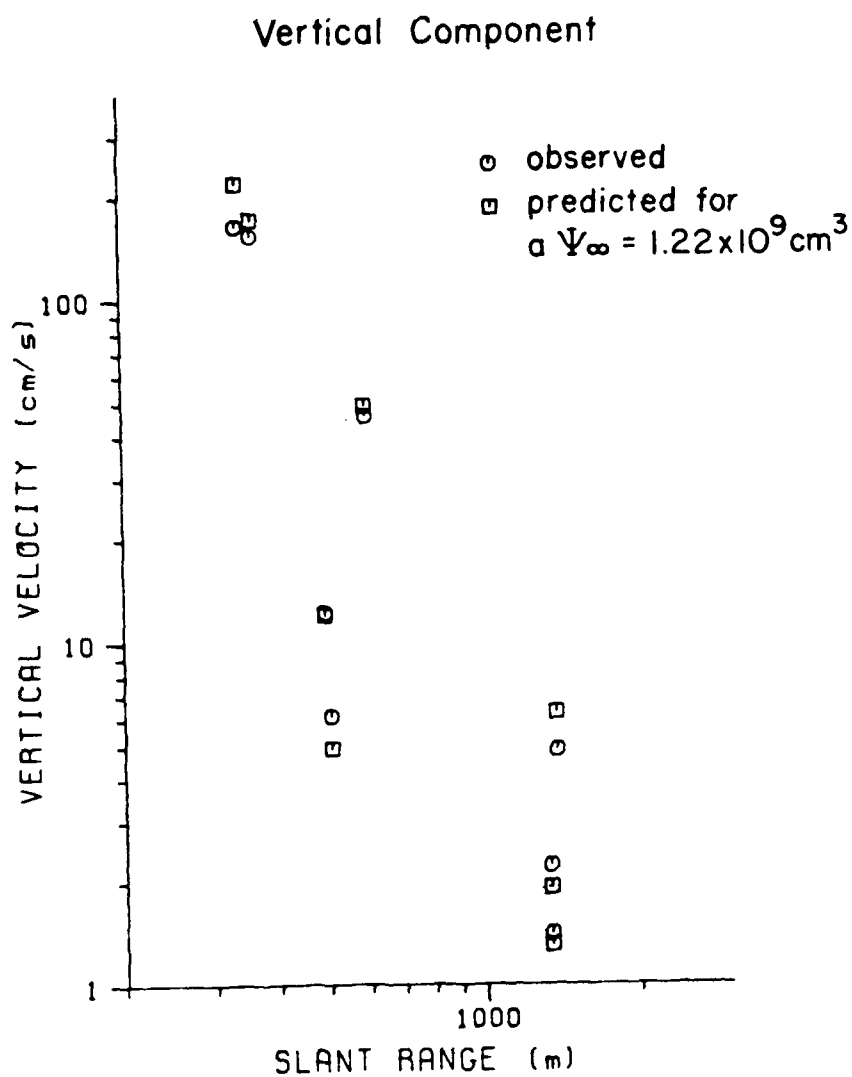


Figure 7. A comparison of the observed and predicted amplitude of the vertical component of velocity for DISCUS THROWER. Both surface and borehole gages are included.

Table 5 - Static RDP values from MUDPACK

<u>Surface Gages</u>	<u>Slant Range (m)</u>	<u>Vertical (cm³)</u>	
1	162	0.89 x 10 ⁸	
2	180	0.83	"
3	228	0.97	"
4	302	1.20	"

<u>Borehole Gages</u>	<u>Slant Range (m)</u>	<u>Vertical (cm³)</u>	<u>Radial (cm³)</u>
B4-4	303		0.68 x 10 ⁸
B4-3	195	0.96 x 10 ⁸	0.89 "
B4-2	179	0.67 "	0.85 "
B4-1	173	0.65 "	0.89 "
B2-3	279	0.78 "	0.99 "
B2-1	261	1.26 "	1.12 "
N1-4	183		0.39 "
N1-3	131	0.17 "	0.27 "
N1-1	102	0.48 "	0.51 "

MERLIN: The MERLIN experiment was detonated on February 16, 1965 at 17:30:00.0 GMT. The working point was at a depth of 296 m in dry tuff, and was south of DISCUS THROWER and MUDPACK, but the borehole cuttings indicate that the geology is very similar. MERLIN was instrumented with two borehole arrays, but these were located very close to ground zero, so only the surface array data was used to determine Ψ_{∞} .

Table 6 gives the values of Ψ_{∞} determined for MERLIN. At slant ranges less than 300 m, the values for Ψ_{∞} appear to be underpredicted. Beyond 300 m, the average value for Ψ_{∞} is $3.4 \times 10^8 \text{ cm}^3$. The radial surface velocity gauges are again inconsistent with both the vertical measurements and with each other.

DISCUSSION

For all three of the events studied, the near-field records provided a consistent measure of the effective source function once a critical distance is reached. Inside this critical distance, the values we determine for Ψ_{∞} are systematically underestimated. Figure 8 is an attempt to compare all three events. For each station for a given explosion, the value of Ψ_{∞} determined at that station is divided by the average for the event. This is plotted as a function of scaled distance to remove the effect of different yields. Beyond a distance of approximately 130 scaled meters, the values of normalized Ψ_{∞} scatter about 1.0 by $\pm 20\%$. At distances less than $130 \text{ m/kt}^{1/3}$, the stations' values of the static RDP is progressively less than the large distance mean. We interpret this as the breakdown in elastic wave propagation theory in predicting the ground velocity very near an explosion. On the basis of non-linearity or shockwave fronts, the underprediction of Ψ_{∞} is counter-intuitive: inside the elastic radius we expect the velocity amplitudes to be much greater than predicted. This is most likely an artifact of the way we are measuring the peak velocity. It is in this region that the acceleration pulses have pronounced shoulders, so the energy in the pulse appears to be partitioned into at least two wavefields, only one of which is behaving elastically. If we look only at the peak velocity and not try to identify the geometric arrival, the values of Ψ_{∞} tend to be overpredicted. Although we do not have a model for the acceleration pulse shoulder, its presence can be used to determine where elastic waveform modeling may be used

Table 6 - Static RDP values from MERLIN

<u>Slant Range (m)</u>	<u>Vertical (cm³)</u>	<u>Radial (cm³)</u>
297	2.03 x 10 ⁸	
300	2.21 "	
305	2.87 "	
315	2.98 "	
332	2.93 "	
425	3.30 "	1.55 x 10 ⁸
544	4.30 "	1.79 "
678	3.57 "	0.70 "
816	3.37 "	0.78 "

to determine the effective source function. Figure 9 indicates that a similar phenomenon occurs for near-field data from Pahute Mesa. When a similar measurement approach is applied to data from ten Pahute Mesa events studied by Barker, et al. (1985) and Hartzell, et al. (1983), the observed peak velocities are well predicted beyond a scaled range of about $175 \text{ m/kt}^{1/3}$, but are overpredicted inside this range. The difference in the range at which elasticity appears applicable between Yucca and Pahute events is presumably due to differences in material properties between sites.

Once the zone of "elastic applicability" has been determined, and assuming structure is well known, the estimates for yield based on Ψ_{∞} will not be a function of gauge location. The determination of the values of Ψ_{∞} in this study are of particular interest because they represent energy radiated over a large range of take-off angles. For example, in the case of DISCUS THROWER, the value of Ψ_{∞} determined from station 12S is most sensitive to energy radiated downward along a take-off angle of 25° , while the borehole

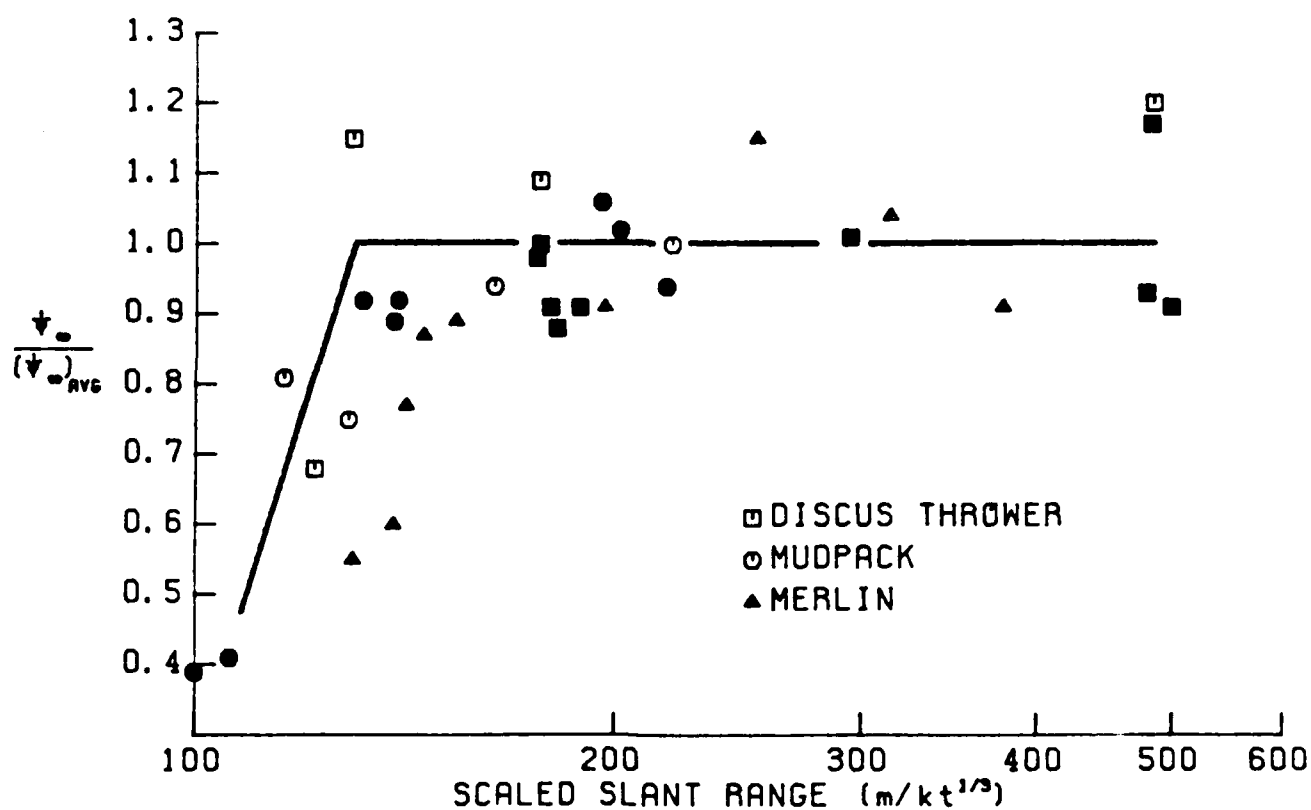


Figure 8. A comparison of the normalized Ψ_{∞} (Ψ_{∞} as determined at a given station divided by the average value for that event) for the three events studied. Beyond a scaled distance of about 130 m/kt^{1/3}, the modeling provides a very consistent measure of Ψ_{∞} .

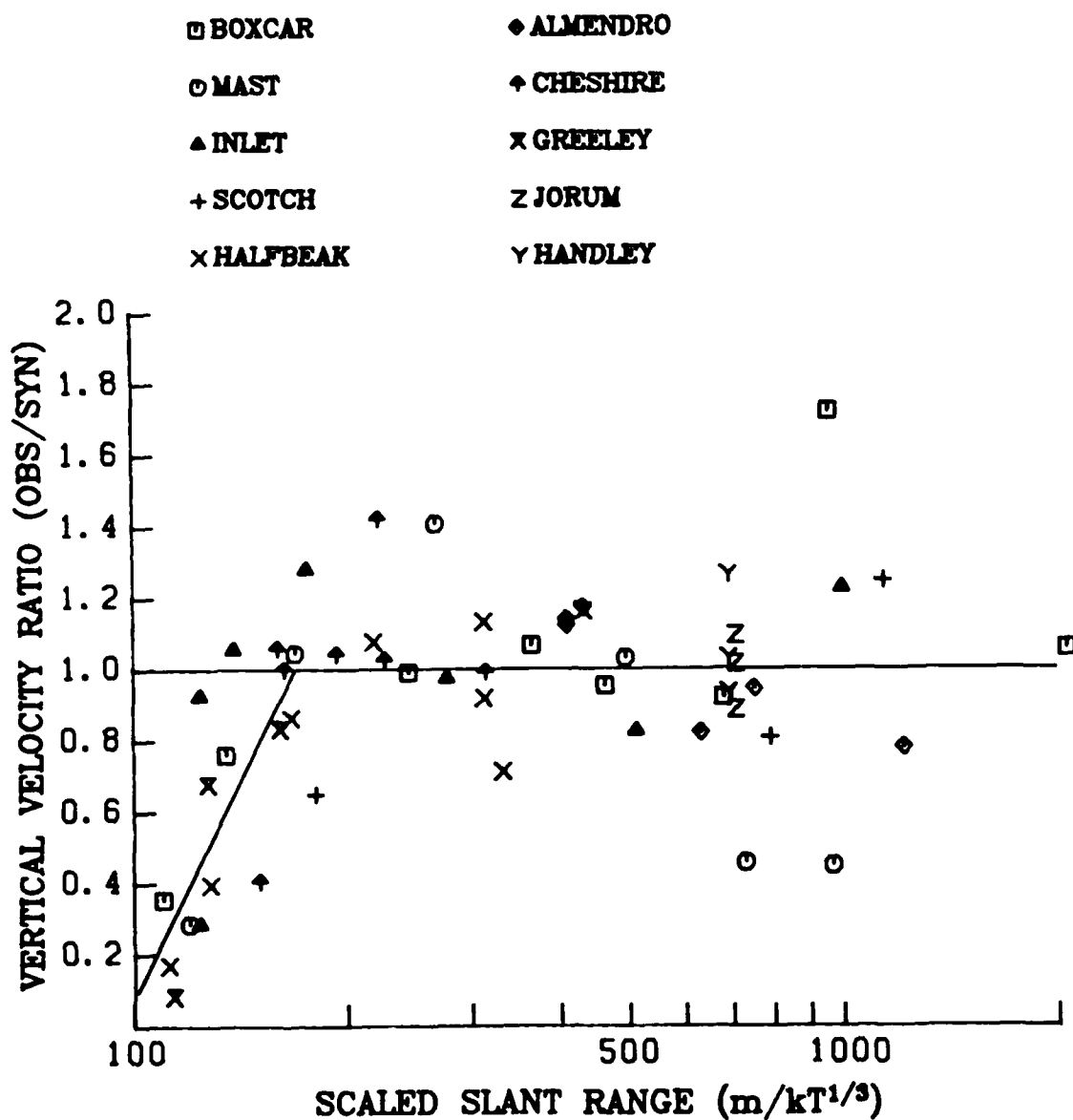


Figure 9. A comparison of the ratio of observed to synthetic peak velocity values for ten Pahute Mesa events modeled by Barker, et al. (1985) and Hartzell, et al. (1983). This measure is equivalent to the normalized ψ_{∞} of Figure 8. For Pahute Mesa events, consistent amplitudes are obtained beyond a scaled range of about $175 m/kt^{1/3}$.

stations have a horizontal angle of incidence, and station 5S has a nearly vertical (up) travel path. If the explosion was not symmetric, one would expect to see variations in the estimate for Ψ_{∞} . The large data set here argues against a source asymmetry explanation for tectonic release.

For all three events, the radial P-wave amplitudes are much more difficult to predict than their vertical component counterparts. At large ranges, the surface radial values for Ψ_{∞} are in good agreement with the vertical estimates, but at the borehole stations, they are generally smaller than expected, and are very sensitive to the location of the gauge relative to the tuff-carbonate interface. There are three basic hypotheses to explain the inconsistencies: (1) the horizontal motions are more influenced by incorrectly modeled structural parameters than the vertical motions, (2) the horizontal motions are more influenced by non-linear behavior, or (3) somehow the radial motion is more difficult to measure (i.e., poor coupling in the borehole) than the vertical motion. It is beyond the scope of this study to differentiate between these possibilities, the variation in radial amplitudes is important in light of other techniques for calculating the static level of the RDP. One of the most common techniques is to integrate the radial displacement as recorded at a borehole gauge at approximately shot level. Perret and Kimball (1971) determined Ψ_{∞} using this technique for several of the borehole stations we modeled in this study for DISCUS THROWER. The value they obtain for the RDP is $4.2 \times 10^9 \text{ cm}^3$, or a factor of 4 larger than our result. Figure 10 includes a comparison of the scatter for the two methods of determining Ψ_{∞} . The integration of the radial displacement has scatter of a factor of 5.0 about the mean, while using the elastic modeling of the vertical component of the P waves has a scatter of 0.2.

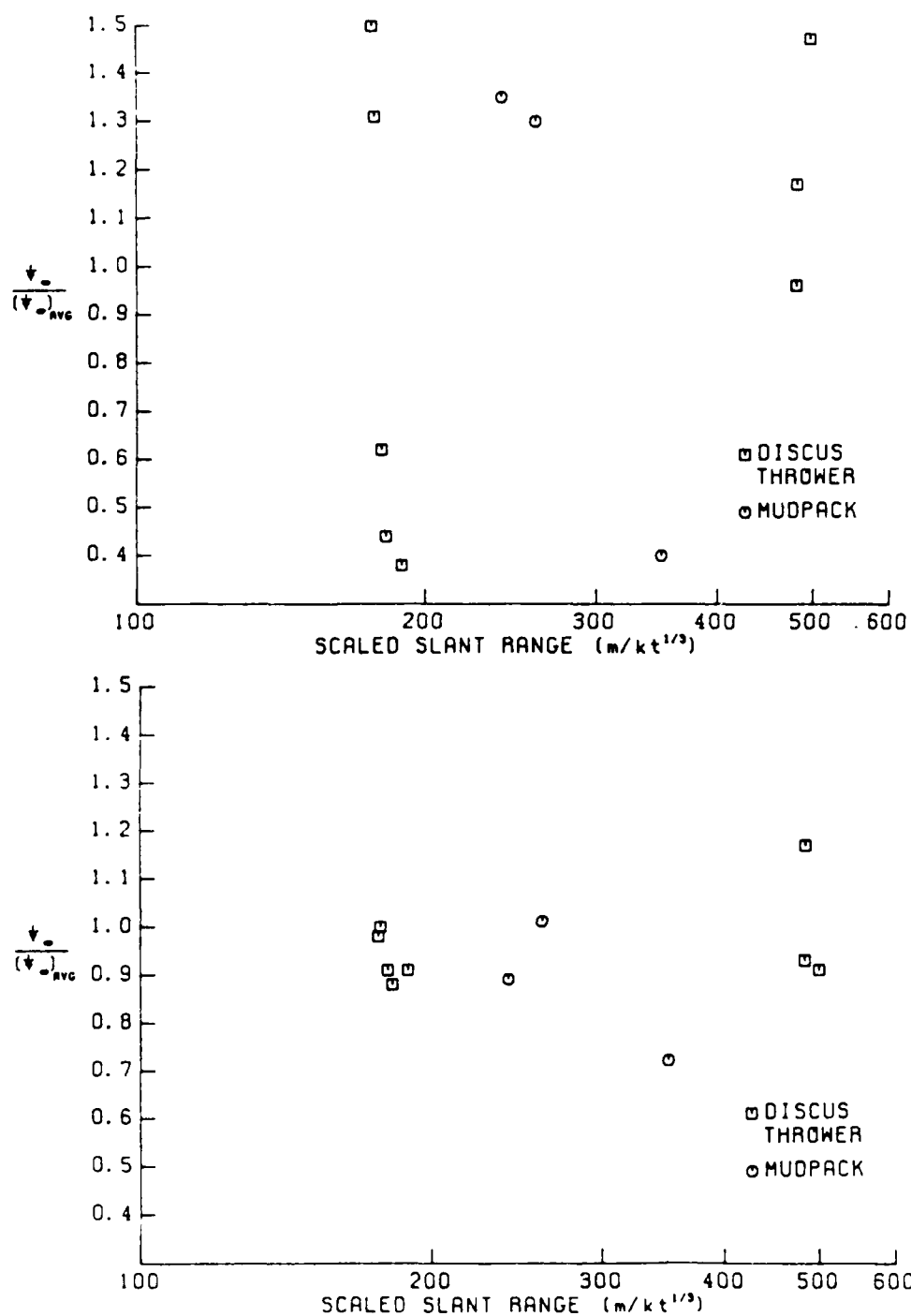


Figure 10. A comparison of methods for determining ψ . The top graph shows the scatter in ψ_{∞} as determined by integration of the radial components of displacement near shot level. The lower graph gives the scatter in ψ_{∞} determined by generalized ray modeling.

In order to estimate the yields of underground explosions based on the effective source functions as determined by near-field modeling, we must have a series of scaling relationships that are applicable to the material properties of the source medium. Hartzell, et al. (1983) developed the following scaling relation for Pahute Mesa events:

$$\Psi_{\infty} = 6.72 \times 10^8 Y / h^{0.27} \quad (5)$$

where h is the depth of burial in meters. Further, on the basis of announced yields, it is possible to write an empirical relationship for h and yield:

$$h = 0.120 Y^{1/3}. \quad (6)$$

Combining (5) and (6) leads to

$$\Psi_{\infty} = 9.6 \times 10^7 Y^{1.1}. \quad (7)$$

We have chosen to approximate this with a simple linear relationship between yield and Ψ_{∞} :

$$\Psi_{\infty} = 10.2 \times 10^7 Y. \quad (8)$$

We can derive the same sort of function for the Yucca Flats data modeled in this study using the announced yields. This gives

$$\Psi_{\infty} = 4.0 \times 10^7 Y. \quad (9)$$

This implies that the coupling associated with the dry tuff of alluvium is 2.5 times less than that of the wet tuff of Pahute Mesa. This is consistent with the analysis of Perret and Kimball (1971), who found that DISCUS THROWER had a very low seismic efficiency; only 0.25% of the energy released in the explosion reaches the region of elastic response as seismic energy. In contrast, explosions detonated in hard rock typically have an efficiency of about one percent.

We can use (9) to predict the yields of other events detonated in dry tuff or alluvium. Perret and Bass (1975) summarize the peak velocity measurements for several Yucca Flats events. We took the velocity amplitudes and station parameters, along with the velocity model used for DISCUS THROWER and determined values of Ψ_{∞} for PACKARD, FISHER and VULCAN. In Figure 11 the values of Ψ_{∞} are plotted against announced yield for these events. In all three cases, the scaling relationship did a very good job of predicting the yield. In fact, the worst event predicted is DISCUS THROWER, which appears to fall between the curves for wet and dry tuff. This may be the result of DISCUS THROWER being detonated so close to the carbonate interface.

CONCLUSIONS

It is possible to use the rise time and amplitude of the near-field P waves to determine consistent static levels of Ψ_{∞} for an effective source function described by Helmberger and Hadley (1981). For the three events studied (Table 7 summarizes the effective source functions obtained), the

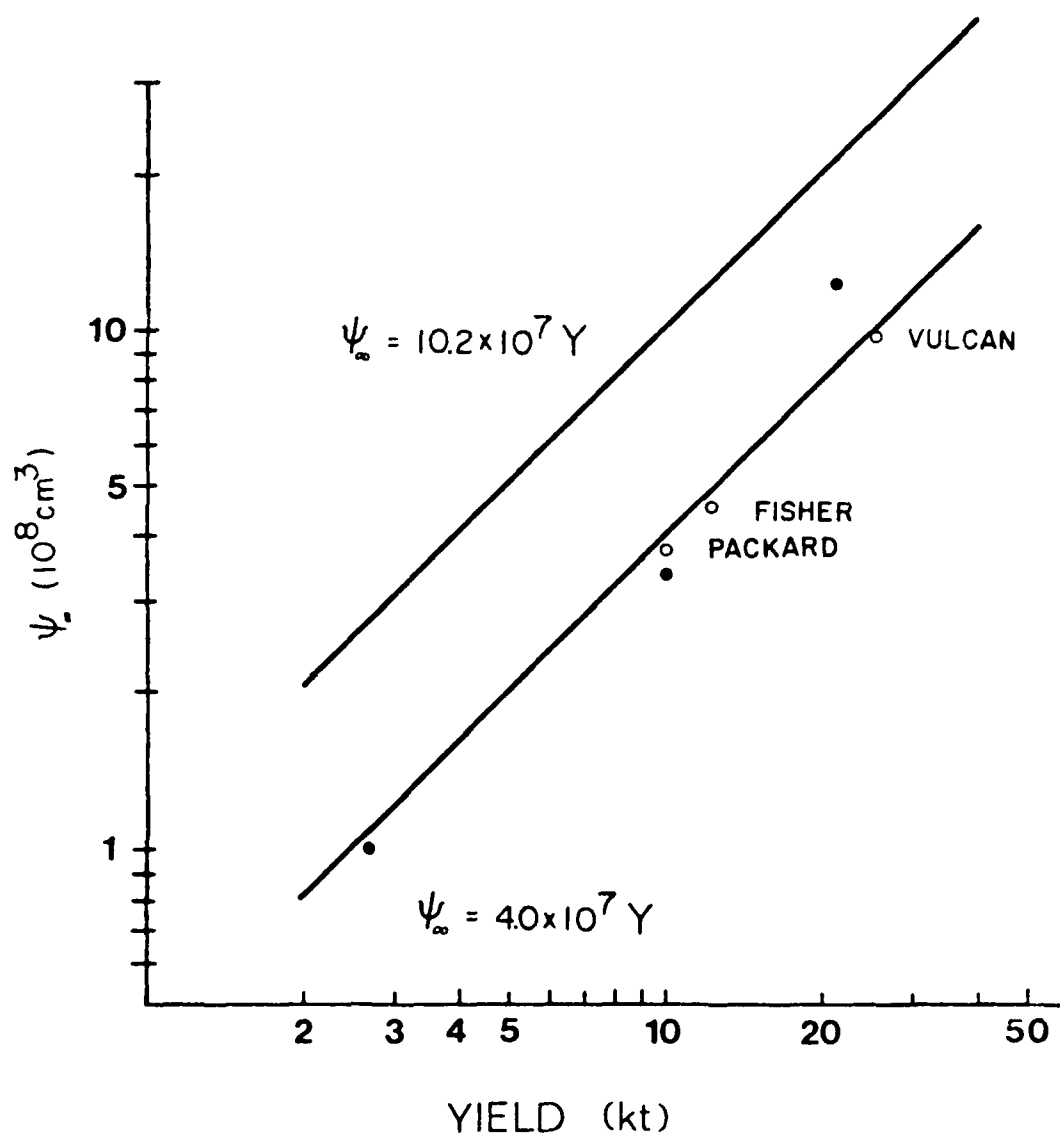


Figure 11. A linearized scaling law relating ψ_{∞} to yield for events detonated in dry tuff or alluvium. Also shown is an approximation to the relation developed by Hartzell, et al. (1983) for Pahute Mesa events.

Table 7 - Summary of Effective Source Functions

Event	K (s^{-1})	B	Ψ (cm^3)	Mo (dyne-cm)	Depth (m)	Ann. Yield (kt)
DISCUS THROWER	16	1*	1.22×10^9	1.02×10^{20}	337	21
MUDPACK	23*	1*	9.90×10^7	8.30×10^{18}	155	2.7
MERLIN	20*	1*	3.37×10^8	2.82×10^{19}	296	10

* assumed values.

vertical component of velocity can be modeled using generalized rays for scaled slant ranges greater than $130 \text{ m/kt}^{1/3}$. Since this roughly corresponds to the depth of burial, this implies that source strength may be determined from surface gauges within the spall zone without having to resort to extensive modeling of non-linearity and spall or slap-down.

The scaling relationship which was derived relating Ψ_{∞} to yield implies that coupling is 2.5 times smaller for dry tuff and alluvium shots than for the wet tuff events at Pahute Mesa. The fact that once the region was calibrated by an event where the velocity structure is known in detail (such as DISCUS THROWER) a scaling relationship can be used to predict the yield of other events in the region can be of fundamental importance in threshold monitoring.

REFERENCES

- Barker, J. S., S. H. Hartzell, L. J. Burdick and D. V. Helmberger (1985). Effective source functions for underground nuclear tests at Pahute Mesa from near-field modeling, Final Technical Report WCCP-R-85-02, Woodward-Clyde Consultants, Pasadena.
- Burdick, L. J., D. M. Cole, D. V. Helmberger, T. Lay and T. Wallace (1982). Effective source functions from local surface measurements, Final Technical Report WCCP-R-82-01, Woodward-Clyde Consultants, Pasadena.
- Burdick, L. J., T. Wallace and T. Lay (1984). Modeling near-field and teleseismic observations from the Amchitka test site, J. Geophys. Res., 89, 4373-4388.
- Hartzell, S. H., L. J. Burdick and T. Lay (1983). Effective source functions for Pahute Mesa nuclear tests, Final Technical Report WCCP-R-83-3, Woodward-Clyde Consultants, Pasadena.
- Haskell, N. A. (1967). Analytic approximation for the elastic radiation from a contained underground explosion, J. Geophys. Res., 72, 2583-2587.
- Helmberger, D. V. (1968). The crust-mantle transition in the Bering Sea, Bull. Seismol. Soc. Am., 58, 179-214.
- Helmberger, D. V. and D. M. Hadley (1981). Seismic source functions and attenuation from local and teleseismic observations of the NTS events JORUM and HANDLEY, Bull. Seismol. Soc. Am., 71, 51-67.
- Langston, C. A. and D. V. Helmberger (1975). A procedure for modeling shallow dislocation sources, Geophys. J. Roy. astr. Soc., 42, 117-130.
- Lay, T., L. J. Burdick and D. V. Helmberger (1984). Estimating the yields of the Amchitka tests by waveform intercorrelation, Geophys. J. Roy. astr. Soc., 78, 181-208.
- Minster, J. B. and S. Day (1985). Decay of wavefields near an explosion source due to high strain, nonlinear attenuation, submitted to Bull. Seismol. Soc. Am..
- Perret, W. R. (1971). Free-field surface motion from a nuclear explosion in alluvium: MERLIN event, Report SC-RR-69-334, Sandia Laboratories, Albuquerque.
- Perret, W. R. and K. B. Kimball (1971). Ground motion induced in a multilayered earth by a contained nuclear explosion, Report POR-6400, Sandia Laboratories, Albuquerque.

- Perret, W. R. and R. C. Bass (1975). Free-field ground motion induced by underground explosions, Report SAND74-0252, Sandia Laboratories, Albuquerque.
- Rodean, H. C. (1981). Inelastic processes in seismic wave generation by underground explosions, in E. S. Husebye and S. Mykkeltveit - eds., Identification of Seismic Sources - Earthquake or Underground Explosion, D. Reidel, Dorchester.
- Stump, B. W. and L. R. Johnson (1984). Near-field source characterization of contained nuclear explosions in tuff, Bull. Seismol. Soc. Am., 74, 1-26.
- Trulio, J. (1978) Simple scaling and nuclear monitoring, Final Report, Applied Theory, Inc..
- vonSeggern, D. and R. Blandford (1972). Source time functions and spectra for underground nuclear explosions, Geophys. J. Roy. astr. Soc., 31, 83-97.

PART III

SIMULTANEOUS INVERSION OF NEAR-FIELD DATA

FOR SOURCE AND STRUCTURE PARAMETERS -

A PRELIMINARY ASSESSMENT

by

Jeffrey S. Barker and L. J. Burdick

INTRODUCTION

The determination of source parameters for underground nuclear explosions through waveform modeling of near-field recordings is dependent upon the velocity structure model assumed between the source and receivers. While independent information may exist for some aspects of the structure, such as the velocity at the surface and the depths to the water table and basement, the detailed models are generally the result of laborious trial-and-error modeling of observed waveforms (e.g., Helmberger and Hadley, 1981; Hartzell, et al., 1983; Burdick, et al., 1984). Discretizations of velocity gradients into plane-layered structure models must be fine enough to avoid introducing high frequency errors into the source function determinations. For signals with frequencies up to 5 Hz and compressional velocities near 3 km/s, layer thickness should be less than about 0.6 km. This is particularly important near the source depth due to the interference of upgoing and diving energy over near-field ranges. Thus an adequate structure model for near-field waveform modeling might consist of more than ten layers in the top 10 km of the crust. There is obviously a premium to be paid before undertaking the modeling of events at different test sites. Further, the structure model obtained is, to a certain extent, dependent upon the source function used during the modeling procedure. The result is clearly non-unique and the extent of the trade-offs cannot easily be quantified.

One solution to this problem is a simultaneous inversion for source and structure parameters. The complexity of wave interaction in the near-field makes such an inversion an approximate and somewhat costly endeavor. So, while the models obtained by such an inversion may not be intrinsically

"better" than their trial-and-error counterparts, a suitable choice of inversion method will automatically provide invaluable information concerning parameter and data resolution. Not only can the source vs. structure trade-offs be quantified in this way, but also the trade-offs within the source and structure parameterizations (such as the $B-\psi_{\infty}$ trade-off in the RDP) may be determined. We also obtain an indication of which aspects of the observed data are most important in constraining the solution.

This section of this report includes a discussion of the development of such an inversion, as well as preliminary tests of the structure model determination aspect using synthetic data sets. Application of the method to near-field data from Pahute Mesa and Yucca Flats events will be included in the Final Technical Report.

BACKGROUND

The vertical displacement due to an explosion source may be written using first order asymptotic Generalized Ray theory as (see for example, Helmberger and Harkrider, 1978)

$$w(r,t) = \psi'(t) * \frac{1}{\pi} \sqrt{\frac{2}{r}} \frac{d}{dt} \left(\frac{1}{\sqrt{t}} * \sum_i^{\text{rays}} R_i(p) \right) \quad (1)$$

where $*$ denotes convolution, $\psi'(t)$ is the time derivative of the reduced displacement potential (RDP), and

$$R_i(p) = \text{Im} \left(\frac{\sqrt{p}}{\eta_\alpha} R_{NZ}(p) \Pi_i(p) \frac{dp}{dt} \right)_c \quad (2)$$

which is evaluated along the Cagniard contour. p is the ray parameter, η_α is the vertical wave slowness ($\eta_\alpha = \sqrt{\alpha^{-2} - p^2}$), $R_{NZ}(p)$ is the receiver function defined by Helmberger (1974), and $\Pi_i(p)$ is the product of reflection and transmission coefficients along the path for each ray.

For the inversion, we need to compute the partial derivatives of (1) with respect to the individual parameters of the source and velocity structure. The partial with respect to structure parameters, say the velocity of the j th layer, v_j , reduces to the evaluation of

$$\frac{\partial R_i(p)}{\partial v_j} = \frac{\partial R_i(p)}{\partial p} \frac{\partial p}{\partial v_j} \quad (3)$$

which consists of evaluating the partials of the various terms in (2) as a function of the complex ray parameter along the Cagniard contour, while the contour itself varies with changes in the velocity parameter. This evaluation must be made for each ray, then summed to obtain the partial derivative.

Previous structure inversions based on waveform modeling have invoked a variety of approximations in order to simplify (3). Mellman (1980) utilized a modified first motion approximation, such that rapidly varying terms in (2) are approximated by evaluating them only at the geometric ray parameter. Shaw (1983) and Chapman and Orcutt (1985) used the WKBJ approximation to invert marine reflection/refraction data, and Brown (1982) employed a similar

approach to obtain the ocean sound speed profile. Since the WKBJ approximation becomes invalid where large velocity gradients exist, or where discontinuities are encountered near the turning depth of a ray, Given (1984) developed a hybrid WKBJ-Generalized Ray approach to obtain upper mantle structure. In inverting long-period, regional P_{n1} waveforms for average crustal structure, Wallace (1983) generated average Generalized Ray Green's functions, which were "stretched" or "squeezed" to simulate perturbations in the structure model.

In forward modeling of near-field waveforms, Burdick, et al. (1982) and Barker, et al. (1985) have shown that the observed waveforms result from the interference of upgoing and diving rays, as well as surface reflections. This interference is particularly sensitive to the velocity gradient near the source depth. Each synthetic seismogram consists of a superposition of rays from a variety of take-off angles that sample different portions of the structure. An algorithm designed to determine if and when the modified first motion, WKBJ and other approximations are appropriate for a particular ray, to compute the analytic partial derivatives, and sum over rays would seem to be of questionable efficiency and accuracy. Instead, numerical partials may be computed by evaluating the terms in (3) along the complex ray parameter for each ray. This approach is obviously nonlinear, and care must be taken to limit the model perturbations from which partials are computed and to damp the resulting parameter changes. For simpler problems, the computation of numerical partial derivatives would be terribly inefficient, but given the complexity of the near-field waveform modeling problem, the accuracy of the method will more than counterbalance the computational cost.

A number of techniques have been used to obtain source parameters by

inversion of body waveforms. Burdick and Mellman (1978) inverted teleseismic body waves to obtain the orientation and time history of the Borrego Mt. earthquake. Several investigators have inverted teleseismic body waves to obtain the seismic moment tensor. A few examples include Stump and Johnson (1977), Langston (1981), Dziewonski, et al. (1980) and Nabelek (1984). To our knowledge, the only inversion of near-field data for explosion source parameters was performed by Stump and Johnson (1984). In that study, they solved for the six independent elements of the moment tensor and interpreted the relative amplitudes and time histories of the isotropic part and deviatoric part in terms of explosion and tectonic release sources, respectively. Because the moment tensor was free to take on any value, and because the velocity structure model was fixed, it is entirely possible that errors in the structure model and noise in the data could map into the non-isotropic moment tensor. In addition, since no constraint was placed on the form of the isotropic time history, only the low-frequency level could be interpreted in terms of the parameters of an explosion RDP.

Because of our assertion that errors in the velocity structure adversely affect explosion source parameter estimates, we are interested in approaching these problems before tackling source complexity. Therefore, our preliminary inversions will constrain the explosion source to be isotropic and we will constrain the source time history to have the form of the time derivative of the RDP. Various forms of the RDP will be considered. After evaluating these results, the source parameterization could be generalized to allow the source time history to take on an arbitrary shape. At a later stage, a deviatoric moment tensor source representing tectonic release could be added to the isotropic source, with the latter constrained to the known depth and origin

time of the explosion. Inverting for a single, six-component moment tensor, however, constrains the non-isotropic portion of the source to occur at the same location as the explosion. While this may turn out to be the case, near-field observations should allow resolution of spatial separations in the two sources, so such a constraint may be unreasonable.

INVERSION METHOD

The layered structure models required for Generalized Ray synthetics may be considered discretizations of one or more velocity gradients separated by first- or second-order discontinuities. In order to minimize the number of free parameters in the inversion, we will utilize this fact and solve not for the velocities and thicknesses of individual layers, but for the velocity gradient and the velocity at the top of the gradient. The discretized model will follow this gradient, with layer thicknesses determined by the wavelength of the predominant period in the data. Shear velocity and density may be free parameters, or may be related to the compressional velocity by predefined constants. In general, the free parameters are the gradient within each layer, the velocity at the top of the layer, and the depth to the top of the layer. Thus, for an n -layered structure in which shear velocity and density are not free parameters, the number of structure parameters in the inversion is $3n-1$. The number of gradients to be considered will be fixed for each inversion, so the optimal number will have to be determined by test inversions proceeding from simpler to more complex models. Constraints such as the depth to the water table, or that a particular interface may have only a

second-order discontinuity, reduce the number of free parameters while increasing non-linearity of the inversion.

Since the discretized velocity model will vary from iteration to iteration as well as with the model perturbations required to compute the numerical partials, the ray set from which the synthetics are computed will also vary. Barker, et al. (1985) found that the first one or two cycles of vertical velocity observations at near-field ranges were well modeled by including the upgoing direct ray, a sum of diving rays that constitute turning, reflecting and critically refracting energy, and a sum of rays that depart upward, reflect from the free surface and follow diving ray paths. If radial observations are to be modeled, or if later portions of the waveform are considered, P-to-S conversions at the free surface and at discontinuities should be included. An algorithm to generate this ray set for each new layered structure is simple to implement, and computational time is saved by culling rays which arrive outside the inversion time window, or whose amplitude will be below some predefined cutoff level.

The source parameterization follows the form of the RDP proposed by Haskell (1967):

$$\Psi(t) = \Psi_{\infty} \left(1 - e^{-Kt} [1 + Kt + (Kt)^2 + (Kt)^3 - B(Kt)^4] \right) \quad (4)$$

where Ψ_{∞} represents the static value, K represents the rise time, and B represents the overshoot. Helmberger and Hadley (1981) truncated the polynomial in (4) to cubic, while vonSeggern and Blandford (1972) suggest that it should be quadratic. The effective source function for any of these forms may be obtained by taking the first (displacement), second (velocity) or third

(acceleration) time derivatives of the RDP. As may be seen from (4), the RDP and its time derivatives are linear in Ψ_{∞} and B, but not in K. Analytic partial derivatives may be computed for Ψ_{∞} and B, but we will rely on numerical partial derivatives for K. The computation of the effective source functions is quite fast, and the difference may be computed before the convolution in (1). The first section of this report indicated that Ψ_{∞} and B trade off nearly totally in modeling near-field velocity records. While this trade-off may be quantified by allowing both parameters to vary in the inversion, useful source estimates may require that B be constrained.

The linearized least-squares inverse may be obtained by solving

$$\Delta c' = A' \Delta p' \quad (5)$$

in which $\Delta c'$ is the residual vector, containing the differences between observed and synthetic data, A' is the matrix of partial derivatives, and $\Delta p'$ is the desired vector of parameter changes. Perhaps the simplest determination of the residual vector is a point-by-point difference of observed and synthetic seismograms within the time window. This implies, however, that neighboring points in a seismogram represent independent observations, which is generally not the case. On the other hand, since each seismogram reflects a lagged sum of rays which sample different portions of the structure, the resolution of parameters varies through the time window, and a single observation for each seismogram underestimates the information contained in the waveform.

Burdick and Mellman (1978) utilized an error, or residual, function based on the normalized cross-correlation coefficient between observed and synthetic

waveforms. That is,

$$e_i = 1 - \max(\hat{o}_i \text{ cc } \hat{s}_i) \quad (6)$$

where

$$\hat{o}_i(t) = \frac{o_i(t)}{(\int o_i^2(t) dt)^{1/2}} \quad (7)$$

and

$$\hat{s}_i(t) = \frac{s_i(t)}{(\int s_i^2(t) dt)^{1/2}} \quad (8)$$

$o_i(t)$ is the i th observed seismogram, $s_i(t)$ is the i th synthetic seismogram and cc denotes cross-correlation. This error function has become popular because it is sensitive to the shapes of the waveforms, while the normalization makes it insensitive to absolute amplitude, and measuring the maximum of the cross-correlation makes it insensitive to absolute time. In the near-field problem, however, absolute amplitude and time are well calibrated, and must be fit by the resultant model. Therefore, in addition to (6), our residual will include for each seismogram the relative difference in the normalization factors,

$$a_i = \frac{(\int o_i^2(t) dt)^{1/2} - (\int s_i^2(t) dt)^{1/2}}{(\int o_i^2(t) dt)^{1/2}} \quad (9)$$

which is a measure of absolute amplitude residual, and the time lag to the maximum of the cross-correlation, t_i , which is a measure of absolute time residual. The residual vector is now defined as

$$\Delta c' = [e_1, a_1, t_1, e_2, a_2, t_2, \dots, e_m, a_m, t_m]^T \quad (10)$$

for m seismograms and the objective function to be minimized by the inverse is

$$r = \sum_m (e_i^2 + a_i^2 + t_i^2) . \quad (11)$$

With this choice for the residual function, the numerical partial derivatives become, rather than (3),

$$\frac{\partial e_i}{\partial p_j} = \frac{(e_i(p_j + \Delta p_j) - e_i(p_j - \Delta p_j))}{2 \Delta p_j} \quad (12)$$

where Δp_j is the perturbation to the starting model parameter, p_j . The partials $\partial a_i / \partial p_j$ and $\partial t_i / \partial p_j$ have similar form.

Now that we have defined the form of the residual and parameter change vectors, we may redefine the matrices in (5) as

$$\Delta c = s^{-1/2} \Delta c'$$

$$\Delta p = w^{-1/2} \Delta p' \quad (13)$$

$$A = s^{-1/2} A' w^{1/2}$$

in which s and w are the covariance matrices of the observations and parameters, respectively. The basic purpose of these weighting factors is to counter the dimensionality of the residuals and the parameterization of source and structure. For simplicity, we assume that errors are uncorrelated. If an estimate of the variance is known (e.g., timing errors), that value is used as the weighting factor. Otherwise, weights are assigned based on an estimate of the dimensions. For example, waveform residuals will have values between 0.0 and 1.0, while absolute time residuals are more likely to be less than 0.1s. Similarly, a reasonable variation in the velocity at the top of a layer might be about 1 km/s, while the variation in gradient might be about 0.1 km/s/km. The weighting factors may also be modified to tailor the sensitivity of the inversion. For instance, we may wish to preferentially fit absolute travel time at the expense of slight waveform mismatches. In this case, we would decrease the time residual variance relative to that of the waveform residual. Following Jackson (1979), a priori constraints may be placed on the parameter changes so that, for example, the velocity at the top of a layer cannot be negative, or so that source parameters must fall within a range of reasonable values.

The weighted version of (5) may be solved by a linearized generalized

inverse (Wiggins, 1972) such that

$$\Delta p = A^+ \Delta c = V \Lambda^{-1} U^T \Delta c \quad (14)$$

in which Λ is the diagonal matrix of non-zero singular values of A , V is the corresponding matrix of eigenvectors which spans the parameter space, and U is the matrix of eigenvectors that spans the residual space. Since the problem is non-linear, the inversion is iterative and minimizes both the least-squares error, $|A \Delta p - \Delta c|^2$, and the length of the parameter changes, $|\Delta p|^2$. Since small singular values result in large parameter changes, an a priori cut-off is specified, below which the singular value is assumed to be zero, and the dimension of the parameter space is truncated. The resulting parameter trade-offs may be determined by an inspection of the parameter resolution matrix,

$$R = V V^T, \quad (15)$$

which reduces to the identity matrix in the case of perfect resolution. If during test inversions, the parameter resolution is deemed unacceptable, adjustments may be made in the parameter weights or the singular value cut-off, and the inversion may be repeated. The importance of particular observations or residuals in the inversion may be determined from the information density matrix,

$$S = U U^T. \quad (16)$$

This may indicate, for example, that the parameter changes are most sensitive to the absolute amplitude residual at nearer receivers, and to the absolute time residual at more distant receivers. The information density matrix from test inversions may suggest modifications to the observation weights.

Finally, since most of the partial derivatives in A are determined numerically, some care must be taken in determining the size of the parameter perturbations from which the partials are computed. In addition, particularly in the presence of local minima in the residual space, it may be necessary to constrain or damp the parameter changes, and it may be useful to utilize second derivative information. Some of these points will be discussed in the examples of preliminary inversions to follow.

PRELIMINARY ASSESSMENT OF STRUCTURE INVERSION

As a simple initial test of the inversion for velocity structure, we generated a synthetic data set for an explosion source in a halfspace. The compressional velocity in the halfspace was 6.0 km/s, the shear velocity was 3.44 km/s (a Poisson solid) and the density was 3.0 g/cm³. The source was represented by a Helmberger-Hadley (1981) RDP with $K=7.0 \text{ s}^{-1}$, $B=1.0$ and $\Psi_{\infty}=1.0 \times 10^{10} \text{ cm}^3$, and was located at a depth of 1.0 km. Vertical component velocity synthetics were computed for ranges of 2, 4, 6, 8, 10 and 12 km. Since the object of the test inversion is the halfspace velocity, we constrain

the structure to be a single layer with a zero velocity gradient.

In such a simple case, it is instructive to investigate the residuals as a function of the parameter values. In Figure 1 are the waveform residuals, e_1 , absolute amplitude residuals, a_1 , and travel time residuals, t_1 , plotted as functions of receiver distance and halfspace velocity. Velocities from 5.0 to 7.0 km/s are considered in increments of 0.25 km/s. Since the body waveforms do not change with variations in the halfspace velocity, the variations in waveform residuals are due to the truncation of the synthetic waveform as it is shifted with respect to the time window. The waveform residual is zero only when there is a perfect match: at the correct halfspace velocity of 6.0 km/s. Similarly, the absolute amplitude residual does not represent the difference in peak amplitudes between observed and synthetic waveforms, but rather the difference in the peak values of their autocorrelations. So, systematic amplitude variations due to velocity changes are superposed with truncation effects due to the time shifts relative to the window. Amplitude residuals may take on positive and negative values, and the sign is important in determining the partials. Only at the correct velocity (6.0 km/s) are the amplitude residuals at all of the receivers zero. The most sensitive measure of the correct halfspace velocity appears to be the travel time residual. This residual is linearly decreasing at all receivers for increasing halfspace velocity and, of course, the most distant receivers are most sensitive to variations in the velocity. The travel time residual is zero at all receivers for the correct velocity.

For simple problems with only a couple of free parameters, a grid-searching approach in which the minimum of the residuals is found by stepping through the parameter space, would be quite reasonable, particularly

Halfspace Model Residuals

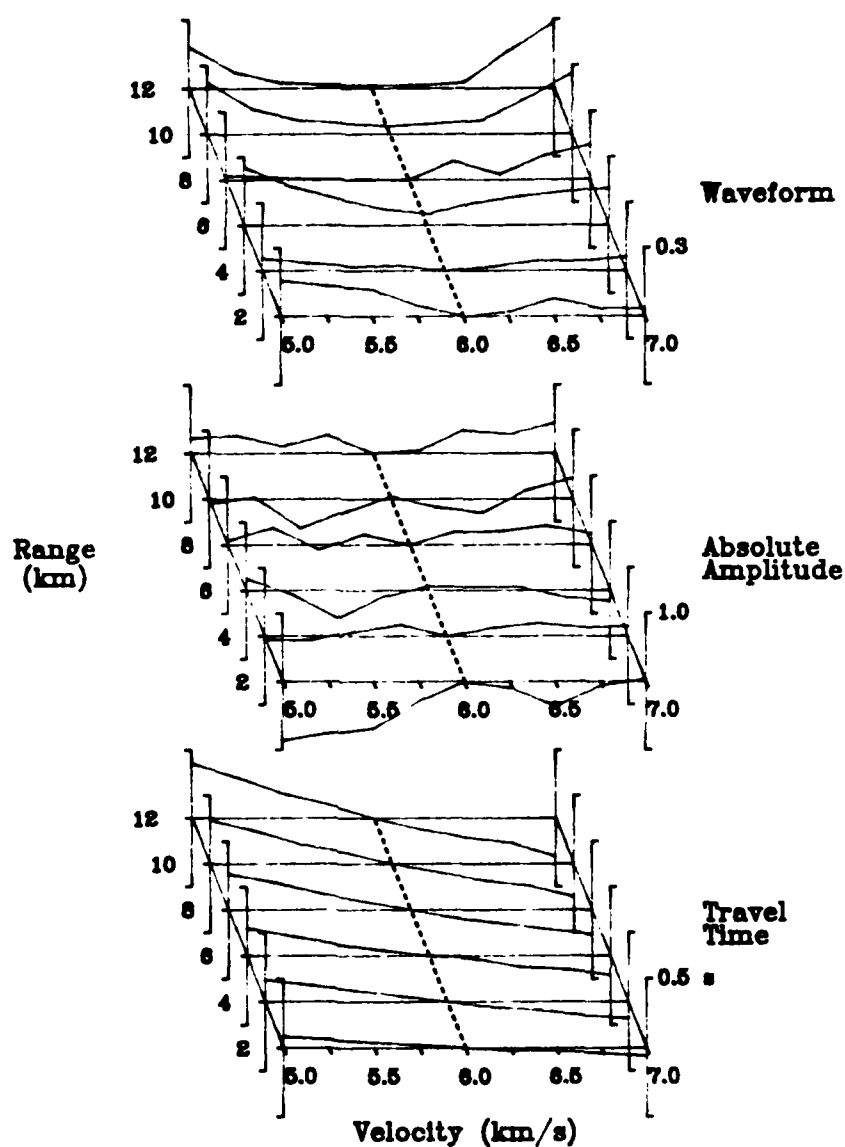


Figure 1. Waveform, absolute amplitude and travel time residuals for the halfspace model as functions of receiver distance and velocity. The correct velocity is 6.0 km/s.

in the presence of local minima. This is essentially the procedure used to generate Figure 1. The grid-searching approach, however, becomes quite unwieldy when the number of free parameters exceeds three or four, and does not readily supply information on the relative resolution of the parameters. In anticipation of more complex problems, therefore, we have performed the generalized inverse for the test case of determining the halfspace velocity from a starting model with a velocity of 5.0 km/s. If we were to invert only the travel-time residuals, Figure 1 indicates that the inversion would be linear. However, since the partials are computed by a linear difference of the residuals, the curvature in the waveform and amplitude residuals requires an iterative scheme. A 10% perturbation in velocity is used to compute the partials. Accounting for the dimensionality of the residuals, and utilizing the observation that travel time residuals appear to be most sensitive to halfspace velocity, we define the covariance matrix of the observations to be $\text{diag}(1.0, 1.0, 0.1)$ for the waveform, amplitude and time residuals at each receiver, respectively. Since there is only one parameter, the covariance of the velocity is set to 1.0. Five iterations were allowed, with no constraint or damping placed on the parameter changes. The results are tabulated in Table 1, and the waveforms for each iteration are plotted in Figure 2.

After only two iterations, the velocity determined is within 0.5% of the correct value, and convergence is complete after four iterations. The quality of fit may be determined by inspecting the waveforms in Figure 2, or by two objective measures listed in Table 1. The RMS fit is defined as $\text{RMS} = \sqrt{r / 3 \cdot m}$, where r is the objective function (11) which is the sum of the squared residuals and $3 \cdot m$ is the total number of residuals. The least-squares error is $\text{LSE} = |A \Delta p - \Delta c|^2$, and is a measure of the linearity of the

Table 1 - Halfspace Velocity Inversion Results

<u>Iteration</u>	<u>α (km/s)</u>	<u>RMS fit</u>	<u>Least-square error</u>
Start	5.000	0.277	
1	5.629	0.137	1.978
2	5.969	0.130	0.280
3	5.987	0.056	0.308
4	5.999	0.001	0.056
5	5.999	0.012	0.0002
Data	6.000		

inversion at each iteration. In initial inversions, the time windows were chosen to include the halfspace Rayleigh wave at each receiver. This, however, causes a strong local minimum to be formed at low velocities when the "synthetic" P wave correlates with the "observed" Rayleigh wave. Although the Generalized Ray synthetics are exact for the halfspace Rayleigh wave, they are generally inadequate for modeling surface waves for more complicated structures. For both of these reasons, the inversion time windows were shortened to exclude the Rayleigh wave where it is separable from the P wave.

For a somewhat more realistic test, and in order to test the discretization and ray summing procedures, a synthetic data set was generated for a single velocity gradient. The compressional velocity at the surface was set to 3.5 km/s and the velocity gradient was 0.5 km/s/km. The shear velocity was constrained to that of a Poisson solid ($1/\sqrt{3}$ times the compressional velocity) and the density was constrained to $1/2$ the compressional velocity. The gradient was discretized using a predominant period of 0.25 s, which results in 10 layers in the top 15 km with layer thickness increasing with

Halfspace Velocity Inversion Results

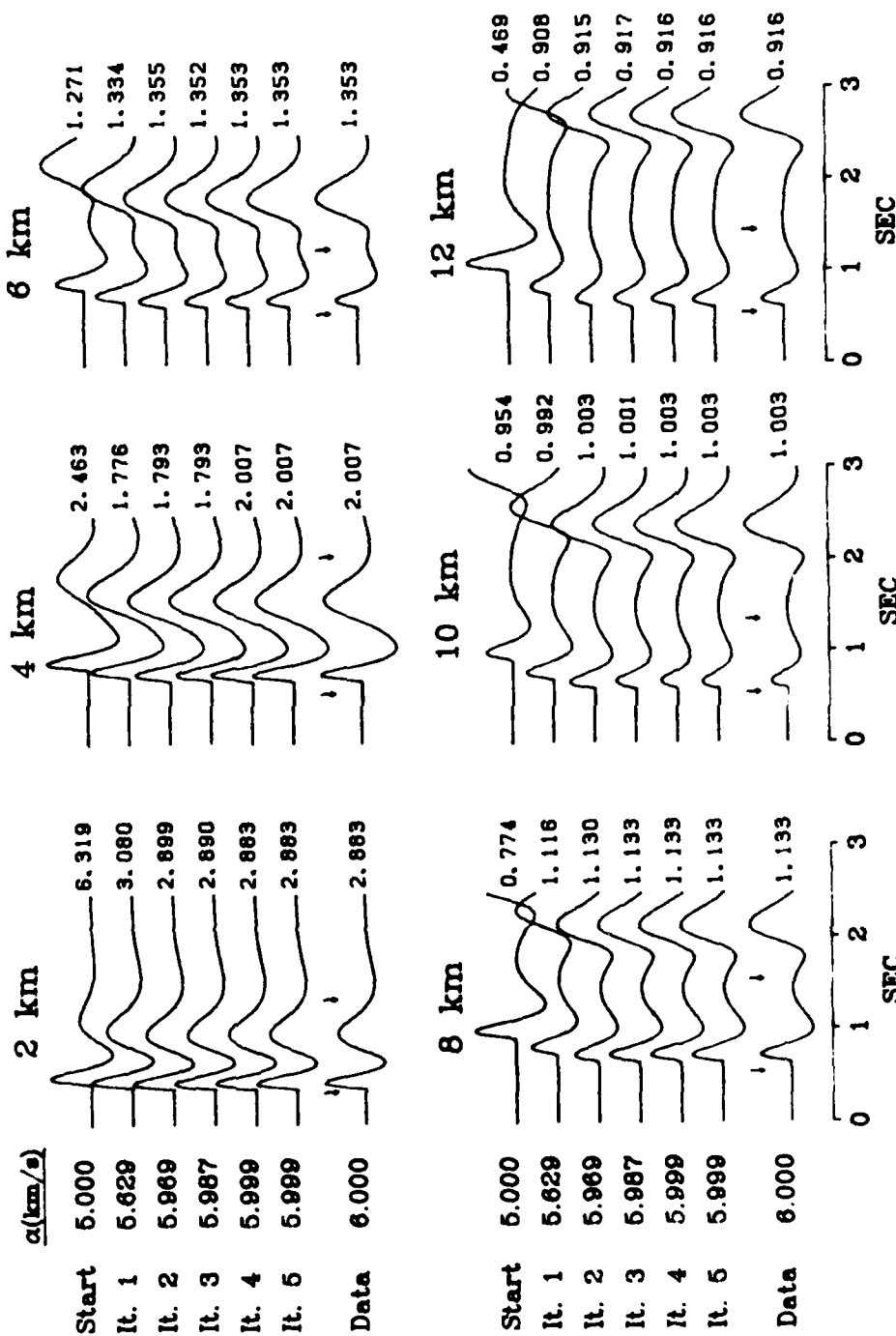


Figure 2. Results of the halfspace velocity inversion. Synthetic seismograms are shown for the starting model and five iterations at each receiver. The data seismograms (also synthetic) are plotted below. Arrows above the data waveforms indicate the inversion time windows and numbers to the right are the peak trace amplitudes. The values of the parameter (halfspace velocity) for each iteration, and the correct value of the data, are shown to the left.

depth. All upgoing and diving direct P waves and the surface-reflected pP waves were considered, but culling late arriving rays resulted in 18 rays being summed for the final response. Once again, synthetic velocity seismograms were computed for ranges of 2, 4, 6, 8, 10 and 12 km.

Figures 3 and 4 illustrate the dependence of the waveform, absolute amplitude and travel time residuals at each receiver as functions of the velocity gradient and the velocity at the surface, respectively. As shown in Figure 3, since the waveforms at the nearer receivers are dominated by the upgoing P wave, which is relatively insensitive to the velocity gradient, there is very little variation in their residuals over the ranges of gradient considered (0.3 to 0.7 km/s/km). On the other hand, the waveforms at the farther receivers are dominated by diving turning rays, and their residuals (particularly travel time) can resolve changes in the gradient. Overall, it appears that velocity gradient, in this simple example, will be resolved by travel time residuals at farther receivers and amplitude residuals at all receivers. The residuals due to variations in surface velocity (Figure 4) are very similar to those for the halfspace test (Figure 1). The waveform residuals have a broad minimum, the travel time residuals are a robust measure of the correct surface velocity, and the amplitude residuals include variations due to truncation by the time window. In comparing Figures 3 and 4, it appears that the residuals are more sensitive to variations in surface velocity than velocity gradient. We will have to take this into account in assigning parameter weights in the inversion.

Before performing an inversion for surface velocity and gradient, it is instructive to invert for gradient only, constraining the surface velocity to its correct value. In this case, we define the covariance matrix of the

Gradient Model Residuals

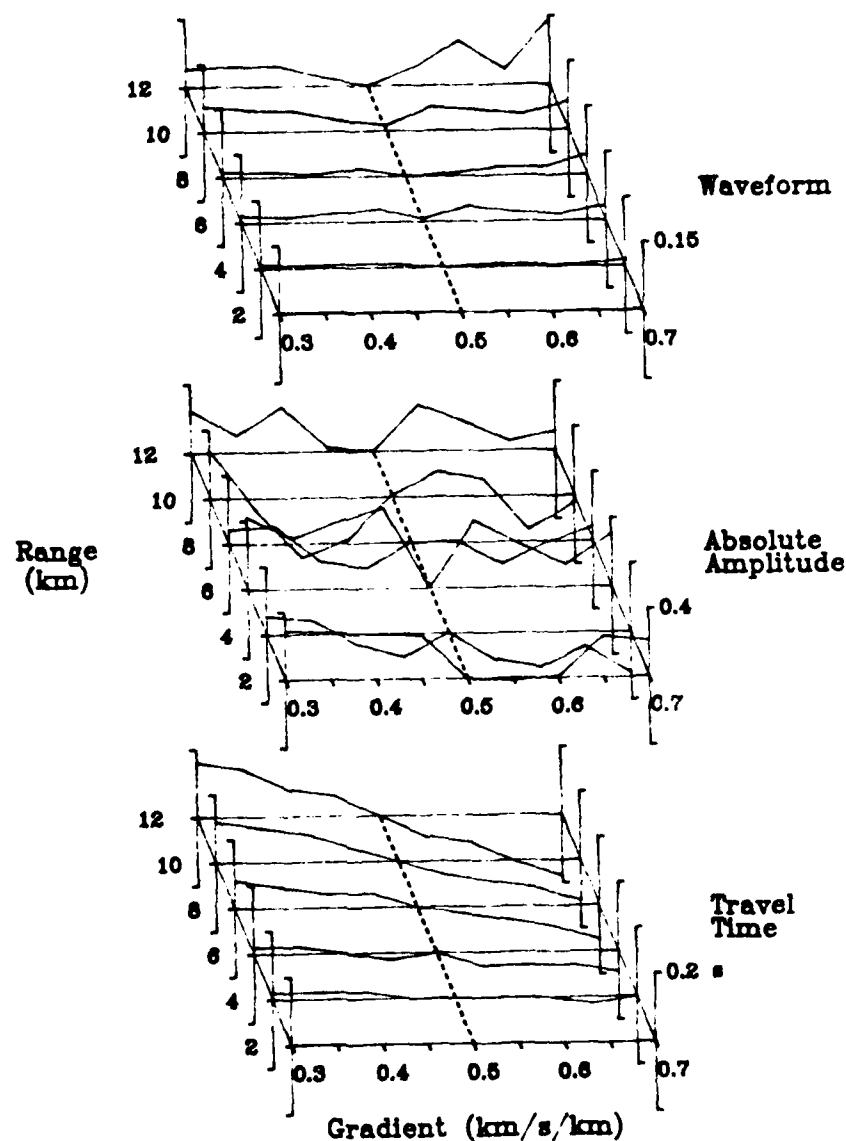


Figure 3. Waveform, amplitude and time residuals for the gradient model as functions of receiver distance and gradient. The correct gradient is 0.5 km/s/km.

Gradient Model Residuals

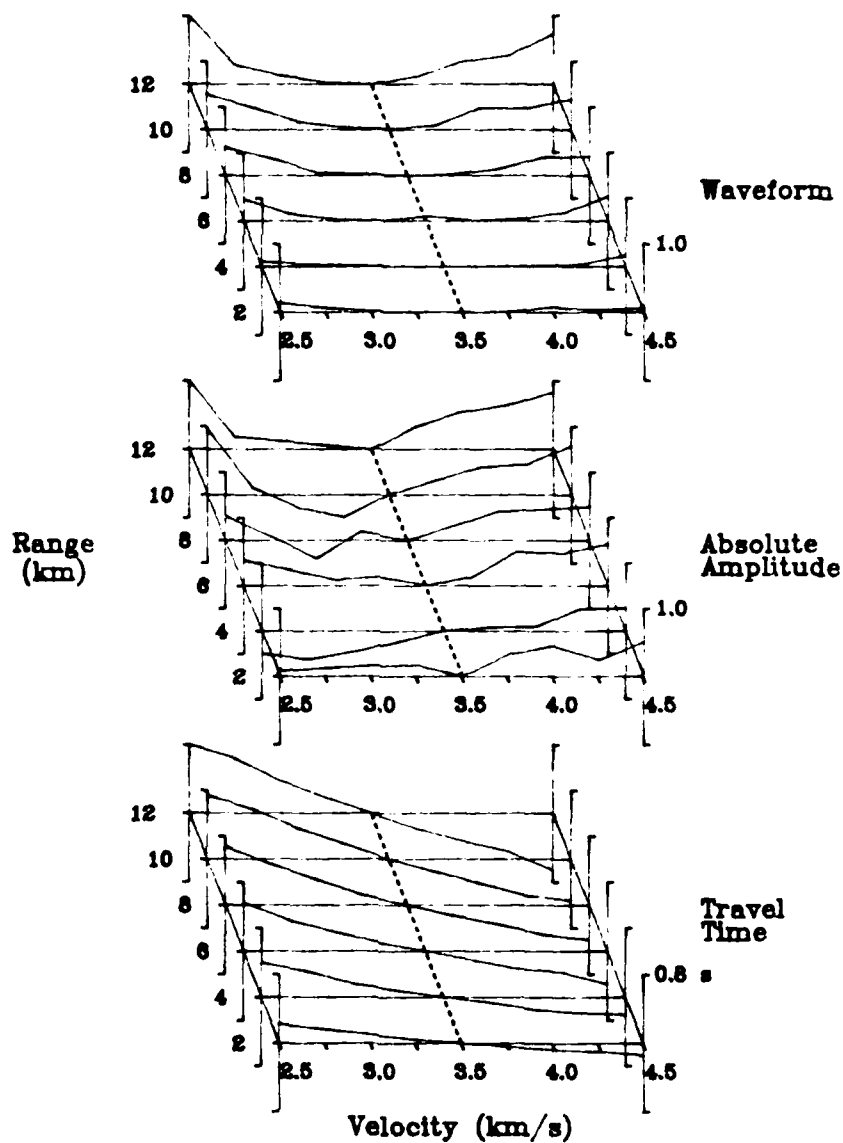


Figure 4. Waveform, amplitude and time residuals for the gradient model as functions of receiver distance and the velocity at the surface. The correct velocity is 3.5 km/s.

observations according to the dimensionality of the residuals, but in addition, we wish to preferentially minimize the waveform residuals since changes in gradient appear to have significant effect on the details of the waveform. We define the matrix to be $\text{diag}(0.01, 1.0, 0.1)$ for waveform, amplitude and time residuals at each receiver, respectively. Partial derivatives are computed by 10% perturbations in the gradient, beginning with a gradient of 0.6 km/s/km. The correct gradient is 0.5 km/s/km. Five iterations were allowed with no damping of parameter changes. The results of the inversion are listed in Table 2 and the waveforms for each iteration are plotted in Figure 5.

Convergence to the solution is much more difficult in this case. An inspection of the information density matrix indicates that the first iteration is primarily controlled by the waveform and travel time residuals at the 12 km receiver, with some influence by the waveform and amplitude residuals at 6 km. After this initial step toward the correct solution, the second and third iterations are controlled by the amplitude residuals at 6 and 10 km. As may be seen in Figure 3, the amplitude residuals at these receivers vary more rapidly for gradients slightly less than 0.5 km/s/km than for those slightly greater than 0.5 km/s/km. In the second iteration, the partial derivatives are computed based on the difference in the residuals at 0.573 and 0.469 km/s/km. Even though the latter is closer to the correct solution (0.5 km/s/km), its amplitude residual is larger in absolute value than the former, so the partial derivative of the amplitude residuals causes the solution to move away from the correct gradient. By the fourth iteration, the solution has moved far enough away that the lower bracket value used in computing the partials is approximately 0.5 km/s/km, and the partial is unaffected by the

Table 2 - Gradient Inversion Results

Iteration	$\frac{d\alpha}{dz}$ (km/s/km)	RMS fit	Least-square error
Start	0.600	0.102	
1	0.522	0.052	1.015
2	0.529	0.107	0.125
3	0.560	0.083	2.128
4	0.497	0.047	0.080
5	0.471	0.117	0.088
Data	0.500		

changes in the residuals for smaller gradients. It is clear from this discussion that some information on the second derivatives of the residuals is needed in determining the parameter changes.

Finally, we have performed several test inversions for simultaneously determining velocity gradient and surface velocity. There is an obvious trade-off between these parameters, indicating the need to truncate small singular values. In addition, however, the parameters should be weighted beyond that required by the dimensionality of the parameters. Figures 3 and 4 illustrated that the inversion appears to be more sensitive to variations in surface velocity than gradient. This means that a given residual value may be due either to a reasonable variation in surface velocity or a relatively larger variation in gradient. Since the inversion is non-linear, an error in surface velocity will be only partially corrected, while the gradient varies substantially to compensate. Inversions in which the parameters are equally weighted, or in which gradient is preferentially weighted will diverge. We

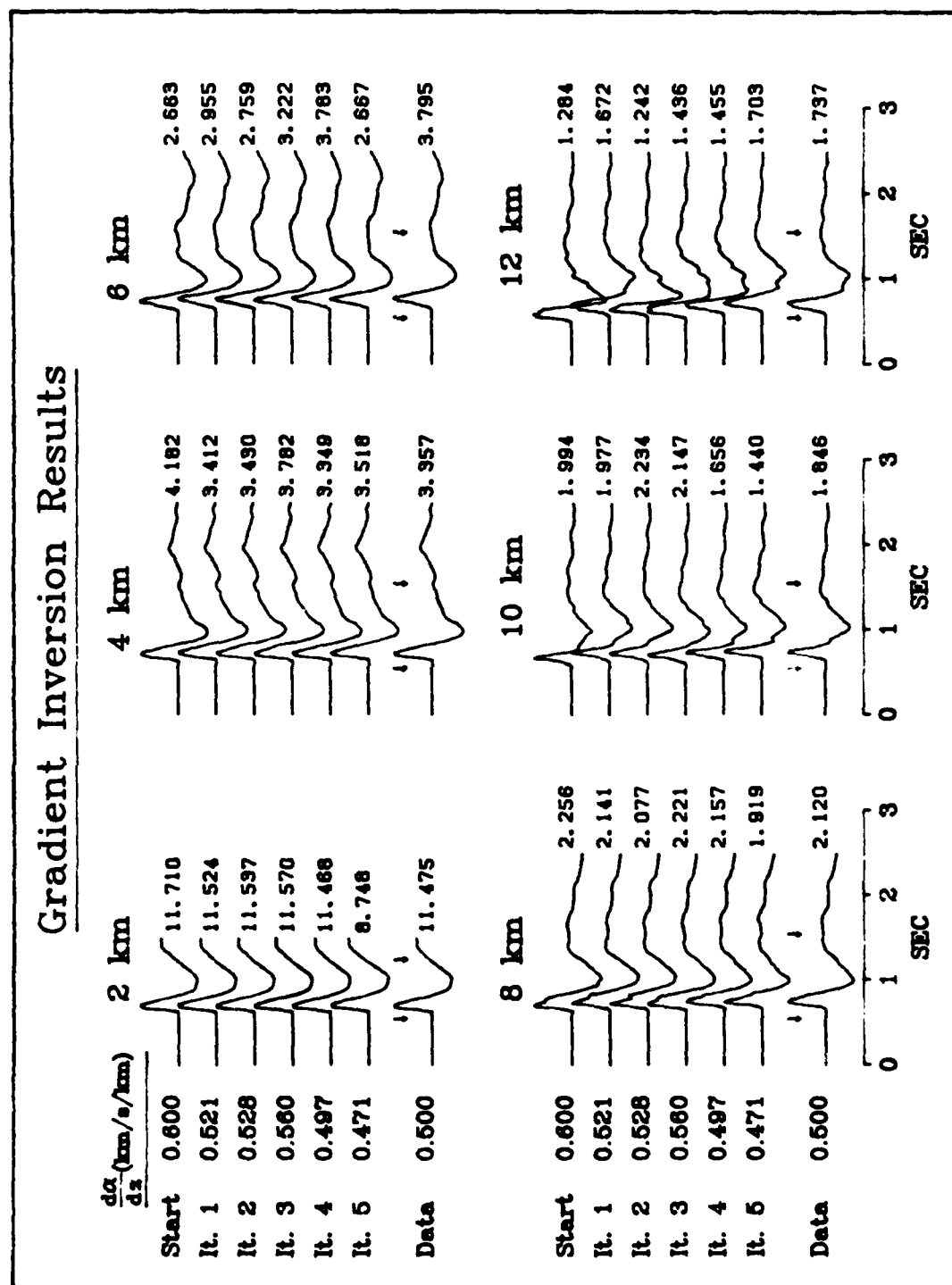


Figure 5. Results of the inversion for velocity gradient. The format is the same as in Figure 2, except that the parameter shown on the left is velocity gradient in km/s/km.

have therefore defined the covariance matrix of the parameters such that surface velocity is preferentially weighted as $\text{diag}(1.0, 0.1)$ for surface velocity and gradient, respectively. The covariance matrix of the observations is $\text{diag}(0.1, 1.0, 0.1)$ for waveform, amplitude and travel time residuals, respectively. A cut-off was established so that one of the singular values could be truncated to avoid large variations due to poor resolution. Perturbations of 10% were used to generate the partials. Ten iterations were allowed from a starting model with surface velocity of 2.5 km/s and a gradient of 0.4 km/s/km. The correct solution had a velocity of 3.5 km/s and a gradient of 0.5 km/s/km.

The results of the inversion are listed in Table 3, and the waveforms from chosen iterations are shown in Figure 6. In the first iteration, both parameters are perfectly resolved and the change is toward the correct solution for both. In the second and following iterations, one singular value has been truncated. The weighting scheme has ensured that the remaining eigenvector is oriented in the parameter space mostly in the direction of surface velocity, but with a small component in the gradient. This means that the second and following iterations consist mainly of modifications to the surface velocity, with only small (and perhaps incorrect) modifications to the gradient. This is also indicated by the diagonals of the resolution matrix, which are included in Table 3. After about five iterations, the model is slightly low in surface velocity, which is counteracted by a slightly high gradient. The waveforms from this combination are close enough to those of the correct solution, that parameter perturbations are relatively small in later iterations. Figure 6 shows that the primary effect of these later perturbations is to improve the absolute amplitude, since travel time and

Table 3 - Gradient and Surface Velocity Inversion Results

Iteration	α (km/s)	R^*	$\frac{d\alpha}{dz}$ (km/s/km)	R^*	RMS fit	LSE
Start	2.500		0.400		0.598	
1	2.751	1.000	0.495	1.000	0.311	25.9
2	2.994	0.967	0.509	0.033	0.238	10.1
3	3.331	0.921	0.540	0.079	0.156	1.01
4	3.453	0.936	0.550	0.064	0.139	0.409
5	3.458	0.842	0.551	0.158	0.094	0.369
6	3.437	0.947	0.549	0.053	0.144	0.184
7	3.439	0.947	0.549	0.053	0.151	0.406
8	3.432	0.917	0.549	0.083	0.140	0.470
9	3.456	0.967	0.550	0.033	0.129	0.363
10	3.466	0.881	0.551	0.119	0.078	0.311
Data	3.500		0.500			

* value of the diagonal of the resolution matrix for this parameter.

waveshape are already fairly well fit. This indicates that it may be desirable to allow the covariance matrix of the observations to change for later iterations, to allow the amplitude residual more influence on the solution.

CONCLUSIONS

We have introduced a method for the simultaneous inversion of near-field waveforms for source and structure parameters. The source may be represented by any of a number of effective source functions. The structure model is

Inversion for Surface Velocity and Gradient

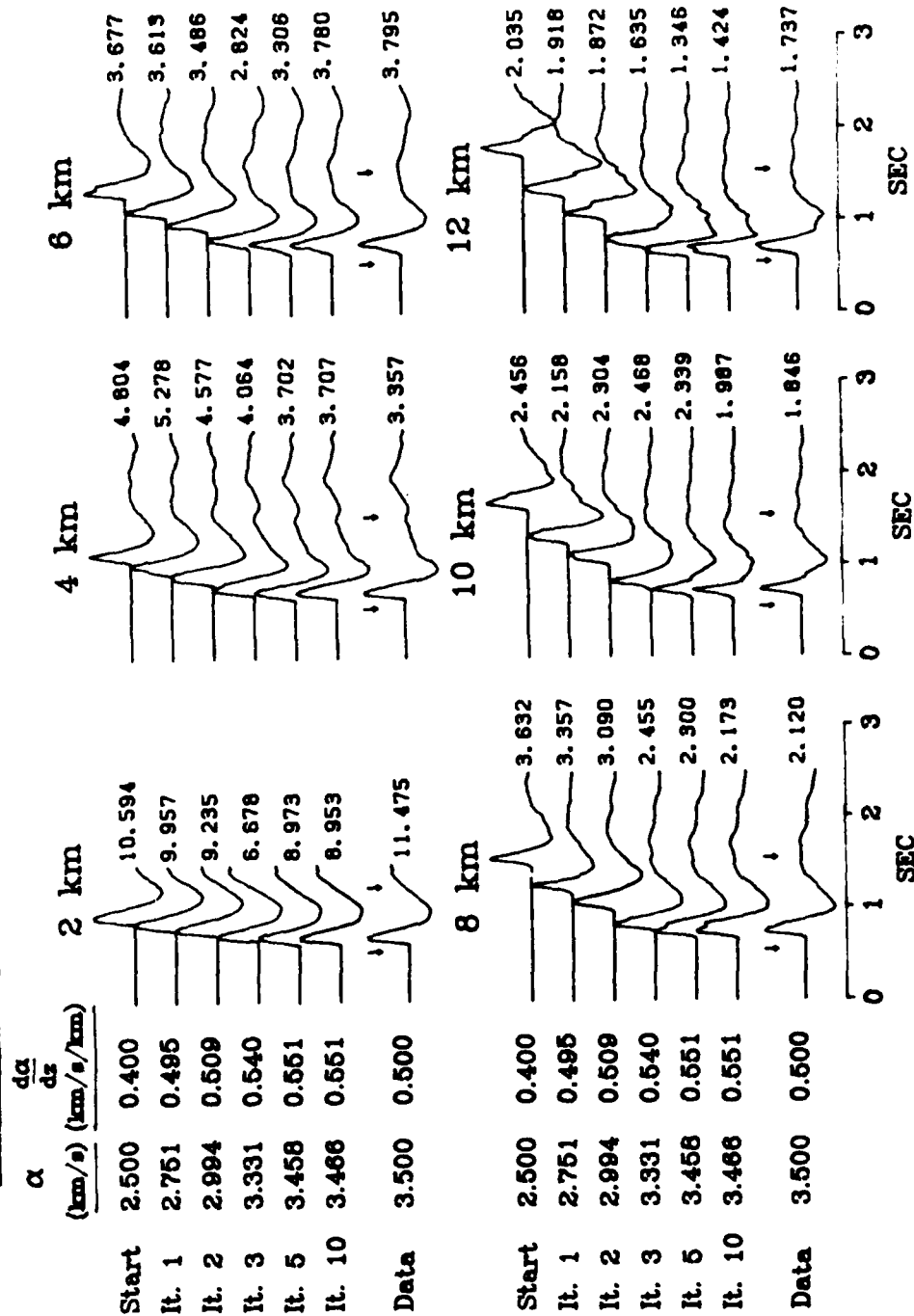


Figure 6. Results of the simultaneous inversion for gradient and velocity at the surface. The format is the same as in Figure 2, except that both parameters are printed on the left.

parameterized as a layered stack, in which the free parameters are the velocity at the top of each layer, the velocity gradient within the layer and the depth to the top of the layer. For each observation, the residuals consist of the normalized cross-correlation coefficient between the data and synthetics (a measure of waveform fit), the difference of the normalizations (a measure of absolute amplitude), and the time lag to the peak of the cross-correlation (a measure of absolute travel time). Numerical partial derivatives are computed using asymptotic Generalized Ray synthetics, and the problem is solved using an iterative generalized inverse.

Test inversions have been performed for simple structure models. The inversion for halfspace velocity is quite robust, but an inversion for a single gradient indicates that the curvature of the residuals in the parameter space causes the linear difference scheme for computing the partials to be inadequate. Information on the second derivatives of the residuals could solve this problem. In solving for both surface velocity and gradient, these parameters trade off. Without adequate weighting of the parameters, the inversion diverges. However, utilizing the fact that the inversion is more sensitive to surface velocity than gradient, and truncating singular values to damp poorly resolved parameter changes, causes the inversion to slowly approach the correct solution. Preferential weighting of the different residuals as a function of iteration may improve convergence.

Applying the simultaneous inversion for source and structure parameters to actual data will not be a simple task. Noise in the data and constraints in the parameterizations will compound the uncertainty caused by parameter trade-offs. By adjusting parameter and observation weights, and progressing from simple to more complex parameterizations, it should be possible to obtain

a solution comparable to those obtained by trial-and-error modeling. The inversion, however, provides two additional benefits that trial-and-error modeling cannot: (1) it automatically provides a quantitative measure of the resolution of the parameters and the importance of the observations in obtaining the solution, and (2) it avoids the tedious and ambiguous process of defining a detailed structure model for a given site before solving for source parameters. Further tests will investigate the trade-offs in multiple gradient models, as well as the effect of different source parameterizations on the structure determination. Following this, we will apply the inversion to observed near-field data from Pahute Mesa and Yucca Flats, which we have previously modeled using trial-and-error techniques. If this proves fruitful, the next step will be to invert near-field data from different test sites, such as the GASBUGGY, RULISON and RIO BLANCO events.

REFERENCES

- Barker, J. S., S. H. Hartzell, L. J. Burdick and D. V. Helmberger (1985). Effective source functions for underground nuclear tests at Pahute Mesa from near-field modeling, Final Technical Report WCCP-R-85-02, Woodward-Clyde Consultants, Pasadena.
- Brown, M. G. (1983). Inverting for the ocean sound speed structure, Ph.D. thesis, UCSD.
- Burdick, L. J. and G. R. Mellman (1976). Inversion of the body waves from the Borrego Mountain earthquake to the source mechanism, Bull. Seismol. Soc. Am., 66, 1485-1499.
- Chapman, C. H. and J. A. Orcutt (1985). Least-squares fitting of marine seismic refraction data, Geophys. J. Roy. astr. Soc., 82, 339-374.
- Dziewonski, A. M., T.-A. Chou and J. H. Woodhouse (1981). Determination of earthquake source parameters from waveform data for studies of global and regional seismicity, J. Geophys. Res., 86, 2825-2852.
- Given, J. W. (1984). Inversion of body-wave seismograms for upper mantle structure, Ph.D. thesis, Caltech.
- Hartzell, S. H., L. J. Burdick and T. Lay (1983). Effective source functions for Pahute Mesa nuclear tests, Final Technical Report WCCP-R-83-3, Woodward-Clyde Consultants, Pasadena.
- Haskell, N. A. (1967). Analytic approximation for the elastic radiation from a contained underground explosion, J. Geophys. Res., 72, 2583-2587.
- Helmberger, D. V. (1974). Generalized ray theory for shear dislocations, Bull. Seismol. Soc. Am., 64, 45-64.
- Helmberger, D. V. and D. G. Harkrider (1978). Modeling earthquakes with generalized ray theory, in J. Miklowitz and J. Achenback - eds., Proc. of IUTAM Symposium: Modern Problems in Elastic Wave Propagation, J. Wiley & Sons, New York.
- Helmberger, D. V. and D. M. Hadley (1981). Seismic source functions and attenuation from local and teleseismic observations of the NTS events JORUM and HANDLEY, Bull. Seismol. Soc. Am., 71, 51-67.
- Jackson, D. D. (1979). The use of a priori data to resolve non-uniqueness in linear inversion, Geophys. J. Roy. astr. Soc., 57, 137-157.

- Langston, C. A. (1981). Source inversion of seismic waveforms: the Koyna, India, earthquakes of September 13, 1967, Bull. Seismol. Soc. Am., 71, 1-24.
- Mellman, G. R. (1980). A method for waveform inversion of body-wave seismograms, Ph.D. thesis, Caltech.
- Nabelek, J. L. (1984). Determination of earthquake source parameters from inversion of body waves, Ph.D. thesis, MIT.
- Shaw, P. R. (1983). Waveform inversion of explosion seismology data, Ph.D. thesis, UCSD.
- Stump, B. W. and L. R. Johnson (1977). The determination of source properties by the linear inversion of seismograms, Bull. Seismol. Soc. Am., 67, 1489-1502.
- Stump, B. W. and L. R. Johnson (1984). Near-field source characterization of contained nuclear explosions in tuff, Bull. Seismol. Soc. Am., 74, 1-26.
- vonSeggern, D. and R. Blandford (1972). Source time functions and spectra for underground nuclear explosions, Geophys. J. Roy. astr. Soc., 31, 83-97.
- Wallace, T. C. (1983). Long period regional body waves, Ph.D. thesis, Caltech.
- Wiggins, R. A. (1972). The general linear inverse problem: Implications of surface waves and free oscillations for earth structure, Rev. Geophys. Space Phys., 10, 251-285.